DEVELOPMENT AND TESTING OF DEGRADABLE MAGNESIUM ALLOYS FOR BONE FRACTURE HEALING

by

Amy Elizabeth Chaya

BS Bioengineering, University of Pittsburgh, 2009

Submitted to the Graduate Faculty of

The Swanson School of Engineering in partial fulfillment

of the requirements for the degree of

Doctor of Philosophy

University of Pittsburgh

2016

UNIVERSITY OF PITTSBURGH

SWANSON SCHOOL OF ENGINEERING

This dissertation was presented

by

Amy Chaya

It was defended on

December 18, 2015

and approved by

Elia Beniash, PhD, Department of Oral Biology

Aaron Barchowsky, PhD, Department of Environmental and Occupational Health

Bernard J. Costello, MD, DMD, Department of Oral and Maxillofacial Surgery

Yadong Wang, PhD, Department of Bioengineering

Dissertation Director: Charles Sfeir, DDS, PhD, Departments of Oral Biology and Periodontology

DEVELOPMENT AND TESTING OF DEGRADABLE MAGNESIUM ALLOYS FOR BONE FRACTURE HEALING

Amy Chaya, Ph.D.

University of Pittsburgh, 2016

Bone fractures are an extremely common injury, with over six million occurring each year in the U.S. Roughly one third of these fractures require internal fixation devices, such as plates and screws, to facilitate bone healing. Traditionally, internal fixation devices have been made with permanent metals like titanium alloys, which can cause long-term complications and even require surgical removal. To circumvent these problems, resorbable polymeric devices have been developed; however their mechanical limitations render them inadequate for many load bearing applications. Unlike permanent metals and resorbable polymers, degradable magnesium alloys provide a balance of degradation and strength. Recent investigations with magnesium alloys have begun demonstrating their promise as orthopedic biomaterials; however, additional work remains to fully assess their efficacy.

For these reasons, we conducted in vivo studies to better understand the biological effects of magnesium degradation. To begin, two subcutaneous implant models were developed incorporating human stem cells and magnesium implants. Using these models, we measured gradual magnesium degradation, and observed human cells and osteogenic protein expression around the implant-tissue interface. These results supported subsequent assessments of magnesium as fixation plates and screws using an ulna fracture model. With pure magnesium devices, we observed gradual implant degradation and fracture healing similar to that of clinically-used titanium devices. In addition, we observed abundant new bone formation around

the degrading magnesium devices. Interestingly however, when testing faster degrading magnesium alloy devices, we observed localized cortical bone loss. This dichotomy in observations emphasizes the biological sensitivity to magnesium implants based on their degradation rate and composition. Taken together, our results demonstrate preliminary efficacy of pure magnesium fixation devices and support their continued development; however, additional investigations should be conducted to fully understand the mechanisms of magnesium's effect on bone biology and long-term safety.

TABLE OF CONTENTS

LIST OF TABLES

LIST OF FIGURES

PREFACE

This dissertation is dedicated to my amazing family and friends, whose endless love and encouragement has been my constant source of support, happiness, and inspiration. I hope that this dissertation will finally explain what I've been up to for all of these years.

This work would not have been possible without the support of countless individuals. Special thanks to Dr. Elia Beniash, Dr. Aaron Barchowsky, Dr. Bernard J. Costello, Dr. Yadong Wang, and Dr. Prashant N. Kumta for their ongoing guidance throughout my research. Thank you to the entire Center for Craniofacial Regeneration, past and present, who have not only provided research support, but countless laughs and happy memories. Thank you to the Department of Bioengineering, for your support over the many (many, many, many…) years. And finally, merci beaucoup to Dr. Charles Sfeir for being a truly wonderful mentor. Not only have you helped me grow as a scientist, but you have instilled in me la joie de vivre which I shall carry with me forever.

1.0 INTRODUCTION

1.1 BONE

1.1.1 Composition and formation

Bone is a highly dynamic and complex organ, composed of organic (40% by dry weight, 50% by volume) and inorganic (60% by dry weight, 50% by volume) constituents [1-3]. The organic portion of bone predominantly consists of a type I collagen matrix. The fibrils of this matrix are organized as parallel layered sheets, providing tensile strength and a template for mineralization. Also within the matrix are proteoglycans and non-collagenous proteins such as osteocalcin (OC), dentin matrix protein 1 (DMP1), and osteopontin (OPN). These proteins are secreted by bone forming osteoblast cells and regulate mineralization by facilitating collagen alignment, cell adhesion, and hydroxyapatite deposition (data accessible at NCBI GEO database [4, 5].

Hydroxyapatite serves as the inorganic, mineral portion of bone. As it is deposited into the collagen matrix, the tissue hardens and immature bone is formed. Throughout this process, many osteoblasts localize at the leading edge of mineralization known as the osteoid layer. In addition, some osteoblasts remain within the mineralizing matrix, becoming osteocytes. Though these mature bone cells reside in individual lacunae, they are thought to play a role in ongoing bone remodeling by communicating with neighboring cells through canaliculi [1, 3].

This ornate bone formation process occurs endlessly, but is balanced by the work of bone eroding osteoclasts. These cells dissolve adjacent mineral through acidification by hydrogen ion release. In doing so, osteoclasts can tunnel deep into bone, providing an entry way for other cells and blood vessels. This delicate balance of osteoblast and osteoclast activity is necessary to maintain healthy bone turnover, with perturbations potentially leading to bone diseases like osteoporosis and osteopetrosis.

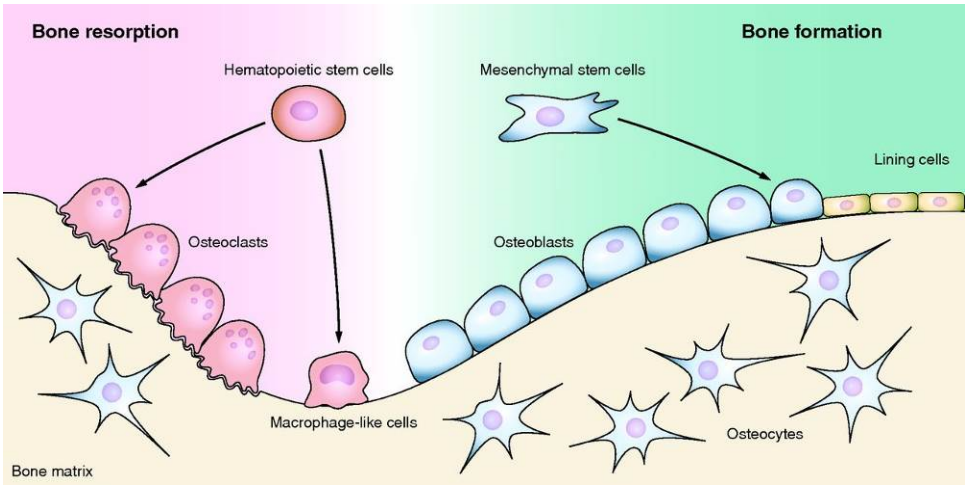

Figure 1. Schematic of bone cells involved in bone formation and resorption [6].

1.1.2 Structure

Macroscopically, two types of bone exist in the adult skeleton: cortical (compact) and trabecular (spongey). Cortical bone is highly dense and forms the strong outer edge of mature long bones, encasing the bone marrow cavity. This compact bone has a high stiffness and compressive strength, facilitating the skeleton's load bearing capabilities. In contrast, trabecular bone is less dense, with a spongey morphology and high surface area to weight ratio. This bone is most commonly found in vertebrae, flat bones, and the center and ends of long bones. Though it has a lower strength than cortical bone, it contributes to the overall stability of long bones and is

thought to remodel in response to mechanical loading. Importantly, trabecular bone serves as a reservoir for blood cell producing red bone marrow, as well as stem and osteogenic cells [7].

The external surfaces of bone are covered in a non-mineralized periosteum. This connective tissue is highly vascularized and contains undifferentiated, pluripotent mesenchymal stem cells (MSCs) which may be recruited upon injury to aid in bone healing and remodeling. For instance, upon bone fracture, MSCs from an uninjured periosteum can be induced to differentiate into chondroblasts, fibroblasts, and osteoblasts to facilitate callus formation and fracture union [8]. Furthermore, stem cells from the periosteum play important roles in bone formation and growth.

1.1.3 Growth

Bone growth can occur through endochondral or intramembranous ossification. Endochondral ossification begins with cartilage which becomes the primary site of ossification. Chondrocytes within this region undergo hypertrophy while an outer periosteal layer is formed. This periosteal layer contains undifferentiated MSCs which later differentiate into osteoblasts and form a boney collar. As bone growth perpetuates, chondrocytes cease secreting collagen and proteoglycans and begin secreting alkaline phosphatase (ALP). This ALP secretion causes additional mineralization of the matrix, which is further remodeled by osteoclasts to form a central medullary cavity for bone marrow. As this process continues, the bone is further elongated through endochondral ossification at secondary sites within the bone's epiphyses [9]. This growth mechanism is common for weight bearing long bones; however, craniofacial bones undergo growth through intramembranous ossification.

Unlike endochondral ossification, intramembranous ossification does not involve cartilage. Instead, intramembranous ossification begins with a cluster of MSCs which differentiate into osteoblasts and secret a matrix of type I collagen. This matrix becomes mineralized as previous described, resulting in newly formed bone [9].

1.1.4 Repair

When a bone is damaged or fractured, it undergoes three main stages of healing: 1) reactive (inflammation), 2) reparative, and 3) remodeling [10].

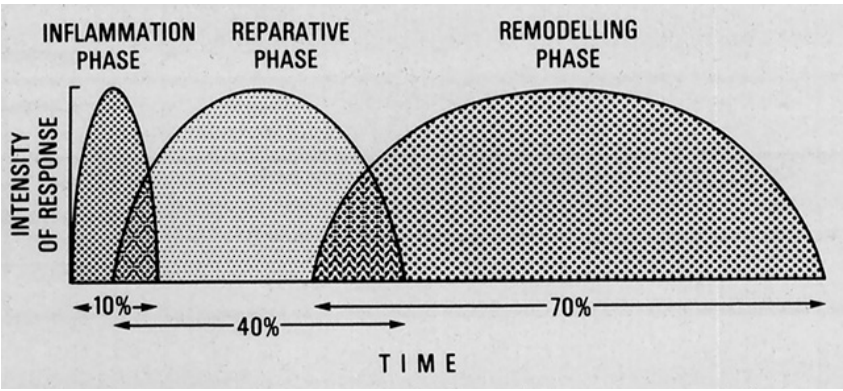

Figure 2. Phases of bone healing and their relative durations [11].

During the reactive phase, the injured site experiences blood clotting, inflammation, and initiation of debriding bone resorption. In addition, granulation tissue forms. Fibroblasts within this tissue, as well as stem cells from the adjacent periosteum and bone marrow, then differentiate into chondroblasts and form hyaline cartilage. This cartilage is later replaced with bone through endochondral ossification as previously described. In addition, some periosteal stem cells differentiate into osteoblasts to form a callus of woven bone over the injured site.

Throughout the remodeling stage, the woven bone is transformed into stronger lamellar bone, re-establishing the bone's mechanical integrity.

In addition to repair through endochondral ossification, intramembranous ossification can occur when the fracture is subject to low strain (< 2%). For instance, if a long bone fracture is stabilized with a rigid internal plating system, the strain on the fractured bone is reduced, promoting healing through intramembranous ossification [12, 13]. Similarly, craniofacial bones which naturally reside in low load bearing and subsequently low strain environments typically repair their fractures via intramembranous ossification.

1.2 BONE FRACTURE MANAGEMENT

Despite bone's sophisticated self-repairing capabilities, nearly one third of all fractures require additional support from internal fixation devices to facilitate healing [14]. These devices include hardware such as pins, nails, plates, and wires, which are implanted to re-align and stabilize bone fragments throughout healing (Figure 3). Traditionally, these devices have been made with permanent metals; however, resorbable polymeric devices have also been developed.

1.2.1 Permanent metal fixation devices

Currently, permanent metals such as titanium (Ti) alloys are the gold standard material for internal fixation devices [15]. These metals were originally selected for their strength and biocompatibility, but have been shown to cause long term complications including interference with pediatric skeletal growth, pain, tissue irritation, metallosis, infection, wear debris

accumulation in the liver and kidney, weakening and necrosis of surrounding bone, and bone re-fracture [15-18]. To avoid these complications, devices may be removed through a second invasive surgery, further increasing patient burden and risk, increasing total procedural costs, and draining valuable hospital resources [15, 19].

Figure 3. Schematic of long bone fracture with fixation plate and screws [20].

1.2.2 Resorbable polymer fixation devices

To circumvent problems associated with permanent implants, resorbable polymers such as poly(lactic-co-glycolic acid) (PLGA) have been utilized [21-23]. Although the resorbable property of these materials conveys a unique advantage over permanent metals, their mechanical limitations render them inadequate for many load bearing applications such as mandibular and long bone fixation [15, 24-26]. Additionally, studies have reported long term foreign body complications associated with these materials, likely a result of their highly acidic degradation products [21-23]. For these reasons, there remains a need to develop novel biomaterials for fracture fixation applications.

1.3 MAGNESIUM ALLOYS

Unlike permanent metals and resorbable polymers, degradable magnesium (Mg) alloys can provide an ideal balance of degradation and strength. In aqueous environments such as the body,

Mg alloys degrade through an electrochemical process in which Mg forms a Mg hydroxide passivation layer on the surface of the implant, and Mg ion and hydrogen gas are released (Figure 4).

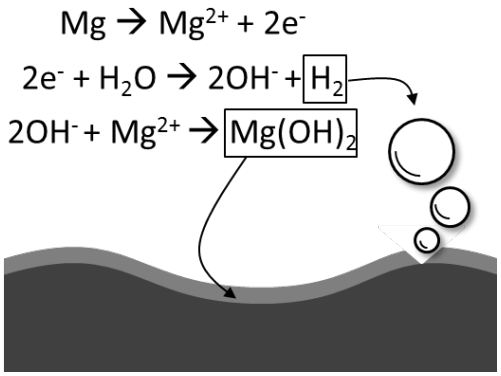

Figure 4. Schematic of Mg degradation process in vivo.

In physiological solutions, this process is accelerated by an abundance of chloride ions which readily react with Mg hydroxide to form highly soluble Mg chloride. This process disrupts the corrosion-protecting oxide layer, enabling pitting corrosion to occur [27].

This degradation process can be exploited to produce degradable metallic fixation devices which reduce the risk of long term complications and eliminate the need for removal surgeries. In addition, device degradation may be advantageous for bone healing. For instance, device corrosion may promote bone remodeling by providing a gradually increasing load to the healing bone [28]. Furthermore, local alkalization caused by Mg degradation elicits calcium and phosphate precipitation which can improve integration with surrounding tissue [26, 28-30]. Unlike permanent metal ion generation which can lead to long term infection, Mg ion is one of the most abundant cations found naturally in the body, half of which is stored in bone [15, 16, 31]. Mg ion is a cofactor for hundreds of enzymatic processes and plays a key role in energy metabolism. Excess Mg that cannot be stored in bone or muscle is routinely excreted by the

kidney, maintaining low levels (1% of total body Mg) of Mg in blood serum and interstitial body fluids [32, 33].

In addition to these biological advantages, Mg alloys can be developed to have optimal mechanical properties for bone fixation. For example, Mg alloys have a low density, high fracture toughness, and compressive strength similar to cortical bone (

Table 1) [16, 26, 34]. These bone-like properties have the potential to reduce adverse stress shielding effects and make Mg alloys suitable for a broad range of clinical applications including load bearing fixation. Furthermore, these alloys can be tailored to match desired mechanical and degradation properties through variations in composition, processing, and post-processing techniques [16, 26, 29]. Taken together, Mg alloys have the potential to not only support, but enhance fracture healing by providing necessary stability while avoiding complications associated with permanent implants.

Table 1. Mechanical properties of craniofacial and orthopedic implant materials and bone [15].

Material	Density (g/cm3)	Elastic Modulus (GPa)	Compressive Yield Strength (MPa)	Fracture Toughness (MPa*m¼)
Bone	1-2	3-20	130-180	3-6
Mg Alloys	1-2	41-45	65-100	15-40
Ti Alloys	4-4.5	110-117	758-1117	55-115
Stainless Steel	7-8	189-205	170-310	50-200

1.3.1 Prior work with Mg alloys

The concept of using Mg for orthopedic applications originated over 100 years ago. These early attempts used Mg implants for joint arthroplasty and inspired subsequent work investigating uses

as orthopedic fixation plates, pins, nails, and wires. Unfortunately however, these early attempts were ultimately unsuccessful clinically due to Mg's rapid degradation [35]. Researchers observed that despite low instances of infection, Mg's uncontrolled corrosion caused rapid gas pocket formation. However, recent advancements have shown that with proper corrosion control, Mg alloys may be suitable for many orthopedic and craniofacial applications [30, 36-39].

To better understand the biological response to these degrading materials, numerous in vitro and in vivo studies have been conducted. Several studies have reported the formation of a calcium and phosphate precipitate on degrading alloys. This layer is thought to provide corrosion protection, promote cell adhesion, and improve osteointegration and osteoconductivity [15, 16, 26, 35]. Furthermore, studies assessing Mg rods in bone have shown high mineral apposition rates, increased bone mass [26], and enhanced neo-formation of bone tissue [28] surrounding the implants. These results suggest that degrading Mg alloys can induce bone cell activation and enhance mineralization in vivo. Furthermore, studies assessing Mg alloys in vivo have shown good biocompatibility and minimal inflammation for slow and fast degrading alloys alike [26, 28, 30, 40]. These results demonstrate that many Mg alloys are biocompatible and capable of promoting localized bone remodeling. Overall, these studies have begun demonstrating the potential for Mg alloys as orthopedic biomaterials.

1.3.2 Challenges studying Mg alloys

Despite the rise in recent interest in Mg alloys for medical applications, numerous challenges remain studying them in vitro and in vivo. One significant challenge lies in that their degradation behavior is highly dependent on their local environment. For example, Witte et al compared the corrosion behavior of Mg alloys AZ91D and LAE442 in vitro and in vivo [29]. They observed

corrosion rates four orders of magnitude higher in vitro than in vivo. These results showed that in vivo corrosion behavior cannot be accurately predicted by traditional indirect in vitro testing, such as those outlined by the American Society for Testing and Materials (ASTM) standards. Furthermore, in a separate study Witte et al observed differences in Mg screw corrosion depending on its local tissue environment in vivo [41]. After implanting Mg alloy AZ31 screws into the hip bone of sheep, they observed accelerated corrosion of screw heads (surrounded by soft tissue) when compared to screw shafts/threads (surrounded by bone). These studies demonstrated the sensitivity of Mg to its immediate local environment and suggested that increased fluid flow and chloride ion concentration accelerates corrosion, while passivation layer protection decelerates corrosion.

Due to these complexities, there remains no consistent correlation between in vitro and in vivo corrosion behavior and subsequent biological response for Mg alloys. For these reasons, in vivo testing is often necessary to provide the most clinically relevant assessments of material behavior and biological effect.

1.4 IN VIVO MODELS FOR MATERIAL AND DEVICE TESTING

Numerous in vivo models exist for studying novel biomaterials such as Mg alloys. For instance, subcutaneous and boney models can provide clinically relevant environments for performing in vivo material verification and device validation testing.

1.4.1 Subcutaneous model

The subcutaneous model is commonly used in rodents such as mice and rats to study material behavior and biological response, including biocompatibility and toxicity. In this model, implants are placed beneath the skin, where they are exposed to a moderate amount of blood flow and biological fluids. Alternatively, intramuscular implantation may be performed when additional exposure to blood flow is desired [42].

Subcutaneous implants often consist of a combination of test materials, scaffolds, cells, and/or growth factors. These implants are often tested as regenerative therapies; however, in the present dissertation, we use subcutaneous implants to study the in vivo behavior various Mg alloys and their effect on an implanted human stem cell population (human bone marrow stromal cells, hBMSCs). To do so, we utilize immunocompromised mice. These mice lack a thymus and cannot produce T-cells, thus unable to fully develop an acquired immune response (Charles River Laboratories, Wilmington, MA). This model, coupled with the naturally immunomodulating behavior of MSCs allows us to study the cells after allogenic transplantation [10, 43].

1.4.1.1 Bone marrow stromal cells

Bone marrow stromal cells (BMSCs) are multipotent stem cells derived from the stroma of bone marrow [44, 45]. In vivo, bone marrow stroma supports local hematopoietic cells by providing signaling factors as well as a mechanical support system. In addition, cells within the stroma serve as a reservoir of osteogenic progenitors to aid in bone growth and repair [44]. When exposed to the appropriate cues, BMSCs can form multiple skeletal tissues including bone, cartilage, and fat. Furthermore, large numbers of BMSCs can be readily obtained from relatively

small amounts of bone marrow with little variation among bone source [44-47]. For these reasons, BMSCs are commonly studied for various hard tissue regeneration applications [48, 49]. For instance, poly(glycerol sebacate) (PGS) scaffolds seeded with BMSCs have been used to regenerate large segmental defects in rabbit ulna [50]. In addition, autologous BMSCs are being tried clinically with scaffolds such as hydroxyapatite, beta-tricalcium phosphate (β-TCP), and fibrin glue to treat various bone defects [48, 49].

In the present dissertation, we utilize hBMSCs as a clinically relevant cell population to study the effects of in vivo Mg degradation. In order to implant the hBMSCs and maintain them around the alloys, we utilize scaffold-based and scaffold-less approaches.

1.4.1.2 Scaffolds

Historically, scaffolds have been considered a critical component of tissue engineering by providing a three dimensional architecture for cell adhesion and growth, as well as mechanical support for load bearing applications. Numerous scaffold materials have been used, each uniquely tailored for their specific tissue engineering application. For instance, within the bone engineering field, an array of metals, polymers, ceramics, hydrogels, and composites have been explored [51]. Typically, these materials are used in concert with cells and growth factors to stimulate and/or support tissue growth and regeneration. However, in the present dissertation, we utilize scaffolds (without the addition of growth factors) to transplant hBMSCs around Mg alloys into subcutaneous pockets in mice. This model allows us to study effects of the degrading alloys on the surrounding hBMSC population within an in vivo environment.

1.4.1.3 Scaffoldless constructs

An alternative approach to using scaffolds is to create scaffoldless constructs. Scaffoldless constructs can be formed from many cell types by allowing them to produce endogenous matrix. The matrix can then be manipulated to form various three dimensional structures such as sheets, rods, and spheres [52-55]. This scaffoldless approach has been adopted for various clinical applications including regeneration of bone, dentin, skin, and cornea, and has been shown to provide several advantages over traditional scaffold-based techniques [55]. For instance, scaffoldless constructs allow cells to create a preferred three dimensional architecture, naturally optimized for their communication, growth, and survival. In addition, scaffoldless constructs eliminate the potential for unwanted scaffold interactions on cell behavior, and can provide an abundant cell population without requiring complex cell seeding methodologies [52, 54, 55].

Similar to scaffolds, scaffoldless constructs have predominantly been explored for tissue regeneration applications. However, in the present dissertation we explore the potential for these constructs to serve as a model for studying the biological response to degrading Mg alloys in vivo. With this model, we are able to study the effects of alloy degradation on hBMSCs in vivo without the use of scaffolds.

1.4.2 Ulna fracture model

The subcutaneous model can provide an adequate environment to study Mg alloys as basic materials; however, it is also necessary to assess these metals as functional devices in their intended biological setting. For these studies, bone defect models are used [56]. In the present dissertation, we utilize rabbit ulna fracture models to assess Mg alloys as fixation plates and

screws. These models allow us to examine fixation devices in a semi-load bearing environment, studying their degradation and effect on bone healing and new bone formation.

In the ulna fracture model, an osteotomy (0.5-1 mm thick) is created through the ulna, while the adjacent radius is left intact. A fixation device is then secured into the ulna to provide fracture alignment and reduction. In this manner, the limb's load bearing is distributed between the uninjured radius and the fractured ulna, providing a semi-load bearing environment for the implanted devices. This model is advantageous for testing novel degradable devices; however, more mechanically rigorous models can also be pursued. For example, a fracture model in which the full thickness of both the radius and ulna are cut would provide a full load bearing environment for implanted devices.

2.0 SPECIFIC AIMS

The overall goal of this dissertation is to assess Mg alloys and their preliminary efficacy as bone fixation devices in vivo. We hypothesize that Mg alloys can serve as ideal bone fixation device materials by providing a unique combination of material degradation and fracture stabilization. To test this hypothesis, we will study Mg alloys in vivo as materials as well as fixation devices through the following specific aims.

2.1. Specific Aim 1: Develop and assess a 3D model to study Mg alloy degradation and effect on human stem cell behavior and differentiation. A 3D model will be developed to study alloy degradation and effect on cells and tissue. The model will consist of a collagen scaffold seeded with hBMSCs containing a central Mg alloy rod. Scaffolds will be implanted in vivo (mouse subcutaneous) and assessed for degradation, mineral formation, and cell localization and differentiation using microCT, histology, and immunohistochemistry. Different alloy compositions will be compared. We hypothesize that hBMSCs seeded in a collagen sponge will provide an efficient system to study Mg alloys in vivo. Furthermore, we hypothesize that Mg alloys will undergo gradual degradation, without inhibiting hBMSC localization or effect on osteogenic differentiation.

2.2. Specific Aim 2: Develop a scaffoldless model from hBMSCs to study Mg alloy degradation and effect on human stem cell behavior and differentiation. Scaffoldless constructs will be created from hBMSCs and formed around Mg alloys. Constructs will be implanted in vivo (mouse subcutaneous) and assessed for degradation, mineralization, and cell localization and differentiation using microCT, histology, and immunohistochemistry. We hypothesize that scaffoldless constructs will provide an efficient model to study Mg alloys while eliminating the potential for scaffold interference.

2.3. Specific Aim 3: Develop and assess novel degradable Mg fixation plates and screws in a semi-load bearing fracture model. Fixation devices will be developed to stabilize ulna fractures in rabbits. Preliminary device efficacy will be assessed by degradation, fracture healing, and new bone formation. Commercially available pure Mg, a novel Mg alloy, and clinically-used Ti devices will be compared. We hypothesize that in the presence of ongoing degradation, Mg fixation devices will provide adequate fracture reduction and facilitate physiological healing.

3.0 AN IN VIVO MODEL TO ASSESS MAGNESIUM ALLOYS AND THEIR BIOLOGICAL EFFECT ON HUMAN BONE MARROW STROMAL CELLS

3.1 ACKNOWLEDGMENTS

The work presented in this chapter was supported by the National Science Foundation's Engineering Research Center for Revolutionizing Metallic Biomaterials (NSF ERC RMB, grant 0812348) and has been published in Acta Biomaterialia [57]. All work was done in collaboration with Dr. Sayuri Yoshizawa, Dr. Kostas Verdelis, Dr. Elizabeth Bilodeau, and Dr. Charles Sfeir. In addition, we thank Andrew Holmes (University of Pittsburgh) for Mg alloy machining, Da-Tren Chou and Dr. Prashant N. Kumta (University of Pittsburgh) for Mg alloy heat treatment, Dr. Frank Witte (Charité Universitätsmedizin, Berlin, Germany) for histological guidance, and Dr. Arnold Donnenberg (University of Pittsburgh) for providing hBMSCs.

3.2 ABSTRACT

Magnesium alloys have many unique qualities which make them ideal candidates for bone fixation devices, including biocompatibility and degradation in vivo. Despite a rise in Mg alloy production and research, there remains no standardized system to assess their degradation or biological effect on human stem cells in vivo. In this study, we developed a novel in vivo model

to assess Mg alloys for craniofacial and orthopedic applications. Our model consists of a collagen sponge seeded with human bone marrow stromal cells (hBMSCs) around a central Mg alloy rod. These scaffolds were implanted subcutaneously in mice and analyzed after 8 weeks. Alloy degradation and biological effect were determined by microcomputed tomography (microCT), histological staining, and immunohistochemistry (IHC). MicroCT showed greater volume loss for pure Mg compared to AZ31 after 8 weeks in vivo. Histological analysis showed that hBMSCs were retained around the Mg implants after 8 weeks. Furthermore, IHC showed the expression of DMP1 and OPN around both pure Mg and AZ31 with implanted hBMSCs. In addition, histological sections showed a thin mineral layer around all degrading alloys at the alloy-tissue interface. In conclusion, our data show that degrading pure Mg and AZ31 implants are cytocompatible and do not inhibit the osteogenic property of hBMSCs in vivo. These results demonstrate that this model can be used to efficiently assess the biological effect of corroding Mg alloys in vivo. Importantly, this model may be modified to accommodate additional cell types and clinical applications.

3.3 INTRODUCTION

Each year, there are approximately six million bone fractures in the United States, often requiring the use of fixation devices to facilitate healing [58]. Traditionally, bone fixation devices have been made with permanent metals such as Ti alloys. Unfortunately, these materials can cause numerous long term complications and may ultimately require removal through a second surgery [15, 17, 59-62]. To circumvent these issues, resorbable polymers have been developed [63]; however, their lack of mechanical stability has rendered them inadequate for

many load bearing applications such as mandibular and long bone fixation [64]. In addition, composite materials such as hydroxyapatite or bioglass contained polyetheretherketone (PEEK) are under development [65]; however, long term foreign body reactions to resorbable polymers have been reported [66-68]. For these reasons, there remains a need to develop novel materials for fracture fixation applications.

Unlike permanent metals and resorbable polymers, degradable Mg alloys can provide an ideal balance of degradation and strength. Mg alloys are biocompatible [26, 40, 69-72], have initial strength and mechanical properties similar to bone [15], and have demonstrated good osteointegration [73, 74]. Furthermore, studies have shown that Mg^{2+} (herein referred to as Mg ion) a product of Mg degradation, may enhance bone formation [15, 26, 75]. For example, a recent study by Yoshizawa et al highlighted the connection between Mg ion and signaling pathways involved in bone formation, emphasizing the potential for these materials in craniofacial and orthopedic applications [76]. For these reasons, numerous Mg alloys are being developed; however, to our knowledge there is no method described in the literature to assess Mg alloy degradation and their cytotoxic or osteogenic behavior on human cells in vivo.

Traditionally, alloy corrosion has been studied with in vitro systems; however, in vitro corrosion is often not indicative of in vivo behavior [77-79]. Similarly, the biological effect of degrading Mg alloys is often tested in vitro through direct or indirect assays. Unfortunately, these systems are usually not suitable for studying long term effects. Furthermore, the observed in vitro cellular response may vary significantly from in vivo tissues [69, 78]. For these reasons, we have established a new system to study Mg alloys and their biological effect in vivo.

Although this work focuses on the effect of Mg alloys on hBMSCs, this model system could be adapted for other cell types and clinical applications. Previous studies have compared

the cellular reaction of cell line (human osteosarcoma cell line MG63) and primary cultured cells (human umbilical cord perivascular cells HUCPV) to Mg alloys. Results showed a significant difference in biological response between these cell types, emphasizing that primary cells should be used for more clinically relevant analyses [80]. Furthermore, hBMSCs have shown to form bone tissue in vivo when transplanted with certain biomaterials, such as hydroxyapatite [81], silk scaffold [82], collagen sponge [83], or even cell sheets without scaffold [54]. For these reasons, we identified hBMSCs as an ideal cell population to study the biological effects of Mg alloys for orthopedic and craniofacial bone regeneration.

To maintain hBMSCs around Mg alloys, a commercially available collagen sponge (Infuse® Bone Graft), without additional growth factors, was used as a scaffold (although other biocompatible scaffold could be used). Cells were pre-seeded in the sponge and transplanted with Mg rods into subcutaneous pockets of immunocompromised mice. We hypothesized that this model would allow us to closely study the effect of alloy degradation on cell behavior and osteogenic differentiation. Importantly, these observations allow us to make informed conclusions regarding alloy potential for craniofacial and orthopedic applications.

3.4 MATERIALS AND METHODS

3.4.1 Cell culture

Human bone marrow cells were provided by Dr. Albert Donnenberg (University of Pittsburgh) as previously described [84]. All procedures were approved by the University of Pittsburgh Committee on Research Involving the Dead. Cells were plated at $4x10^5$ /cm^2 on plastic culture

dishes, and colony forming cells were collected and used as hBMSCs. These cells were characterized for CD105, CD73, CD34, CD90, CD117, CD133, CD45, and CD44 expression by FACS analysis, and cultured in 20% fetal bovine serum (Atlanta Biologicals, Flowery Branch, GA) contained α-minimal essential medium (α-MEM, Life Technologies, Grand Island, NY) with 1% penicillin and streptomycin (Life Technologies, Carlsbad, CA) and 1% L-glutamine (Life Technologies). Cells were subcultured to passage 4, and $6x10^6$ cells per sample were prepared for implantation.

3.4.2 Scaffold and alloy preparation

Collagen sponges (Infuse® Bone Graft, Medtronic, Minneapolis, MN) were cut into 7x7x3 mm cubes, and a central hole for the Mg alloy was punched using a 3 mm diameter Dermapunch™ (Figure 5). The collagen sponges were soaked in culture medium, blotted dry with filter paper, and immediately transferred to cell containing medium at 37ºC for 30 minutes to facilitate cell adhesion. Two types of Mg alloys were assessed in this study, 99.9% pure Mg and AZ31 (3% Al and 1% Zn; Goodfellow, Coraopolis, PA). Alloys were machined as 3x3 mm cylinders, heat treated at 205°C for 1.5 hours, and furnace cooled. Alloys were then washed by sonication in pure acetone and ethanol for 10 minutes each, and sterilized under UV light for 2 hours on all sides. All alloys were kept sterile until implantation. Mg alloys with collagen sponges without hBMSCs were similarly prepared and used as controls.

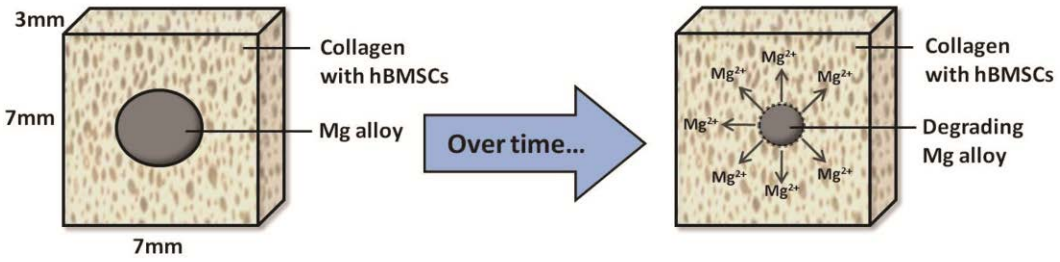

Figure 5. Schematic of scaffold containing collagen sponge with Mg rod and hBMSCs.

Schematic shows degradation of Mg causing Mg ion release into surrounding scaffold and cell population.

3.4.3 Surgical procedure

All protocols for animal experiments were approved by the Institutional Animal Care and Use Committees at the University of Pittsburgh. Eight to ten week old immunocompromised mice (BALB/C nude) were purchased from Charles River Laboratories International (Wilmington, MA). A 2 cm central dorsal incision was made and subcutaneous pockets were created by blunt dissection. Samples were transplanted into individual pockets and incisions were closed with surgical clips. Samples were harvested after 8 weeks, dissected with surrounded tissue, and formalin fixed for subsequent analysis.

3.4.4 MicroCT

Mg alloys were scanned by microCT (VivaCT 40, Scanco Medical AG, Brüttisellen, Switzerland) before implantation and after dissection. Scans were performed at 55 kV, 72 μA, with an integration time of 139 ms (10.5 μm isotropic voxel). After scanning, alloys were segmented from background and soft tissue using adaptive thresholding as previously described

[85, 86]. Thresholds were defined for each sample based on distinct density differences between the Mg alloy and surrounding soft tissue. VivaCT 40 software was then used to analyze alloy morphology and quantify volume.

3.4.5 Histological assessment

Dissected samples were embedded in Technovit 9100 New® (Heraeus Kulzer, Hanau, Germany), allowing sectioning of alloys and mineralized tissue without decalcification. Samples were sectioned at 6-8 μm and stained with Hematoxylin and Eosin, von Kossa, and Alizarin Red. hBMSCs were identified by in situ hybridization using human specific Alu probe with In Situ Hybridization and Detection Kit (Rembrandt, Amsterdam, Netherland) according to manufacturer's instruction. Bone protein expression was analyzed by IHC using primary antibodies against human and mouse DMP1 (SC-6551, Santacruz, Santa Cruz, CA) and human and mouse OPN (SC-10593, Santacruz) with IgG Alexa Fluor® 594 secondary antibody (Life Technologies, Carlsbad, CA). Bright field and fluorescent images were obtained using a Nikon Eclipse TE2000-E microscope (Nikon Instruments, Melville, NY). The inflammation in the surrounding tissue of transplants was analyzed by a pathologist.

3.4.6 Statistical analysis

Statistical analysis was performed using IBM SPSS Statistics 19 (IBM, Armonk, NY). Alloy volume loss was compared between material groups (n=4 per group) using a Student's t-test. Graphical representations reflect mean ± standard deviation.

3.5 RESULTS

3.5.1 Mg degradation behavior

Four samples of each alloy were scanned by microCT before implantation and after 8 weeks to quantify volume changes due to corrosion in vivo. MicroCT 3D reconstructions showed that both pure Mg and AZ31 underwent pitting corrosion; however, pure Mg samples showed larger voids (≤0.2 mm diameter) (Figure 6 A). Alloy volume quantification showed significantly greater volume loss for pure Mg compared to AZ31 after 8 weeks in vivo (Figure 6 B). Pure Mg degradation yielded a net decrease in volume of 1.4 mm^3, while AZ31 yielded a net decrease of 0.5 mm^3.

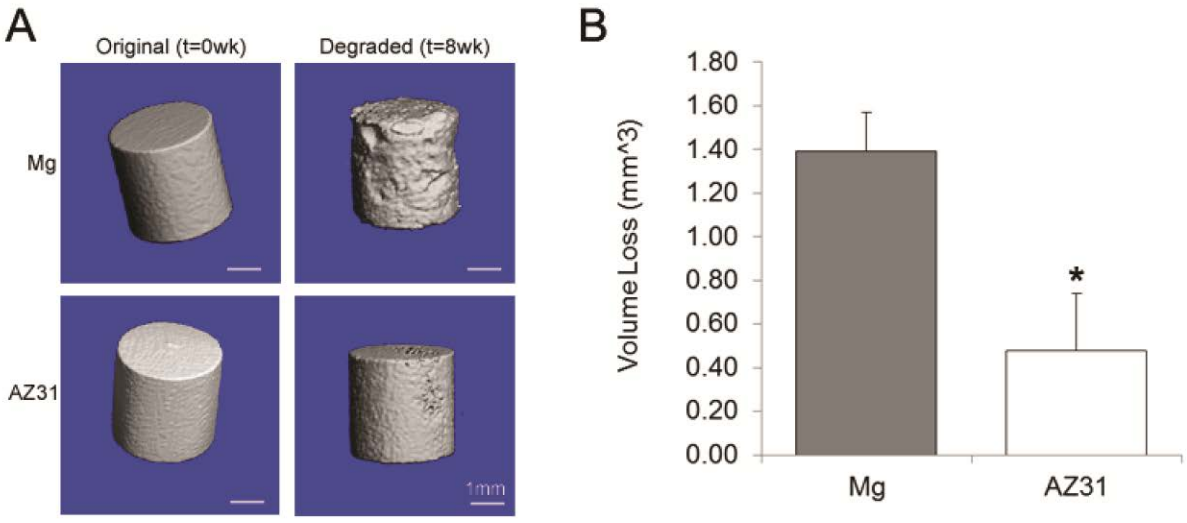

Figure 6. MicroCT showing volume loss of pure Mg and AZ31 after 8 weeks.

MicroCT 3D renderings and volume quantification show significantly greater volume loss for pure Mg compared to AZ31 after 8 weeks in vivo. MicroCT reconstructions show corrosion of pure Mg and AZ31 after 8 weeks (A). Net volume loss was quantified from reconstructed volumes before implantation and after 8 weeks in vivo (B). Averages presented as mean values ± standard deviations (* $p < 0.05$). Scale bars are 1 mm.

3.5.2 Biological response to implant degradation

Mg alloys and surrounding tissue were embedded in Technovit 9100 New®. Blocks were sectioned perpendicular to the long axis of the Mg rod for visualization of the alloy-tissue interface. Most Mg alloy sections were not retained during the sectioning or staining processes; however, their original location remained clearly visible and has been indicated with asterisks throughout. Hematoxylin and Eosin (H&E) staining showed normal tissue morphology and cellularity around all Mg alloys (Figure 7 A-D).

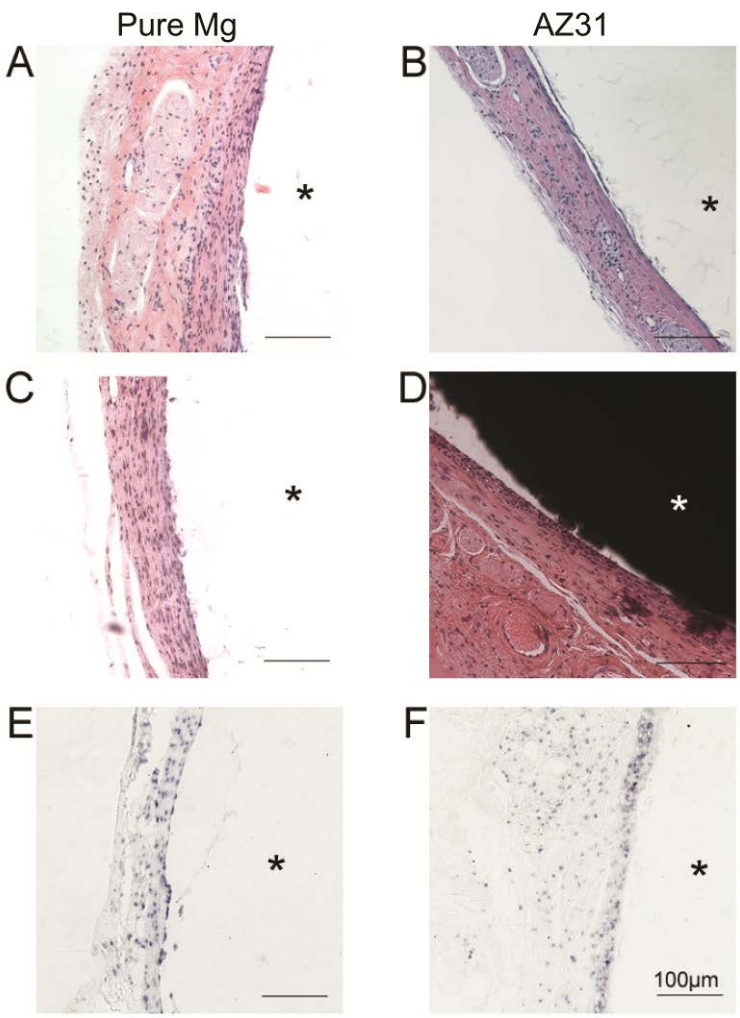

Figure 7. H&E and in situ hybridization showing cellularity around Mg alloys.

H&E stained sections of pure Mg and AZ31 with hBMSCs (A & B) and without hBMSCs (C & D) show cell localization around implants. In situ hybridization with human specific Alu probe on pure Mg (E) and AZ31 (F) identifies human cells within the surrounding cell population. hBMSCs were observed directly surrounding Mg alloys, within fibrous tissue. * indicates implant location. Scale bars are 100 µm.

An appropriate inflammatory response was observed for all samples, including fibrous capsule formation (Supplemental Figure 1). For pure Mg, a mixture, but predominately low intensity

inflammatory infiltrate comprised of predominately lymphocytes, plasma cells, and macrophages was seen. For AZ31, a low to moderate intensity inflammatory infiltrate comprised of a mixture of predominately lymphocytes, plasma cells, and macrophages was seen. No multinucleated giant cells were seen in sections analyzed. hBMSCs were identified by in situ hybridization using human specific Alu probe, and were observed surrounding and often directly in contact with the Mg alloys (Figure 7 E-F). hBMSCs appeared flat and formed multiple layers around the alloys.

Mineral formation was analyzed by von Kossa and Alizarin Red. In all samples, a thin (5-20 μm) layer containing calcium and phosphate was present at the alloy-tissue interface (Figure 8). In some samples, this mineral layer appears separated from surrounding tissue due to sectioning artifact caused by the separation of the Mg alloy during sectioning.

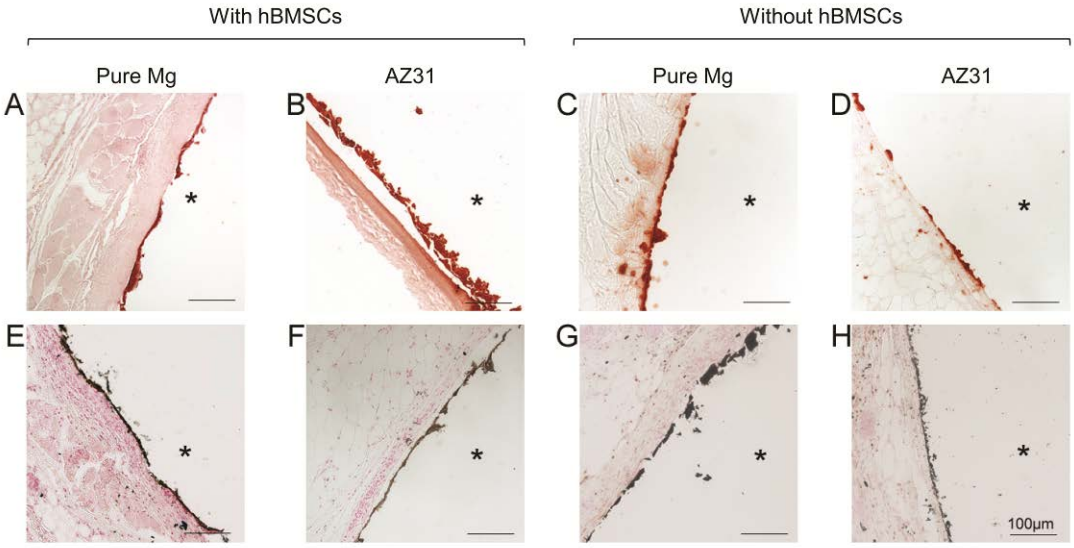

Figure 8. Alizarin Red and von Kossa staining showing mineral around Mg alloys.

Alizarin Red staining of pure Mg and AZ31 with hBMSCs (A & B) and without hBMSCs (C & D), and von Kossa staining of pure Mg and AZ31 with hBMSCs (E & F) and without hBMSCs (G & H) reveal a calcium and phosphate rich layer at the alloy-tissue interface. * indicates implant location. Scale bars are 100 μm.

3.5.3 Osteogenic protein expression around Mg

Osteogenic protein expression was analyzed by IHC. For alloys implanted with hBMSCs, DMP1 (Figure 9) and OPN (Figure 10) expression was observed a short distance (~100 μm) from the alloy-tissue interface. In contrast, for alloys implanted without hBMSCs, no bone marker protein expression was observed. Although no quantitative analysis was performed, the AZ31 group appeared to have slightly higher expression of DMP1 and OPN.

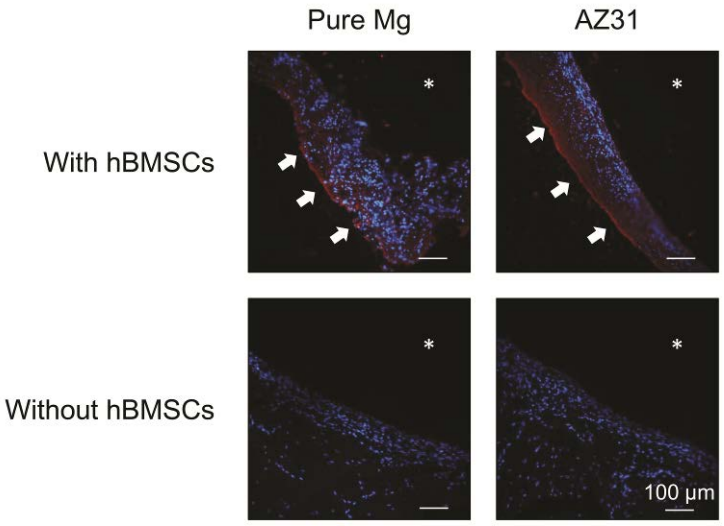

Figure 9. Immunofluorescent staining showing DMP1 expression around Mg alloys. DMP1 expression was observed a short distance from the alloy-tissue interface for pure Mg and AZ31 samples with hBMSCs. DMP1 expression was not observed around alloys implanted without hBMSCs. * indicates implant location. Scale bars are 100 μm.

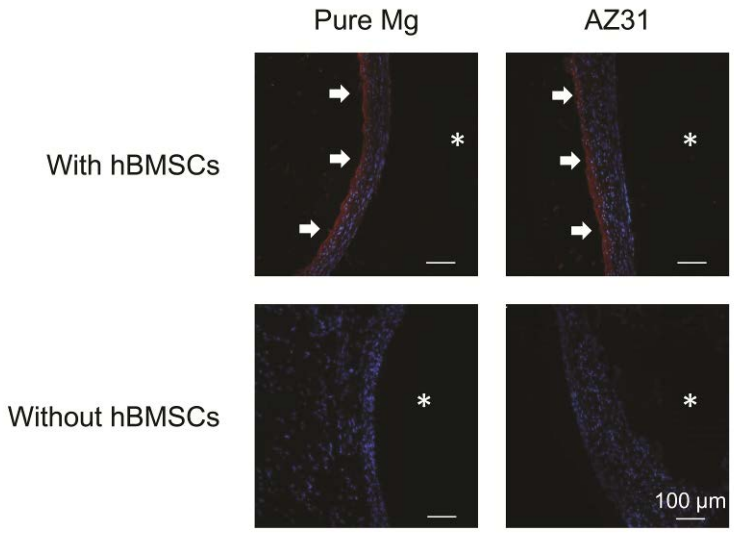

Figure 10. Immunofluorescent staining showing OPN expression around Mg alloys.

OPN expression was observed a short distance from the alloy-tissue interface for pure Mg and AZ31 samples with hBMSCs. OPN expression was not observed around alloys implanted without hBMSCs. * indicates implant location. Scale bars are 100 µm.

3.6 DISCUSSION

Due to their unique combination of biocompatibility, degradation, and mechanical strength, Mg alloys are being studied for numerous craniofacial and orthopedic applications. As an increasing number of alloys are created, there is a growing need to develop a model to assess the biological effect of alloy degradation on human cells in a cost efficient rodent model. Importantly, studies have shown that many traditional in vitro assays cannot accurately predict in vivo behavior [77-79], suggesting that an in vivo assessment model is necessary.

In the current study, we used commercially available 99.9% pure Mg and AZ31 to elucidate appropriate analysis methods for Mg alloys. AZ31 contains 3% Al and 1% Zn, and was

originally produced to improve corrosion resistance for industrial applications. However, its corrosion resistance and biocompatibility suggests its promise as a candidate biomaterial for bone fixation [70]. Although, excess amounts of Al have shown to be toxic and associated with neurological disorders [87], recent in vivo studies using sheep suggest that the amount of Al released by degrading AZ31 bone fixation screws is within the safe range [88]. For this reason, we identified AZ31 as an appropriate slow degrading alloy to compare with faster degrading pure Mg.

To begin assessing the implanted alloys, we evaluated in vivo corrosion behavior. Currently, several methods are used to study alloy corrosion in vitro and in vivo, including weight measurements [78, 89]. This method is largely destructive, requiring surrounding tissue and corrosion products to be chemically removed, therefore inhibiting the ability to study corrosion product production or the alloy-tissue interface. For these reasons, we chose to use high resolution microCT to study changes in alloy volume [78, 85]. To do so, net alloy volume change was observed visually and quantified. Our data show that pure Mg rods underwent significantly greater volume loss than AZ31 after 8 weeks in vivo. Interestingly, it was previously reported that the corrosion rate of 99.99% pure Mg and AZ31 are similar in a rat subcutaneous implant model (99.99% pure Mg: 0.221 mm/year, and AZ31: 0.223 mm/year after 21 days) [90]. This suggests a significant difference in the degradation behavior of 99.9% and 99.99% pure Mg; with 99.9% Mg degrading faster than highly pure 99.99% Mg in vivo. This difference in corrosion rate is likely attributed to microgalvanic corrosion acceleration caused by impurities in the 99.9% pure material [91].

Both pure Mg and Mg alloys are prone to localized pitting corrosion [78, 91]. During degradation, a thin corrosion resistant layer forms on the alloy surface; however this layer is

easily disrupted due to Mg's reactivity with chloride in the body. Disruption of this layer allows corrosion to perpetuate, causing surface particles to break off. This localized corrosion spreads across the alloy surface and may eventually cover the entire alloy [91]. This type of corrosion changes the shape of alloys in vivo, and subsequently affects their mechanical properties. This corrosion behavior, along with hydrogen-assisted cracking and transgranular cracking could ultimately cause Mg alloy fracture [92]. For these reasons, understanding alloy corrosion behavior is crucial while studying Mg alloys for load-bearing devices. Preference should be given to alloys which display corrosion behavior most similar to surface corrosion, thereby avoiding premature catastrophic device failure.

Another key characteristic of degrading alloys is their biological effect. Traditionally, the biological effect of Mg alloys has been studied in vitro by seeding cells directly on Mg alloys [69-71]. However, cells often behave differently in vivo due to protein deposition, long term material exposure, and changes in extracellular matrix [77]. In addition, the degradation rates of Mg alloys vary in vitro and in vivo. For these reasons, in vivo models are often preferred, such as calvarial or femoral defects [93, 94]. These functional models allow assessments of biological responses such as bone regeneration and osseointegration; however, they are typically limited to accommodating a small number of implants per animal, and do not allow us to analyze effects on clinically relevant human cells.

In contrast, our subcutaneous model described herein utilizes a commercially available collagen sponge seeded with hBMSCs and a central Mg rod. Collagen sponges have been used for bone regeneration for decades due to their excellent biocompatibility, cell infiltration capacity, and degradation property [95-97]. In this study, the collagen sponge served as an ideal carrier to maintain cells around degrading alloys. We recognize that this model cannot fully

replicate a functional model (such as those previously described) due to variations in local tissue environment and subsequent Mg alloy corrosion rate; however, it provides many advantages to traditional tissue culture methods. In addition, it utilizes a relatively inexpensive lower rodent model while facilitating clinically relevant assessments of the effect on human cells.

Since Mg alloys exhibit potential as bone fixation devices, we have chosen to study the effect of their degradation on hBMSCs. Specifically, we have focused on assessing mineralization and osteogenic differentiation of cells surrounding the alloys. In situ hybridization and histological sections showed that hBMSCs and host cells remained around the degrading implants, demonstrating the efficacy of this model as a relatively low cost approach to assessing hBMSCs in vivo.

Around the alloys, detailed histologic analysis revealed a low to moderate local inflammatory response, as has been similarly shown with other degradable Mg alloys [40], including fibrous capsule formation. In addition, von Kossa and Alizarin Red staining identified a calcium and phosphate rich layer surrounding all samples. This observation is consistent with several other reports of mineral formation around degrading Mg alloys [26, 70-72, 98]. In the present study, this mineral layer was observed around all alloys, suggesting there was no effect of the implanted hBMSCs on this mineral layer formation. Interestingly however, we did observe differences in bone marker protein expression based on the presence of hBMSCs. IHC of established bone marker proteins DMP1 and OPN showed expression surrounding degrading alloys implanted with hBMSCs. Since no bone protein expression was observed in samples without hBMSCs, we speculate that these proteins are either secreted from hBMSCs or hBMSCs influenced secretion of these proteins from host mouse cells. Interestingly, protein expression was observed approximately 100 μm away from the Mg implants. This expression pattern could

suggest that as the Mg alloys degraded, a gradient of Mg ion was diffused into surrounding tissue. Based on our previous in vitro study, we hypothesize that this gradient stimulated the cells' osteogenic activity when it reached a certain, optimal concentration [76]. These findings might also explain the higher expression of proteins around AZ31 (slower corroding) compared to pure Mg (faster corroding).

3.7 CONCLUSION

In this study, we have developed and tested a novel model to study the biological effect Mg alloys on human cells in a mouse model. We have demonstrated the effectiveness of our model in assessing Mg alloys based on their degradation behavior and subsequent biological effect on both host tissue and implanted hBMSCs in vivo. These data will allow us to more accurately identify Mg alloys which are well suited for bone fixation devices. Uniquely, this model may also be tailored to analyze the biological effect of Mg release from alloys on various cell types.

4.0 A SCAFFOLDLESS MODEL TO ASSESS DEGRADABLE MAGNESIUM ALLOYS IN VIVO

4.1 ACKNOWLEDGEMENTS

The work presented in this chapter was supported by the NSF ERC RMB (grant 0812348) and the Center for Craniofacial Regeneration, and is being prepared for publication. All work was done in collaboration with Dr. Sayuri Yoshizawa, Dr. Kostas Verdelis, Dandan Hong, and Dr. Charles Sfeir. We would also like to acknowledge Dr. Prashant N. Kumta (University of Pittsburgh) for material preparation.

4.2 ABSTRACT

Recent investigations have revealed promise for Mg alloys as orthopedic biomaterials. As new alloys are developed, a model is needed to assess their degradation behavior and effect on cells and tissue in vivo. Previously, we have developed and tested a scaffold-based model for assessing Mg alloys in rodents subcutaneously ("An in vivo model to assess magnesium alloys and their biological effect on human bone marrow stromal cells"). This model utilized a collagen sponge to maintain human stem cells around central Mg implants. As such, we were able to assess Mg degradation and effect on the implanted human cells. However, this model required a

collagen scaffold which has the potential to influence cell behavior. For this reason, we have refined our scaffold-based model to incorporate scaffoldless constructs.

Scaffoldless constructs were formed from hBMSCs and wrapped around Mg rods. These constructs were then implanted into mice subcutaneously and assessed after 4 and 8 weeks. MicroCT analysis showed gradual Mg volume loss overtime with surface corrosion product formation. The rate of Mg corrosion was shown to decrease in rate overtime, likely a result of surface passivation. Histological staining as well as SEM and EDX identified Mg, Ca, and P within the corrosion layer. Adjacent to this layer, both mouse and human cells were identified after 4 and 8 weeks. Interestingly, immunohistochemistry revealed OC and OPN expression around the degrading Mg implants in all groups. These results suggest that the Mg degradation and/or corrosion product formation affected cell behavior and triggered osteogenic protein secretion. Additional work is needed to fully understand the mechanism of this effect; however, this study shed important light on the potential role of the corrosion layer in the biological effect of Mg implants in vivo.

4.3 INTRODUCTION

Due to their desirable combination of mechanical strength, in vivo degradation, and biocompatibility, Mg alloys are being extensively studied for various clinical applications including bone fixation. In turn, numerous alloys are being developed to meet application-specific mechanical and degradation behavior needs. Traditionally, in vitro tests have been used to evaluate novel materials; however, studies have demonstrated a mismatch between in vitro and in vivo behavior for Mg alloys [29, 77, 99]. For these reasons, in vivo testing is often desired

to provide a more clinically accurate representation of Mg alloy behavior and associated host response.

Previously, we established a model for assessing Mg alloys which consisted of Mg rods within a collagen sponge seeded with hBMSCs [57]. Using this model, we studied the effects of Mg degradation on the surrounding human cell population through microCT and histology. This model served as an effective method of studying Mg alloys for bone fixation and could be adapted to accommodate other materials and clinical applications. However, one drawback of this approach is that it requires the use of a scaffold to maintain human cells around the Mg implants. Though scaffolds are commonly used in regenerative medicine, they may not be ideal for studies assessing the cellular response to a test material since the introduction of a scaffold can cause unwanted complications. For instance, scaffolds have the potential to influence cell behaviors such as survival, migration, and differentiation [100-103]. In addition, scaffolds can pose further complications due to difficulty achieving efficient cell seeding [104-108]. Since our focus is to assess the response of the surrounding cell population, it is critical that ample cell seeding is achieved.

To circumvent these potential complications, a scaffoldless approach can be used. This method eliminates the use of a scaffold by allowing cells to form their own 3D structures and maintain a more biomimetic environment with enhanced cell-cell communication and extracellular matrix production. In addition, scaffoldless constructs can remodel freely without inhibition by a scaffold material. Furthermore, scaffoldless constructs eliminate the risk of carrier interaction on cell behavior or potential toxicity from scaffold degradation products [55]. For these reasons, scaffoldless constructs are being used for numerous research applications, including bone tissue engineering [52].

In the present study, we have refined our previously described model to eliminate the use of a cell carrier and alternatively allow hBMSCs to form scaffoldless constructs. We have engineered these constructs to be wrapped around Mg alloys, enabling contact between the cells and degrading Mg. We hypothesize that this method will allow us to study Mg alloys for bone fixation, including their in vivo degradation behavior and effect on a clinically relevant human stem cell population. Furthermore, we view this scaffoldless approach as a platform model which can be tailored to accommodate alternative test materials and cell types.

4.4 MATERIALS AND METHODS

4.4.1 Magnesium implants

Commercially available 99.9% Mg (Goodfellow, Coraopolis PA) was used for this study. Mg implants were machined as 3 x 3 mm rods and subsequently cleaned by sonicated washes in acetone and ethanol, followed by gamma sterilization (2 x 10^6 cGy, 23.5 Gy/min, cesium 137 source, Mark I 68, JL Shepherd and Associates, San Fernando, CA).

4.4.2 Scaffoldless construct formation

Human bone marrow stromal cells were obtained from the Tulane Center for Gene Therapy / Institute for Regenerative Medicine at Scott & White. Cells were expanded according to the provider's recommendations and used to form scaffoldless constructs as previously described [52, 54]. Cells were cultured in 10 cm dishes with αMEM (Life Technologies, Grand Island, NY)

with 10% fetal bovine serum (Atlanta Biologicals, Flowery Branch, GA), 1% penicillin and streptomycin (Life Technologies, Carlsbad, CA), and 1% L-glutamine (Life Technologies) until confluent sheets were formed. Cell sheets were then carefully detached from the dishes using a cell scrapper and gentle agitation. Cell sheets were wrapped around sterile Mg rods (Figure 11) and kept in cell culture medium until implantation. Mg rods without scaffoldless wrappings were also prepared and used as controls.

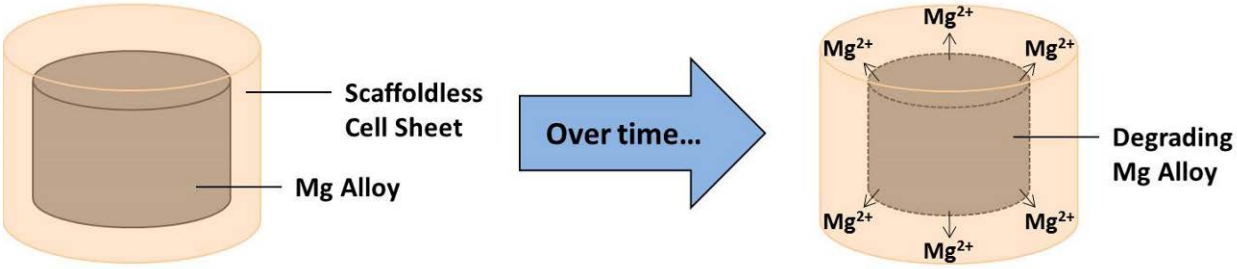

Figure 11. Schematic of scaffoldless constructs with Mg rod.

As the central Mg alloy degrades, the surrounding cell population (within the scaffoldless sheets as well as surrounding host tissue) is exposed to Mg degradation products such as Mg ion.

4.4.3 Surgical procedure

All protocols for animal experiments were approved by the University of Pittsburgh's Institutional Animal Care and Use Committees. Eight to ten week old immunocompromised mice (BALB/C nude) were used for this study (Charles River Laboratories International, Wilmington MA). A 2 cm central dorsal incision was made and subcutaneous pockets were created by blunt dissection. Constructs were transplanted into individual pockets and the incision was closed with sutures. Animals were euthanized 4 and 8 weeks post-operative for further analysis.

4.4.4 MicroCT

MicroCT was used to study Mg degradation. Rods were scanned prior to implantation and after 4 and 8 weeks post-operative with a VivaCT 40 (Scanco Medical AG, Brüttisellen, Switzerland, 10.5 μm voxel, 55 kVp, 72 μA). In addition, live animal scanning was performed every 2 weeks (30 μm voxel, 70 kVp, 114 μA). Using Scanco software, Mg alloys were segmented from surrounding soft tissue based on distinct density differences, and 3D renderings were created showing alloy morphology. Some samples (n=4 per group) were also scanned with a SkyScan 1172 (Bruker-MicroCT, Kontich, Belgium, 6.9 μm voxel, 59 kVp, 167 μA) after 4 and 8 weeks to quantify degradation as previously described [109, 110]. High resolution and contrast allowed underlying Mg and surface corrosion product volumes and surface areas to be quantified separately using Skyscan CTAn software. These volume and surface area values were then used to calculate the corrosion rates of both materials from 0 to 4 weeks, and 4 to 8 weeks.

4.4.5 Histological assessment

Dissected samples were formalin fixed and embedded in Technovit 9100 new® (Heraeus Kulzer, Hanau, Germany). Samples were sectioned at 7-10 μm and stained with Hematoxylin and Eosin, von Kossa, and Alizarin Red. Human cells were identified by in situ hybridization using human specific Alu probe with In Situ Hybridization and Detection Kit (Rembrandt, Amsterdam, Netherland). Furthermore, bone protein expression was analyzed by IHC with primary antibodies against OC (sc-30044, Santacruz, Santa Cruz, CA) and OPN (sc-10593, Santacruz, Santa Cruz, CA), with Alexa Fluor® 488 and 594 secondary antibodies (Life Technologies, Carlsbad, CA).

Bright field and fluorescent images were obtained for analysis (Nikon Eclipse TE2000-, Nikon Instruments, Melville, NY).

4.4.6 Scanning electron microscopy and energy dispersive x-ray spectroscopy

One sample per group underwent scanning electron microscopy (SEM, JEOL JSM-6610, JEOL Ltd., Tokyo, Japan) and energy dispersive x-ray spectroscopy (EDX, EDAX Genesis, Mahwah, NJ) to further assess the formation and elemental composition of the corrosion layer. For each sample, three separate areas containing corrosion layer around the alloy-tissue interface were studied on three separate histological sections.

4.4.7 Statistical analysis

Statistical analysis was performed using IBM SPSS Statistics 19 (IBM, Armonk NY). For degradation assessments, Mg volumes were compared across time points (0, 4, and 8 weeks) using ANOVA and Students t-tests (n=4 per time point). For corrosion rate assessments, samples were compared between two time frames (0 to 4 weeks and 4 to 8 weeks) using Student's t-test. All graphical representations reflect mean ± standard deviation.

4.5 RESULTS

4.5.1 Mg degradation behavior

The in vivo degradation of 99.9% Mg was evaluated with microCT. In general, remaining Mg volume was reduced over time while corrosion product was formed at the surface (Figure 12). Based on Mg volume loss, corrosion rates were calculated to be 0.63 ± 0.21 and 0.60 ± 0.02 mm/yr for 0 to 4 weeks and 4 to 8 weeks, respectively. A Student's t-test revealed a significant decrease in corrosion rate over time (Figure 13).

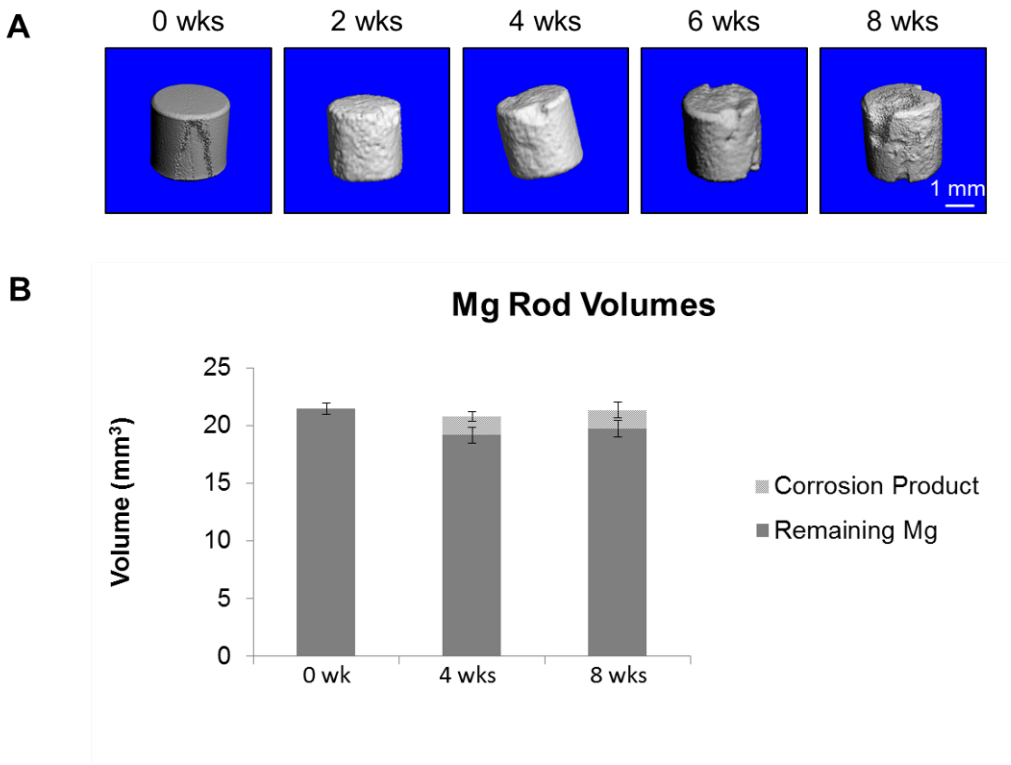

Figure 12. MicroCT showing Mg degradation overtime.

Medium resolution scans (30 µm voxel) were performed and 3D volumes were generated to visualize corrosion (A). High resolution scans (10.5 µm voxel) were performed before implantation and after explantation. Areas of Mg and corrosion product were quantified separately.

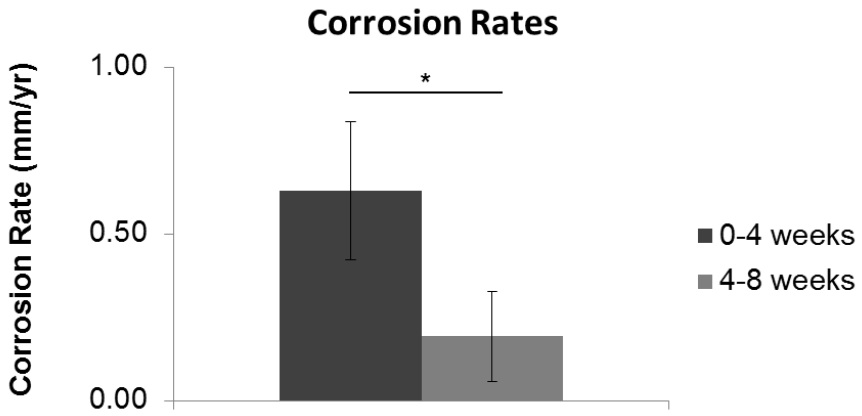

Figure 13. Corrosion rates of Mg overtime.

Corrosion rates were determined from microCT volume loss quantifications from 0 to 4 weeks and 4 to 8 weeks (* p=0.016).

4.5.2 Corrosion layer formation

Corrosion layer formation surrounding the alloys was first evaluated with Alizarin Red (Figure 14) and von Kossa (Figure 15) stainings. These stainings revealed a Ca and P rich layer surrounding all degrading materials. This layer was also observed by microCT as a lower density ring at the periphery of the Mg alloys. In addition, SEM and EDX revealed the presence of Ca, P, and Mg within the corrosion layer of all degrading alloys (Figure 16).

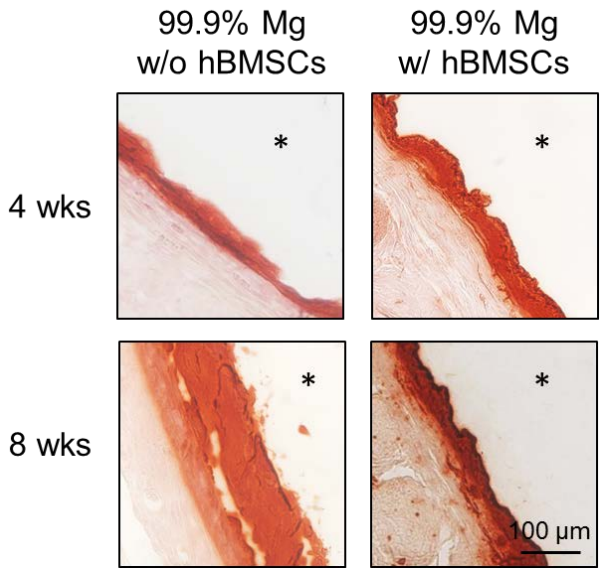

Figure 14. Alizarin Red staining showing Ca around Mg.

Alizarin Red (dark orange/red) shows calcium-rich layer surrounding Mg implants after 4 and 8 weeks post-op. * indicates original location of Mg implant.

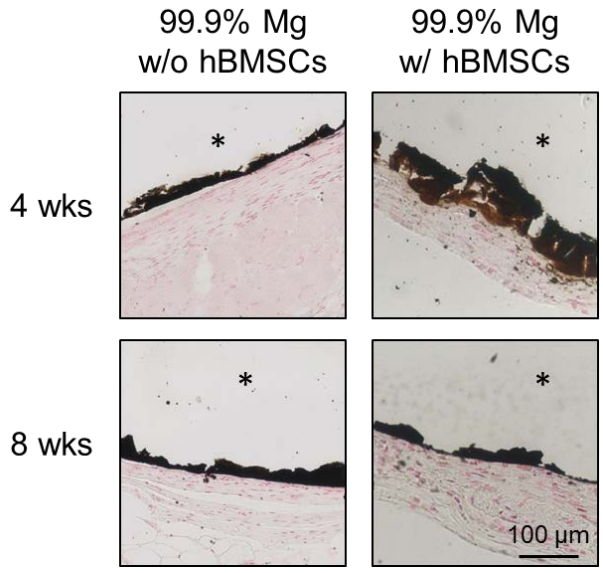

Figure 15. Von Kossa staining showing P around Mg.

Von Kossa (dark brown/black) shows phosphate-rich layer surrounding Mg implants after 4 and 8 weeks post-op. Discontinuity of the stained layer reflects sectioning artifact only. * indicates original location of Mg implant.

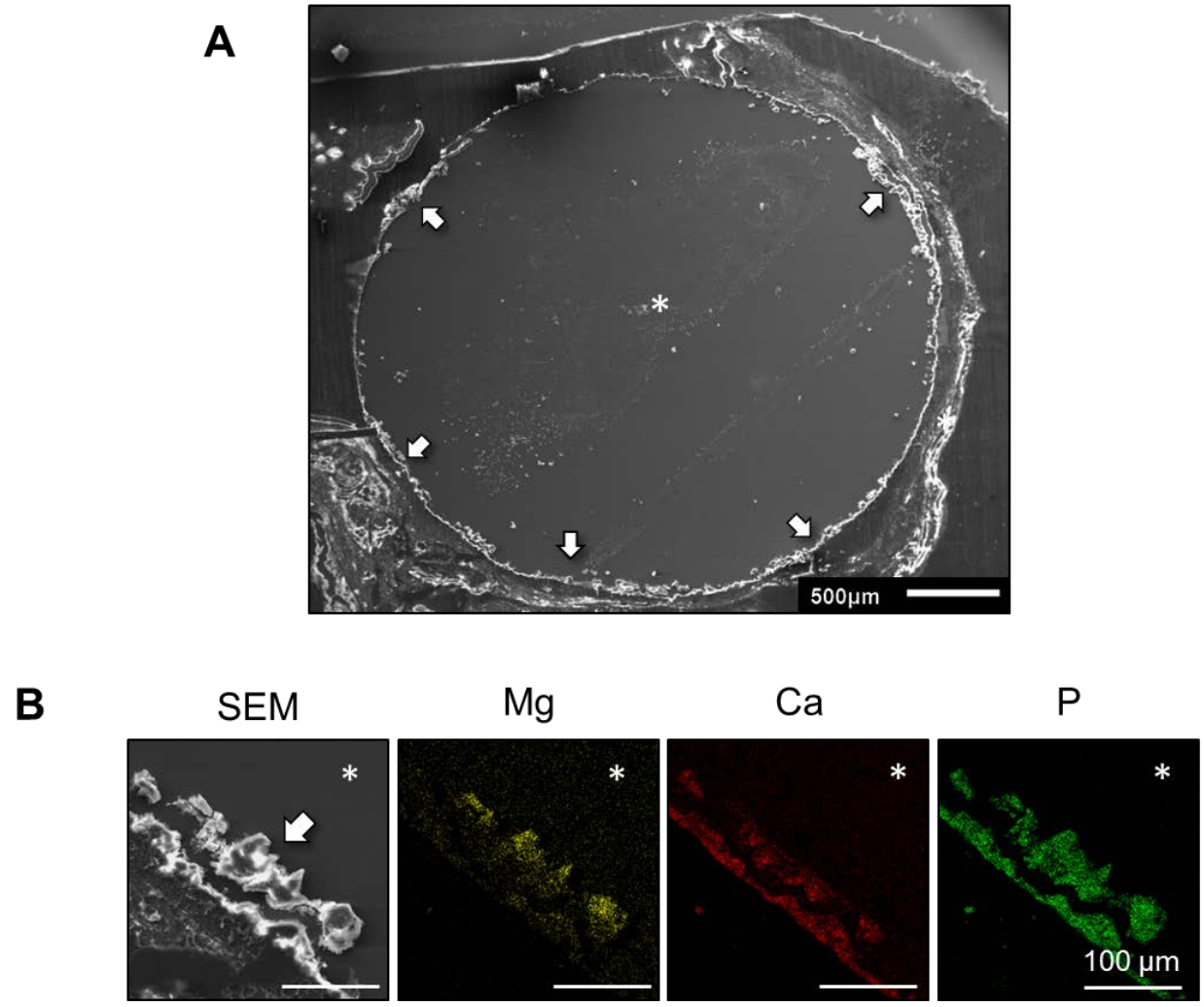

Figure 16. SEM and EDX showing corrosion layer around Mg.

SEM and EDX were used to study the corrosion product formed around degrading alloys. SEM shows a dense mineral deposition at the alloy-tissue interface (A, white arrows). EDX elemental mapping reveals Mg, Ca, and P within the layer of corrosion product. * indicates original location of Mg implant.

4.5.3 Cellularity surrounding Mg implants

Hematoxylin and Eosin staining showed normal tissue morphology and cellularity surrounding the implants (Figure 17 A). Human cells were identified using in situ hybridization targeting the

human specific Alu sequence. hBMScs were identified around implants, near the alloy-tissue interface, after 4 and 8 weeks (Figure 17 B).

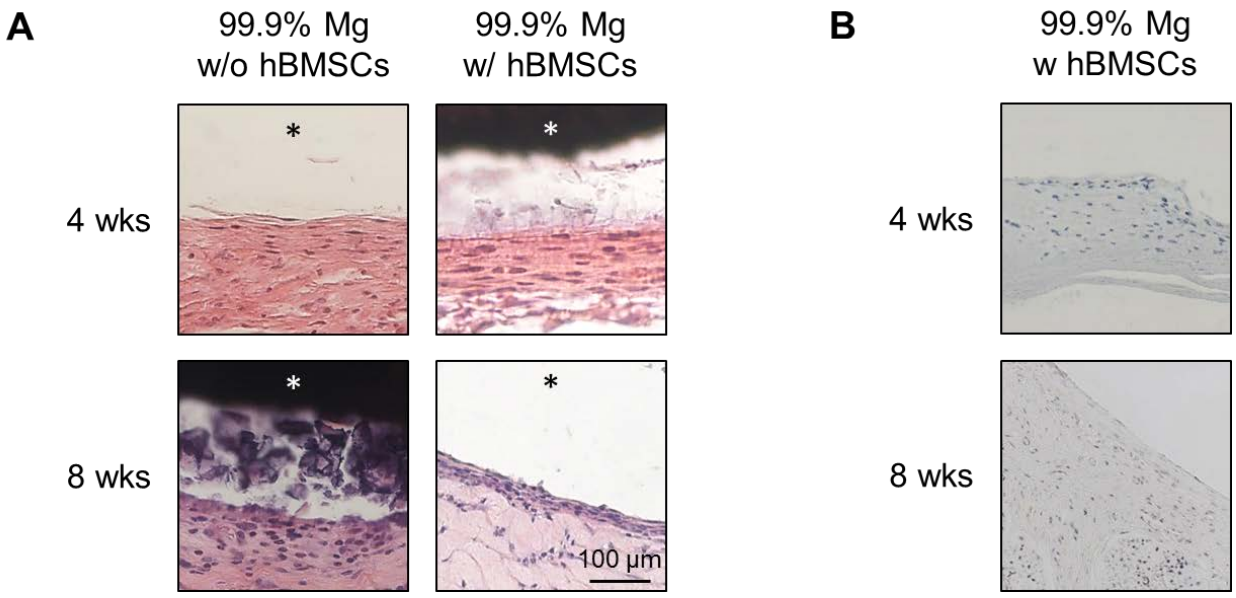

Figure 17. Cellularity around Mg.

Tissue morphology and cellularity were assessed with H&E staining (A). In situ hybridization with human Alu probe was used to identify hBMSCs within adjacent tissue (B, blue/black). * indicates original location of Mg implant.

4.5.4 Osteogenic protein expression around Mg

OC and OPN expression was assessed by immunofluorescence staining. OC (Figure 18) and OPN (Figure 19) were observed at the interface of the degrading Mg rod and surrounding tissue for all samples. No qualitative differences were observed in the expression of these proteins in constructs with or without hBMSCs.

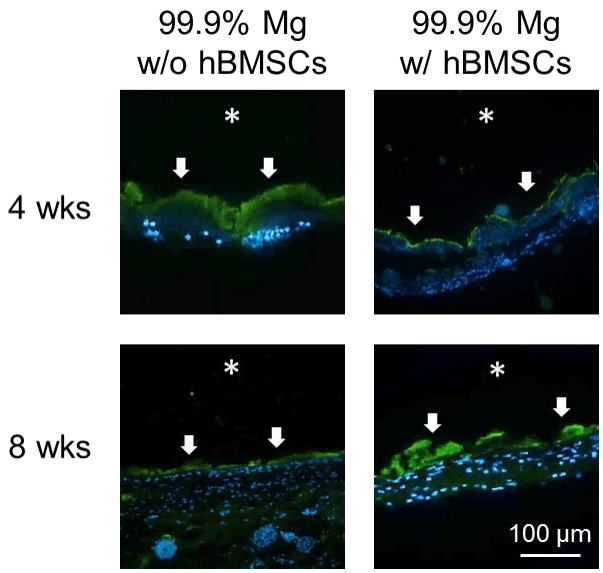

Figure 18. Immunofluorescent staining showing OC expression around Mg.

OC expression was observed at the Mg alloy-tissue interface for all samples (green, white arrows). * indicates original location of Mg implant.

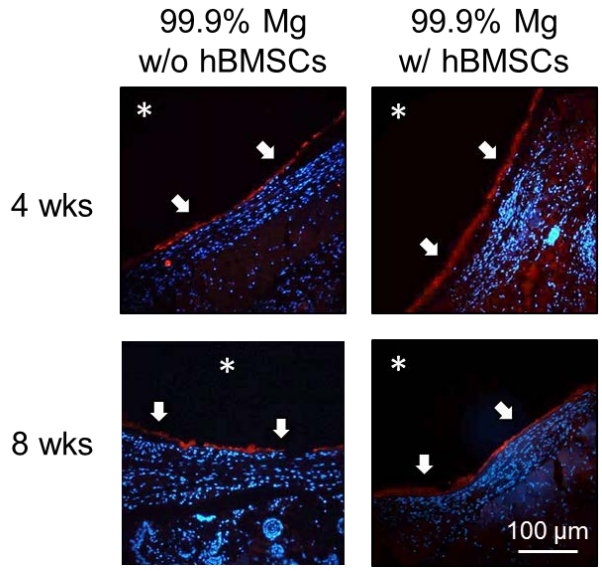

Figure 19. Immunofluorescent staining showing OPN around Mg.

OPN expression was observed at the Mg alloy-tissue interface for all samples (red, white arrows). * indicates original location of Mg implant.

4.6 DISCUSSION

Previously, we presented a model to study Mg alloys in vivo that utilized a scaffold seeded with human stem cells [57]. This model allowed us to study alloy degradation and subsequent effect on human cell behavior in vivo. However, one drawback of this system is that it required the use of a collagen sponge as a cell scaffold. In the present study, we have refined our original model to utilize scaffoldless constructs in the place of collagen scaffolds. This model allowed us to assess clinically relevant human stem cells in contact with degrading Mg implants. We hypothesized that this model would allow us to study alloy degradation and stem cell behavior, while providing a clinically relevant cellular environment and eliminating risk of unwanted scaffold influence on cell behavior.

Scaffoldless constructs are being studied for a wide range of clinical applications, including hard tissue regeneration [53-55, 111-113]. For instance, Akahane et al formed scaffoldless constructs from MSCs and studied their osteogenic potential subcutaneously in rats [54]. This work demonstrated the ability to form scaffoldless constructs from MSCs, as well as the potential for these constructs to serve a role in bone regeneration applications. Scaffoldless constructs have also been used to study dental pulp regeneration as an endodontic therapy. In one study, Syed-Picard et al formed scaffoldless constructs from dental pulp cells (DPCs). These constructs were positioned within the canal of human tooth root segments and implanted subcutaneously in mice where their pulp regenerative potential was assessed [53]. These studies highlight the potential for scaffoldless constructs to be used for tissue regeneration; however, to our knowledge, scaffoldless constructs have not yet been used to study the effects of novel materials (e.g. degradable Mg alloys) on a surrounding cell population. With this approach, we

are able to study a clinically relevant human cell population in a relatively low cost animal model, thus providing an efficient method of evaluating Mg implants in vivo.

In the present study, we began evaluating the Mg implants by measuring their degradation behavior using microCT. Unlike traditional weight loss methods, microCT is non-destructive and does not disrupt the alloy-tissue interface [27, 57, 72]. Through microCT we observed a reduction of underlying Mg volume accompanied by corrosion product formation at the surface. These observations are consistent with previous work by our group and others assessing Mg alloys in subcutaneous, intramuscular, and boney environments [15, 16, 26, 57, 72, 86, 109, 110]. The formed corrosion layer provides relatively weak surface passivation when compared to that of other corroding metals [27, 114]; however, in the present study we observed a significant reduction in Mg corrosion rate overtime. We hypothesize that this corrosion protection was caused not only by the oxide layer formation, but also by Ca and P precipitation on the surface. This precipitation occurs as the pH around the degrading Mg implants rises, drawing Ca and P from circulating fluids [27]. Unlike the Mg oxide layer, this CaP deposition is relatively stable and can inhibit further Mg degradation.

In addition to surface passivation, corrosion layer formation facilitates protein and cell adhesion. In the present study, we observed mouse and human cells at the alloy-tissue interface, adjacent to the corrosion layer. In addition, we observed expression of osteogenic proteins. Osteogenic proteins such as OC, OPN, and DMP1 play important roles in matrix mineralization and are commonly used as markers of osteogenic differentiation. Expression of these proteins was previously assessed using our scaffold-based model [57]; however, in the present study we observed differences in protein expression and localization. For instance, in our previous work we observed OC and DMP1 approximately 100 μm away from the degrading alloys.

Furthermore, these proteins were only observed in samples with implanted hBMSCs and not in samples without hBMSCs. We speculated that these observations indicated a role of the hBMSCs in the observed OC and DMP1 expression. However, in the present study we observed OC and OPN expression directly at the alloy-tissue interface. In addition, this protein expression was observed within all samples, including those without hBMSCs. These results suggest that the hBMSCs are not necessary to facilitate osteogenic protein expression by native cells in contact with degrading Mg alloys within the subcutaneous space. Furthermore, these observations shed light on the possible role of the corrosion layer in the overall biological response to Mg implants.

Previously, we speculated that the biological effects of Mg implants were primarily a result of Mg ion release into surrounding tissue. Various in vitro studies have been performed to simulate this scenario using Mg extracts and salts such as $MgSO_4$. These studies have revealed important effects of Mg on cell behaviors such as proliferation and differentiation [70, 71, 76, 115, 116]; however, less is known about effects of the corrosion layer on cell behavior. To better understand these effects, we must consider the corrosion layer composition. Several studies have investigated the degradation behavior and corrosion product formation of various Mg alloys. Among the corrosion products identified is $Mg(OH)_2$. Janning et al began investigating the in vivo response to $Mg(OH)_2$ in rabbit bone [117]. Using $Mg(OH)_2$ implants, they observed a local increase in bone mass around the slowly degrading $Mg(OH)_2$. These results indicated that $Mg(OH)_2$ plays a role in the enhanced bone growth observed around Mg alloys in vivo. However, Janning et al also acknowledged the potential influence of local alkalosis on bone formation. This rise in pH is a result of Mg degradation and can cause Ca and P deposition, as was observed in the present study [26, 27, 57, 118]. Detailed assessments of this deposition have

demonstrated that various phases of CaP can be formed on Mg alloys [119, 120]. For instance, while studying the degradation behavior of Mg alloy AZ31B, Jang et al noted octacalcuim phosphate (OCP) and HA deposition on the alloys. Furthermore, they observed that at a higher pH, HA was formed, while OCP was formed at a lower pH [119]. In the present study, the phase of deposited CaP was not evaluated; however, it is possible that this precipitation affected local cell differentiation.

Interestingly, we have previously observed CaP precipitation on Mg implants without subsequent osteogenic differentiation of native mouse cells [57]. The dichotomy in observations obtained with the collagen scaffold model (previously reported) and the scaffoldless model (presented herein) suggests that the cellular environments studied (collagen sponge versus endogenous ECM) can significantly affect cellular behavior. For instance, in the present study both the implanted hBMSCs and native mouse cells were in contact with the degrading Mg and corrosion product. Alternatively, with our scaffold-based model it is possible that the collagen partially impeded cell contact with the Mg and corrosion product. As such, the surrounding cell populations were likely exposed to a gradient diffusion of soluble factors. In the present study, the surrounding cell populations were exposed to the Mg and corrosion product by direct contact as well as a diffusion of soluble factors. This difference in cellular environment and material exposure could be responsible for the differences in our observations of cell differentiation.

Although the osteoinductive potential of Mg ion is unknown, the osteoconductivity and osteoinductivity of CaPs have been widely studied [3, 118, 121-123]. Typically, this osteoinduction process involves stem cell adhesion to the material surface (2-4 weeks), cell proliferation and differentiation (3-5 weeks), matrix formation (4-6 weeks), matrix mineralization (6-8 weeks), and bone formation and remodeling (8-10 weeks) [3]. In the present

study, we observed osteogenic differentiation after 4 and 8 weeks, with no signs of subsequent bone formation. These results suggest that the degrading Mg and/or CaP layer is capable of affecting cell differentiation; however, its delayed effect indicates that its osteoinductive potential is relatively low.

Although the time course of this study was too short to observe possible bone formation, other studies have demonstrated osteoinduction following in vivo deposition of CaPs [121, 122]. For instance, early investigations of polyhydroxyethylmethacrylate (polyHEMA) sponges subcutaneous in pigs revealed heterotopic bone formation following Ca deposition [122]. In addition, osteoinduction has been reported with Ti implants which illicit apatite layer formation in vivo [121]. These results demonstrate that a broad range of inert materials can induce bone cell differentiation following CaP deposition. For these reasons, researchers have engineered various CaP coatings for inert materials to enhance their osteoinductive potential [124-126]; however, the effectiveness of these coatings is often dependent on their dissolution rate and microstructure. For these reasons, more detailed assessments of the Mg corrosion layer should be conducted to better understand its osteogenic potential.

4.7 CONCLUSION

We have developed and tested a model for assessing Mg implants in vivo which utilizes scaffoldless constructs formed from hBMSCs. In addition, we have demonstrated the efficacy of using this model to evaluate Mg implant degradation behavior and associated biological response within a clinically relevant human stem cell population. We observed gradual surface corrosion and a reduction in corrosion rate over time which corresponded with the formation of a

passivating corrosion layer at the Mg implant surface. Furthermore, we observed that hBMSCs were retained around the implants after 4 and 8 weeks. Interestingly, we observed the expression of bone proteins OC and OPN around all samples, suggesting the ability of the degrading Mg and/or corrosion layer to affect local cell behavior. Although this model was presently used to assess Mg implants for orthopedic applications, we believe it could serve as a platform which can be adapted to evaluate a broad range of materials (degradable and non-degradable), cell types, and clinical applications.

5.0 FRACTURE HEALING USING DEGRADABLE MG FIXATION PLATES AND SCREWS

5.1 ACKNOWLEDGEMENTS

The work presented in this chapter was supported by the NSF ERC RMB (grant 0812348) and has been published in the Journal of Oral and Maxillofacial Surgery [86]. All work was done in collaboration with Dr. Sayuri Yoshizawa, Dr. Kostas Verdelis, Sabrina Noorani, Dr. Bernard J. Costello, and Dr. Charles Sfeir. We would also like to thank Dr. Prashant N. Kumta and Andrew Holmes (University of Pittsburgh) for material preparation and device fabrication, Dr. Michael Epperly (University of Pittsburgh) for device sterilization, and Dr. Thomas Gilbert (University of Pittsburgh) for surgical assistance.

5.2 ABSTRACT

Internal bone fixation devices made with permanent metals are associated with numerous long term complications and may require removal surgeries. We hypothesized that fixation devices made with degradable Mg alloys could provide an ideal combination of strength and degradation, facilitating fracture fixation and healing, while eliminating the need for implant removal surgeries.

To test this hypothesis, fixation plates and screws were machined from 99.9% pure Mg and compared to Ti devices in a rabbit ulna fracture model. Mg device degradation and effect on fracture healing and bone formation was assessed after 4 weeks. Fracture healing with Mg device fixation was compared to that of Ti devices using qualitative histological analysis and quantitative histomorphometry.

MicroCT showed device degradation after 4 weeks in vivo. In addition, 2D microCT slices and histological staining showed that Mg degradation did not inhibit fracture healing or bone formation. Histomorphology revealed no difference in bone bridging fractures fixed with Mg and Ti devices. Interestingly, abundant new bone was formed around Mg devices, suggesting a connection between Mg degradation and bone formation. Taken together, our results demonstrate potential for Mg fixation devices in a loaded fracture environment. Furthermore, these results suggest that Mg fixation devices may enhance fracture healing by encouraging localized new bone formation.

5.3 INTRODUCTION

Bone fractures are extremely common, with over 6 million occurring each year in the U.S. [127]. These fractures arise from various causes such as trauma, birth defects, sports injuries, and osteoporosis. With the large aging population and high prevalence of osteoporosis, incidences of bone fractures are projected to rise in coming years [127, 128]. For these reasons, fracture treatment remains a key clinical focus within the bone tissue engineering field.

Fracture treatment often requires internal fixation devices such as plates and screws to align and stabilize bone fragments throughout healing. These devices are typically made from

inert, non-degradable metals including Ti alloys [129]. These metals were originally selected for their strength and biocompatibility, but have been shown to cause long term complications including interference with pediatric skeletal growth, pain, tissue irritation, metallosis, infection, wear debris accumulation in the liver and kidney, weakening and necrosis of surrounding bone, and bone re-fracture [17, 61, 129, 130]. To avoid these complications, devices may be removed through a second surgery, further increasing patient risk and total procedural cost [129, 131].

To circumvent problems associated with permanent metals, degradable polymers have been tried. Although the resorbable property of these materials conveys a unique advantage over permanent implants, their mechanical limitations render them inadequate for load bearing applications such as mandibular and long bone fixation [24, 26, 129, 132]. Additionally, studies have reported foreign body complications associated with these materials, likely as a result of their acidic degradation products [22, 133, 134].

Unlike permanent metals and resorbable polymers, degradable Mg alloys can provide an ideal balance of degradation and strength. The degradation of these alloys reduces risk of long term infection, eliminates the need for removal surgeries, and may promote healing through Mg ion release and gradually increasing load to the healing bone [26, 74, 79, 135]. Unlike permanent metal ion generation which can lead to long term infection, Mg ion is found naturally in the body, half of which is stored in bone [61, 129, 136]. Compared to currently used permanent metals, Mg alloys have a low density, high fracture toughness, and compressive strength more similar to cortical bone [15, 26, 34, 61]. These bone-like properties reduce adverse stress shielding effects, and make Mg alloys suitable for a broad range of clinical applications including load bearing mandibular fixation. Furthermore, through variations in processing techniques, these alloys can be engineered to match desired mechanical and degradation

properties [26, 61, 79]. Taken together, Mg alloy fixation devices have the potential to not only support, but enhance fracture healing while avoiding long term complications.

Recent investigations of Mg alloys in vivo have highlighted their potential as bone fixation materials. For example, studies have shown high mineral apposition rates, increased bone mass [26], and enhanced neo-formation of bone tissue [135] surrounding Mg alloy rods implanted in bone. These results suggest that degrading Mg alloys may induce bone cell activation in vivo. Recently, this mechanism was explored in a study performed by our group showing the effect of Mg on signaling pathways involved in bone formation [137]. Furthermore, studies assessing Mg alloys in vivo have shown good biocompatibility and minimal inflammation for both slow and fast degrading alloys [26, 40, 74, 135]. Overall, these studies suggest that Mg alloys have the ability to serve as ideal materials for fracture fixation devices; however, to our knowledge there have been no reported studies testing these materials in a fracture environment. For this reason, we have conducted a study to evaluate the effects of degrading Mg fixation plates and screws on fracture healing in a load bearing rabbit ulna. In this study, degradable Mg devices were compared to clinically used Ti devices. Device degradation, fracture healing, and new bone formation were assessed.

5.4 MATERIALS AND METHODS

5.4.1 Device development

Mg plates and screws were designed and machined from 99.9% pure Mg (Goodfellow, Coraopolis PA). Titanium plates and screws were obtained from a Leibinger CMF Modular

Mandibular Plating System kit (Stryker, Kalamazoo MI). Prior to implantation, Mg devices were cleaned through sonicated washes in pure acetone and ethanol for 10 minutes each, and sterilized with gamma radiation ($2x10^6$ cGy, 23.5 Gy/min, cesium 137 source, Mark I 68, JL Shepherd and Associates, San Fernando CA) [138]. Titanium devices were sterilized using steam sterilization.

5.4.2 Surgical procedure

All animal studies were approved by the University of Pittsburgh's Institutional Animal Care and Use Committee. Five skeletally mature New Zealand White rabbits were used for this study. Prior to surgery, animals were anesthetized with isoflurane. Forearms were shaved and disinfected, and ulnae were exposed through sharp dissection. Two ulnar osteotomies were created using a hand-held rotating saw (0.5-1 mm thick) approximately 15 mm apart. The central bone fragment was briefly removed to ensure complete osteotomies. This bone fragment was then re-aligned, and secured at the proximal and distal ends with either a Ti or Mg plate and screw set. Each plate and screw set consisted of 1 plate and 2 screws. Sets were placed carefully to ensure complete separation without device contact. After fixation, incisions were closed in layers and left un-casted.

5.4.3 X-ray and MicroCT

All animals received biweekly x-rays to monitor device fixation and fracture healing (Ultra HF Generator, Vetel Diagnostics, San Luis Obispo CA). Animals were sacrificed after 4 weeks, and their forearms were extracted and scanned using microCT (VivaCT40, Scanco Medical AG, Brüttisellen Switzerland). Scans were performed with an x-ray voltage of 70 kV, anode current

of 114 μA, and integration time of 250 ms (25 μm isotropic voxel). MicroCT analysis was performed using Scanco software. Mg devices were segmented from surrounding tissue based on distinct density differences which were identified as inflection points within the voxel mineral density histogram as previously described [109]. These inflection points were used to define upper and lower thresholds for the Mg devices, and were verified by visual inspection. 2D slices and 3D reconstructions were created to evaluate fracture healing, device degradation, and new bone formation.

5.4.4 Histological assessment

All samples were formalin fixed and embedded in Technovit® 9100 New plastic (Heraeus Kulzer, Hanau Germany) to allow sectioning and histological analysis without decalcification or Mg device removal. After polymerization, embedded samples were carefully cut in half to separate the Mg and Ti devices. Titanium plates and screws were carefully removed from the bone by deacrylating the plastic covering the devices. After Ti device removal, screw holes and exposed bone were re-embedded with Technovit® 9100 New. All samples were then trimmed and sectioned using a Leica RM2255 microtome (Leica, Buffalo Grove IL) with tungsten-carbide blade. Samples were stained with Masson's Trichrome to visualize bone morphology and quantify new bone formation.

5.4.5 Histomorphometry

Histomorphometry was used to quantify newly formed bone at the osteotomy sites beneath the fixation devices. Stained sections were imaged using a Nikon Eclipse TE2000 bright field

microscope (Nikon, Mellville NY). Images were imported using ImageScope (Aperio, Vista CA) and extractions were made containing the fracture sites. The amount of new bone between the proximal and distal cortical bones was then quantified using BioQuant (BioQuant Image Analysis Corporation, Nashville TN). Pre-existing cortical bone was identified using polarized light microscopy and excluded from these calculations to ensure quantification of new bone only.

5.4.6 Statistical analysis

Groups were compared using a student's t-test. Graphical representations reflect mean ± standard deviation.

5.5 RESULTS

5.5.1 Device implantation and fracture fixation

Mg fixation plates and screws were designed and machined from 99.9% pure Mg, and compared to clinically used Ti devices of a similar size (Figure 20 A). These devices (5 Ti and 5 Mg) were used to secure 10 ulnar fractures in New Zealand White rabbits. All radii were left intact during surgery, providing a load bearing environment throughout healing. X-rays showed that all fixation devices provided adequate re-approximation and reduction of bone fragments throughout healing. Due to Mg's relatively low density, healing fractures and re-aligned bone fragments were clearly visible underneath Mg plates through x-ray (Figure 20 B).

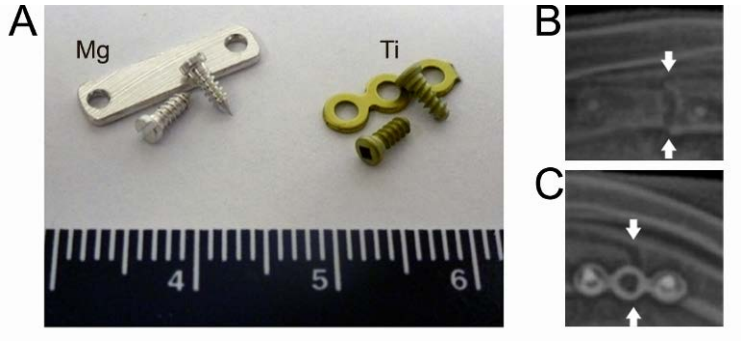

Figure 20. Mg and Ti devices before and after implantation.

Mg and Ti plates and screws prior to implantation (A). X-ray 1 week after implantation showing fixation with a Mg device (B) and radio-opaque Ti device (C). White arrows indicate location of osteotomies.

5.5.2 Device degradation

MicroCT was used to assess Mg device degradation. Devices were scanned before implantation and after removal, and 3D renderings were produced to visualize changes in volume as a result of corrosion (Figure 21). MicroCT 3D renderings showed an overall volume loss of Mg plates and screws after 4 weeks in vivo. Increased volume loss was observed in the threaded screw shaft region. Minimal plate volume loss was observed. Mg device degradation was also observed through localized gas accumulation. This gas accumulation was observed as small pockets surrounding degrading Mg devices (Figure 22). These gas pockets did not cause tissue swelling or inflammation, and did not inhibit fracture healing or new bone growth.

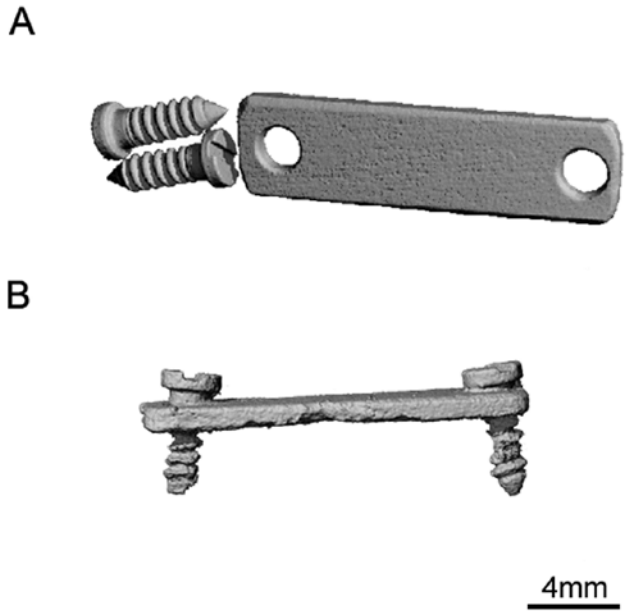

Figure 21. MicroCT 3D renderings of Mg devices before and after implantation.

Original plate and screws prior to implantation (A) and degraded plate and screws after four weeks (B).

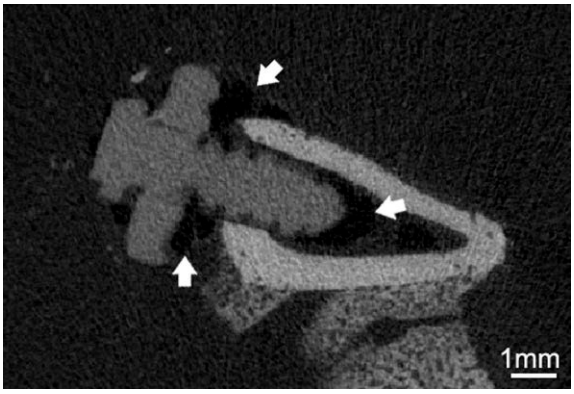

Figure 22. MicroCT 2D view of Mg plate and screw in bone showing gas generation.

White arrows show gas as a result of ongoing device degradation.

5.5.3 Fracture healing

All devices were well tolerated by the rabbits. All animals resumed normal ambulatory function without casting after surgery, providing a load bearing environment for the healing fractures. X-ray, microCT, and histological analyses showed uninhibited fracture healing in the direct presence of degrading Mg devices. After 4 weeks, all fractures showed bone bridging the fracture site and healing cortical bones. Histomorphometry revealed no significant difference in the amount of new bone at fracture sites fixed with Mg or Ti devices (Figure 23).

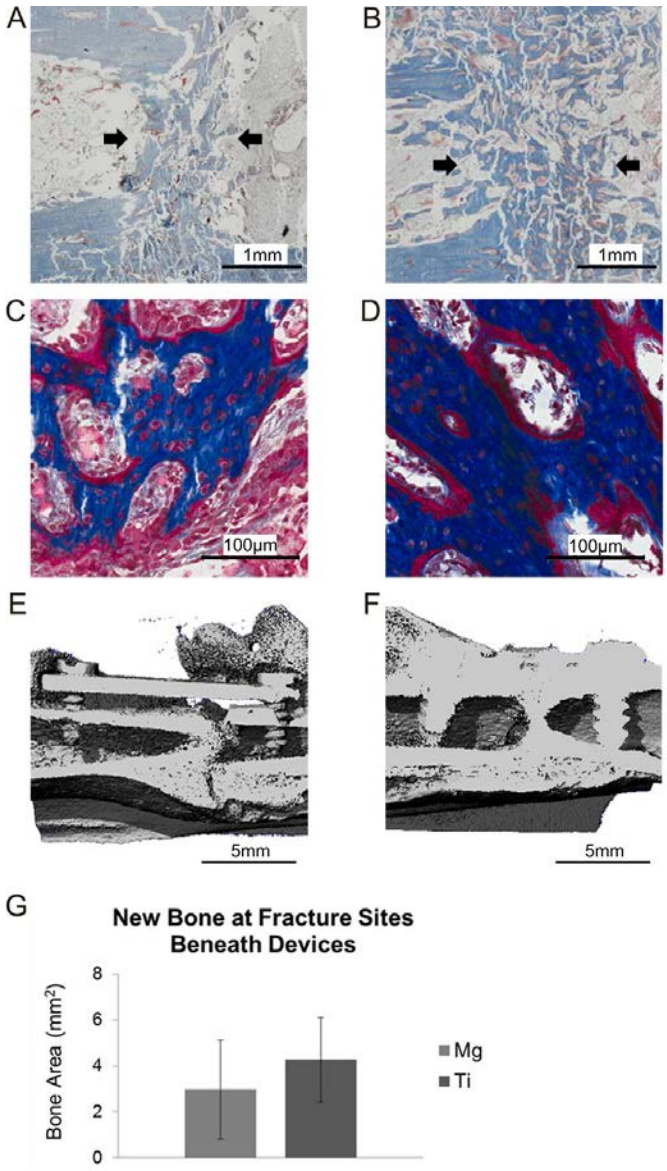

Figure 23. Histological staining and microCT showing fracture healing with Mg devices.

Low magnification images of Masson's Trichrome stained sections show newly formed bone bridging fractures sites fixed with Mg (A) and Ti (B) after 4 weeks (cracking shown reflects histological artifact). Higher magnification images of Mg (C) and Ti (D) devices show osteocytes and active osteoid within new bone at the fracture sites. MicroCT 3D renderings provide an alternative visualization of new bone bridging fracture sites fixed with Mg (E) and Ti (F) devices after 4 weeks. Due to its high density, Ti and surrounding bone appear brighter through microCT than Mg; however, similar rates of bone bridging were observed. Histomorphometry of bone bridging at fracture sites shows no difference between Mg and Ti groups (G).

5.5.4 New bone formation

Interestingly, large areas of new bone were observed above and around degrading Mg devices. In many cases, this new bone formation nearly encased the Mg device, with high levels of bone-device contact. Histological staining showed mature osteocytes and active osteoid throughout these regions. This overgrowth of bone was not observed around Ti devices (Figure 24).

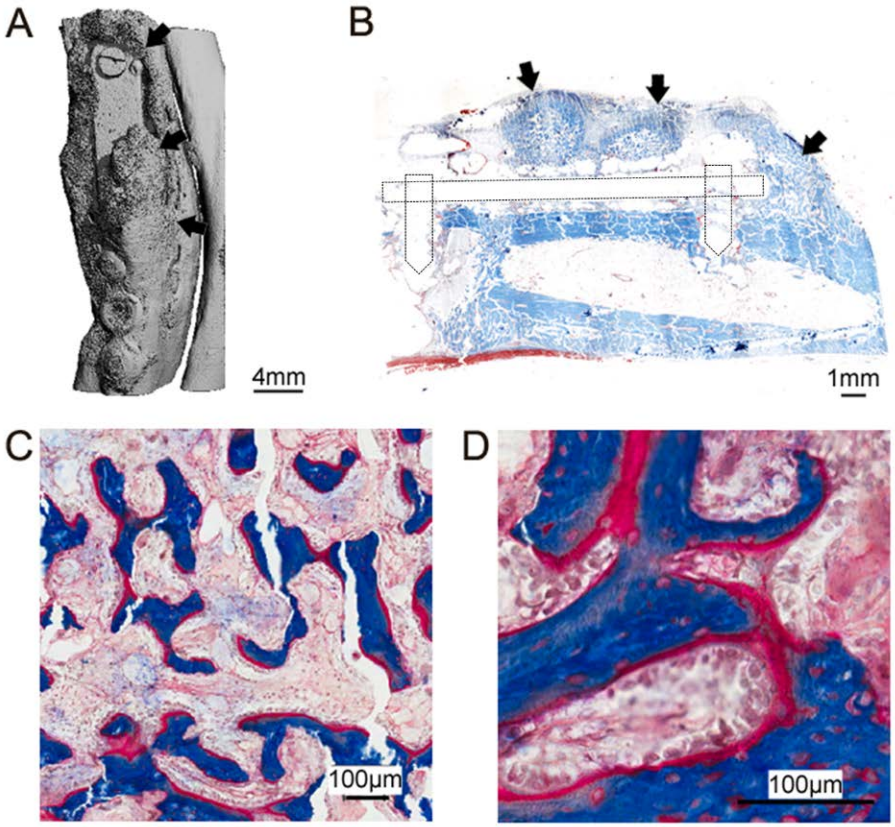

Figure 24. MicroCT and histological staining showing new bone formation around Mg devices.

A 3D rendering of the ulna with Mg and Ti devices shows new bone growth (black arrows) on and around the degrading Mg device (A). A Masson's Trichrome stained section shows bone overgrowth (black arrows) around a Mg device (B). Dotted lines depict approximate location of plate and screws not retained during sectioning. Higher magnification images show osteocytes and osteoid within this region (C & D).

5.6 DISCUSSION

Due to long term complications associated with permanent implants, there is a growing interest in degradable metals for bone fixation. However, to our knowledge there have been no reported studies evaluating these materials as fixation plates and screws in vivo. For this reason, we investigated Mg plates and screws using a rabbit ulnar osteotomy model. This model has previously been used to study bone repair and effects of implants on fracture healing [139-141]. Using this model, we assessed the preliminary efficacy of Mg fixation devices in a load bearing fracture environment. We hypothesized that degradable Mg fixation devices would provide adequate stabilization to facilitate physiological healing despite ongoing device degradation.

In order to evaluate device degradation, microCT was performed. This non-destructive technique has previously been used to study the volume loss of Mg implants in vivo [109, 135]. By segmenting Mg devices from surrounding tissue, we were able to observe degradation throughout the devices in 2D and 3D. Interestingly, volume loss appeared greater for screws than plates, which is possibly attributed to the high surface area, particularly within the threaded shaft region. Device degradation was also observed through small gas pocket formation around the Mg devices. This gas formation is a known product of Mg degradation and has been shown to closely follow Mg implant volume loss [27]. For instance, Kraus et al used microCT to study gas formation and Mg pin degradation in rat femora [135]. They observed gas pocket formation through 12 weeks post-operative; however this gas was largely resorbed by surrounding tissue, and did not cause adverse effects on bone healing. Similarly, in the present study gas pocket formation did not interfere with fracture healing or new bone formation. We hypothesize that overtime, this gas formation would slow as the rate of Mg device degradation plateaued.

Importantly, in the presence of ongoing device degradation and Mg release, our results showed no inhibition of fracture healing or new bone formation. Based on microCT, histological staining, and histomorphometry, we observed similar healing outcomes for fractures fixed with Mg and Ti devices alike. Samples from both groups included newly formed bone with mature osteocytes and active osteoid. In addition, some samples also showed connective tissue and hypertrophic cartilage at the fracture site, indicative of immature healing. However, these observations are expected 4 weeks post-operative, with full union of simple rabbit fractures typically not occurring until six to eight weeks post-operative [140].

In addition to fracture healing, we observed abundant new bone formation above degrading Mg, but not Ti, plates and screws. Increased bone formation and bone density have previously been reported by other groups using Mg-based rods and pins [26, 74, 129, 135]. For example, after implanting two types of Mg pins in rat femora, Kraus et al observed enhanced local bone formation during cortical bone healing. This bone growth later slowed as the Mg pins degraded [135]. In the present study, we observed new bone formation not only adjacent to the healing cortical layer, but also above and around Mg devices. In most cases, this bone growth nearly encased the Mg device, with high levels of bone-device contact. In contrast, no new bone growth was observed over Ti plates and screws.

Taken together, our observations of fracture healing and new bone growth around Mg fixation devices suggest that degrading Mg may positively affect bone formation. Previously, other groups have linked Mg with increased osteoblastic activity, ultimately leading to increased mineral apposition in vivo [26, 74]. Though the mechanism of Mg induced bone formation is not yet fully understood, recent investigations have highlighted the important role Mg in activating osteogenic signaling pathways [137]. These mechanistic data established additional roles of Mg

in bone biology, and support the use of these materials in craniomaxillofacial and orthopedic applications.

5.7 CONCLUSION

This study provided important insight into the ability of degradable Mg alloys to serve as bone fixation devices. We demonstrated that pure Mg fixation plates and screws not only facilitated physiological fracture healing, but supported new bone formation around the degrading devices. These biological evaluations support the use of Mg in craniomaxillofacial and orthopedic applications, providing a load bearing therapy which reduces risk of long term complication and eliminates the need for device removal.

6.0 IN VIVO STUDY OF MAGNESIUM PLATE AND SCREW DEGRADATION AND BONE FRACTURE HEALING

6.1 ACKNOWLEDGEMENTS

The work presented in this chapter was supported by the NSF ERC RMB (grant 0812348), Commonwealth of Pennsylvania (SAP4100061184), University of Pittsburgh's Center for Craniofacial Regeneration, and the Edward R. Weidlein Chair Professorship funds of Prashant N. Kumta from the Swanson School of Engineering University of Pittsburgh, and has been published in Acta Biomaterialia [110]. All work was done in collaboration with Dr. Sayuri Yoshizawa, Dr. Kostas Verdelis, Nicole Myers, Dr. Bernard J. Costello, Da-Tren Chou, Dr. Siladitya Pal, Dr. Spandan Maiti, Dr. Prashant N. Kumta, and Dr. Charles Sfeir. We also thank Andrew Holmes (University of Pittsburgh) for device fabrication, Dr. Michael Epperly (University of Pittsburgh) for device sterilization, and Dr. Alejandro Almarza (University of Pittsburgh) for assistance with mechanical testing.

6.2 ABSTRACT

Each year, millions of Americans suffer bone fractures, often requiring internal fixation. Current devices, like plates and screws, are made with permanent metals or resorbable polymers.

Permanent metals provide strength and biocompatibility, but cause long-term complications and may require removal. Resorbable polymers reduce long-term complications, but are unsuitable for many load-bearing applications. To mitigate complications, degradable Mg alloys are being developed for craniofacial and orthopedic applications. Their combination of strength and degradation make them ideal for bone fixation. Previously, we conducted a pilot study comparing Mg and Ti devices with a rabbit ulna fracture model. We observed Mg device degradation, with uninhibited healing. Interestingly, we observed bone formation around degrading Mg, but not Ti, devices. These results highlighted the potential for these fixation devices. To better assess their efficacy, we conducted a more thorough study assessing 99.9% Mg devices in a similar rabbit ulna fracture model. Device degradation, fracture healing, and bone formation were evaluated using microcomputed tomography, histology and biomechanical tests. We observed device degradation throughout, and calculated a corrosion rate of 0.40 ± 0.04 mm/year after eight weeks. In addition, we observed fracture healing by eight weeks, and maturation after 16 weeks. In accordance with our pilot study, we observed bone formation surrounding Mg devices, with complete overgrowth by 16 weeks. Bend tests revealed no difference in flexural load of healed ulnae with Mg devices compared to intact ulnae. These data suggest that Mg devices provide stabilization to facilitate healing, while degrading and stimulating new bone formation.

6.3 INTRODUCTION

Each year there are over 6 million bone fractures reported in the U.S. [142], approximately one third of which require internal fixation devices to help facilitate healing [14]. Currently, permanent and inert metals like Ti alloys and stainless steel remain the gold standard for internal fixation devices; however, these materials are associated with various long-term complications such as interference with skeletal growth (particularly for pediatrics), tissue irritation, infection, interference with radiological imaging, and unfavorable aesthetics (primarily for craniofacial implants) [15-18, 70]. For these reasons, permanent fixation devices may necessitate invasive removal surgeries, increasing patient burden and risk, and draining valuable hospital resources [59, 60]. To mitigate these concerns, resorbable polymer devices have been developed; however their mechanical properties often limit them as viable options for load-bearing applications [27]. Furthermore, studies have reported long-term foreign body reactions associated with polymeric device degradation, likely due to their acidic degradation products [23, 70, 143]. For these reasons, there remains a need to develop novel fracture fixation devices which mitigate long-term complications and eliminate the need for removal surgeries.

Unlike permanent metals and resorbable polymers, degradable Mg alloys provide a unique combination of strength and degradation. For these reasons, Mg alloys are being explored for various craniofacial and orthopedic applications. Interestingly, Mg alloys were first attempted as orthopedic devices over a century ago. Early Mg-based devices proved to be biocompatible, with low rates of infection; however, rapid degradation of Mg that is characteristic and to be expected with the current metallurgical knowledge known to date caused excessive hydrogen gas formation which ultimately prevented their clinical success [35, 99]. Since these initial investigations, numerous advancements in alloying and corrosion control have been achieved.

These advancements allow Mg and its alloys to be tailored to accommodate the desired mechanical properties and degradation behavior.

Numerous in vitro and in vivo studies have demonstrated the biocompatibility and osteoconductivity of these materials. Indirect assays, in which cells are exposed to media treated with Mg corrosion products, have shown cell viability with low concentrations of degradation product [70, 71, 99]. Similarly, direct assays, in which cells are cultured directly on Mg alloys, have shown cytocompatibility in the presence of ongoing Mg degradation [70, 71, 99]. Importantly, studies assessing Mg implants in endosseous sites, such as guinea pig [26], rat [28], and rabbit femora [72] have shown biocompatibility and normal foreign body response for various Mg alloys. In addition, several studies have shown high mineral apposition rates and increased bone mass and mineral density surrounding Mg implants in bone [26, 27, 117, 144].

These data support the use of Mg implants as orthopedic devices; however there remains a lack of in vivo data assessing these materials as actual fixation plates and screws. For these reasons, we previously conducted a pilot study to evaluate Mg fixation plates and screws using a rabbit ulna fracture model [145]. In the pilot study, we compared 99.9% Mg plates and screws to clinically-used Ti devices, studying the effect of Mg degradation on fracture healing. Our pilot study results showed no significant difference in healing of fractures fixed with Mg or Ti devices. Interestingly, we also observed bone formation above the Mg, but not Ti, plates and screws.

In order to validate this pilot study data, we have conducted a more thorough follow-up assessment presented herein. In the present study, we aim to test our hypothesis that ongoing Mg device degradation will continue to stimulate osteogenic differentiation of local cell populations such as hBMSCs and/or periosteal cells. In turn, this differentiation will result in local bone

formation, providing additional fracture stabilization. Through this process, it is anticipated that Mg devices will be gradually replaced by bone growth, mitigating risk of long-term complications and device removal surgeries. To test this hypothesis, we have performed a thorough assessment of the degradation behavior and biological effect of Mg fixation devices. Specifically, we have designed and tested Mg fixation plates and screws in a rabbit ulna fracture model. Our results have confirmed our pilot study observations of new bone formation around Mg devices, especially above the devices where the periosteum and muscle tissue was present. In addition, we observed no inhibition of fracture healing. Mechanical testing demonstrated that healed fractures fixed with Mg devices responded similarly to healthy controls when subject to three point bending. Taken together, these data demonstrate the efficacy of Mg fixation devices in a load bearing fracture site.

6.4 MATERIALS AND METHODS

6.4.1 Device development

Fixation devices (Figure 25) were machined with 99.9% pure Mg (Goodfellow, Coraopolis, PA). All devices were designed to accommodate rabbit ulnar geometry. Plates were 20x4.5 mm with a thickness of 1-1.5 mm. Screws were 7 mm in length, with a shaft outer diameter of 1.75 mm and shaft inner diameter of 1 mm. Prior to implantation, devices were cleaned by sonicated washes in pure acetone and ethanol, followed by sterilization with gamma radiation ($2x10^6$ cGy, 23.5 Gy/min, cesium 137 source, Mark I 68, JL Shepherd and Associates, San Fernando, CA).

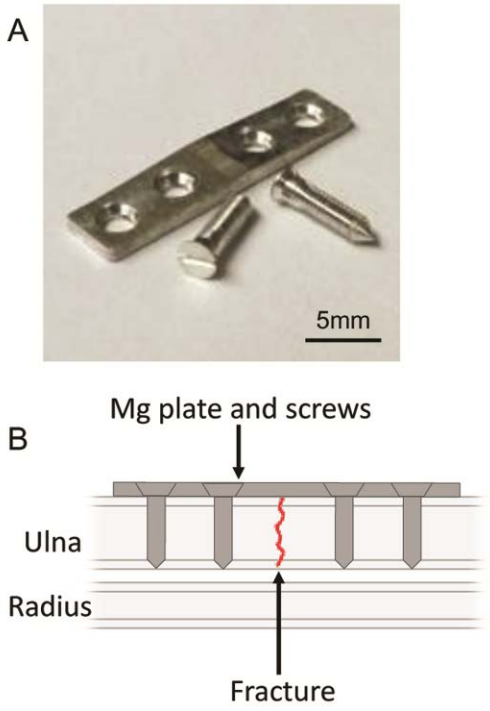

Figure 25. Mg fixation plate and screws before implantation.

Digital image shows devices before implantation (A). Schematic shows device placement in fractured ulna (B).

6.4.2 Surgical procedure

All animal experiments were approved by the University of Pittsburgh's Institutional Animal Care and Use Committee. 12 New Zealand White rabbits (19 weeks of age, 3.5±0.2 kg) were used in this study. Both ulnae (right and left) of all animals were used, providing a total of 24 surgical sites. Each time point consisted of 6 rabbits (12 surgical sites). Prior to surgery, animals were anesthetized and forearms were shaved and disinfected. A 2 cm incision was made over the ulna. Overlying skin and muscle was carefully retracted to expose the ulna. A complete ulnar osteotomy (0.5-1 mm thick) was created using a hand held drill. A fixation device consisting of one plate and four screws was then placed to stabilize the fracture. The incision was closed in

layers with sutures and left un-casted. Animals were monitored daily for general behavior, movement, and food and water intake. In addition, forearms were checked thoroughly by visual inspection and gentle palpation for signs of infection or subcutaneous gas pocket formation. Based on consultation with the University of Pittsburgh's Division of Laboratory Animal Resources, observable gas pockets were removed with a sterile syringe. All gas pocket formations and removals were documented throughout the study.

6.4.3 X-ray imaging

X-ray imaging was used to monitor device placement and fracture healing throughout the study. All animals received x-rays immediately following surgery and every 2 weeks thereafter.

6.4.4 Three point bend testing

A three point bend test was used to evaluate the relative strength of the ulnae after 16 weeks (n=9 ulnae). Prior to testing, forearms were carefully dissected and overlying soft tissue was removed. For all samples, the radius and ulna were fused, preventing us from accurately separating the bones for testing. To exclude radial contributions from the test, two transverse cuts were created on either side of the fracture site and remaining device (4 cm apart) using a low speed saw and diamond blade (Buehler USA, Lake Bluff, IL) as previously described [50]. An Instron 5564 (Instron USA, Norwood, MA) with 2 kN load capacity was used for testing. For each sample, the radius and ulna were positioned on the same horizontal plane on two lower stabilizing points positioned 5 cm apart. The fracture site and radial cuts were centered within these points. One upper moving point was positioned at the center of the two lower points. Test parameters were

modified from previous studies, including a 1 N pre-load, loading speed of 5 mm/min, and stop point of 0.5 mm flexural extension (previously determined to be non-destructive) [50]. The flexural load at 0.5 mm extension was recorded for each sample. Intact ulnae were similarly prepared and used as healthy controls.

6.4.5 MicroCT

High resolution microCT was used to evaluate device degradation and new bone formation. Devices were scanned before implantation with a VivaCT40 (Scanco Medical AG, Bruttisellen, Switzerland) and 10.5 μm voxel size (55 kV, 72 μA). In addition, devices were scanned after 8 and 16 weeks (n=4 per time point) using a SkyScan1172 (Bruker-MicroCT, Kontich, Belgium) scanner with a 10 μm voxel size, 79 kV tube potential and 125 μA tube current. 3D volumes of the scanned samples were generated from acquired 2D lateral projections using Reconn software (Bruker-MicroCT, Kontich, Belgium). For analysis, scanned bone volumes were digitally reoriented using the SkyScan DataViewer software, and user-defined remaining Mg and corrosion product regions of interest were generated using the SkyScan CTAn software (version 1.13.5.1) as previously described [23, 24]. Mg devices were segmented from surrounding soft and hard tissues based on the absorption coefficient (equivalent to mineral density) of remaining Mg and corrosion product. The relative x-ray absorption coefficients within each of these two layers are distinctly different, generating a clear interface between the two, as well as between the corroded product and background as previously described [89]. These interfaces were identifiable as inflection points within the distribution of mineral densities histogram from a region of interest including both remaining Mg and corrosion product. These inflection points

were used to define thresholds for the Mg and corrosion product, and were verified by visual inspection.

Following segmentation, volume quantifications were obtained to evaluate device degradation and bone formation. Corrosion rate was calculated through the microCT-evaluated Mg volume loss using Equation 1, where CR is corrosion rate in mm/yr, ΔV is change in Mg volume in mm^3, A is surface area in mm^2, and t is time in years [25]. Devices were considered in their entirety, and also divided into head and shaft regions with respective regions of interest defined. The head region was defined as any area of the screw above the bottom edge of the plate, while the shaft region was defined as any area of the screw below the bottom edge of the plate.

In addition to device volume change, new bone formation around the devices, as well as bone-device contact was assessed though microCT. New bone around the devices was defined as any bone above the bottom of the plate. Importantly, this region originally contained only muscle and soft tissue; therefore, any bone observed within this region is newly formed. Bone contact throughout the screw shafts was calculated as the intersection surface area between Mg and bone using CTAn.

$$CR = \Delta V/(At) \quad (1)$$

6.4.6 Histological assessment

Samples were formalin fixed and embedded in Technovit 9100 New® (Heraeus Kulzer, Hanau, Germany). Samples were sectioned and stained with Toluidine Blue to visualize bone morphology at the fracture site, device-tissue interface, and within areas of newly formed bone.

6.4.7 Statistical analysis

Statistical analysis was performed using IBM SPSS Statistics 19 (IBM, Armonk, NY). All groups were compared using a student's t-test. For corrosion analysis, screw volumes were compared between two time points (0 and 8 weeks, n=8 screws per time point). In addition, screw volumes were compared between the head and shaft regions (0 and 8 weeks, n=8 screws per region). Plate volumes were similarly compared between two time points (0 and 8 weeks, n=2 plates per time point). For mechanical testing analysis, healed ulnae were compared to healthy controls at 16 weeks (n=9 ulnae per group). All graphical representations reflect mean ± standard deviation.

6.5 RESULTS

6.5.1 Overall animal health

All devices were well tolerated by the animals and did not cause adverse health events. Immediately following surgery, animals resumed normal movement and behavior, including weight bearing on both forearms.

6.5.2 Device degradation

Initial evidence of device degradation was observed through subcutaneous gas pocket formation. Interestingly, subcutaneous gas pocket formation was not observed in all animals. Only two

animals developed subcutaneous gas pockets over the implant site, which were easily removed with a sterile syringe without causing infection or interference with healing. Pockets consisted of gas without additional blood or fluid. Gas pocket formation was observed through 5 weeks post-operative. The largest number of removals, three, was performed during the second week, with all other weeks only requiring one removal each. No gas pocket formation was observed after 5 weeks post-operative.

High resolution microCT was used to study device degradation (n=8 screws, n=2 plates). Based on distinct material density differences, volumes of Mg and corrosion product were quantified separately. Volume quantification revealed a net loss of volume for Mg screws after 8 weeks. Mg volume was reduced by 4.41 ± 0.49 mm^3 after 8 weeks. Meanwhile, 3.35 ± 0.60 mm^3 of corrosion product was produced at the surface (Figure 26 A). Based on this change in Mg volume, the in vivo corrosion rate of our Mg screws was calculated to be 0.40 ± 0.04 mm/year. Interestingly, corrosion behavior varied between different regions of the screws. After 8 weeks, the screw head region consisted of 47.09 ± 13.76 volume percent of Mg, and 52.91 ± 13.76 volume percent of corrosion product. In contrast, the screw shaft region consisted of 75.04 ± 3.34 volume percent of Mg, and 24.96 ± 3.34 volume percent of corrosion product (Figure 26 B). Similar to the screws, the Mg plate volume was also reduced after 8 weeks. Specifically, Mg plates corroded at a rate of 0.55 ± 0.02 mm/year, resulting in 19.57 ± 0.66 mm^3 of Mg volume loss after 8 weeks (Figure 26 C). Due to extensive corrosion product formation and integration with the surrounding tissues, accurate device volume quantification after 16 weeks was not possible. However, additional Mg volume loss and corrosion product production was observed.

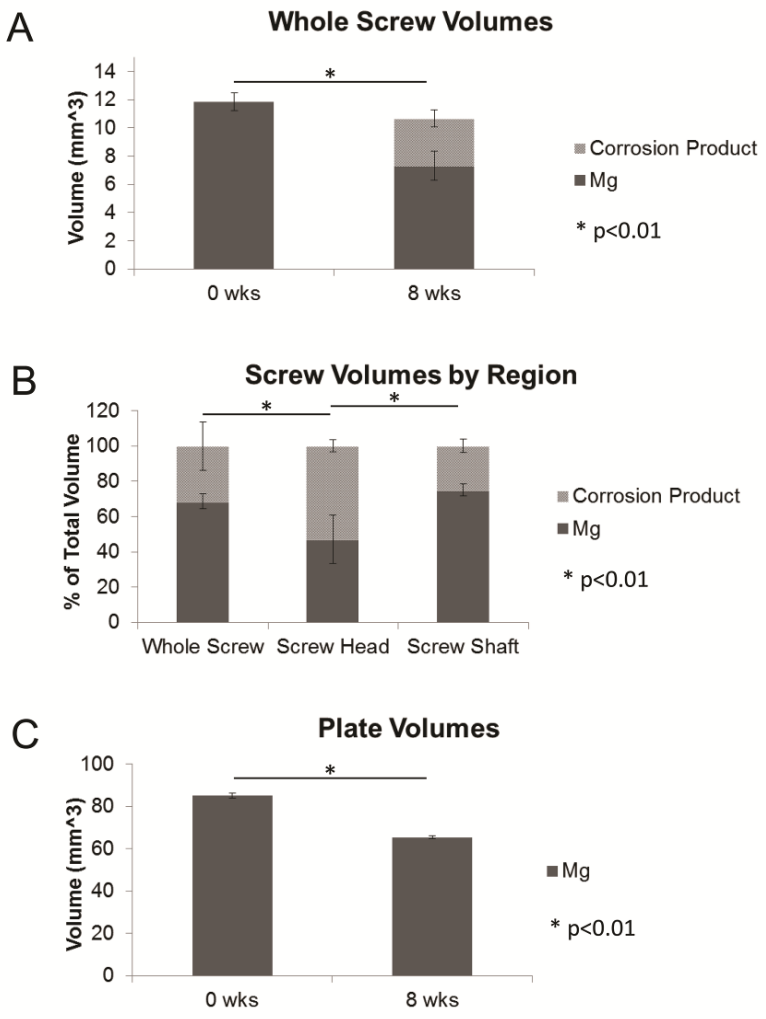

Figure 26. Mg plate and screw degradation quantification.

Screw degradation after 8 weeks was assessed by volume quantification. Due to distinct density differences, Mg and corrosion product were quantified separately for a detailed understanding of corrosion behavior. Volume quantification shows a Mg volume loss of 4.41±0.49 mm3 (* p<0.01). In addition, 3.35±0.60 mm3 of corrosion product was formed at the surface (A). Mg and corrosion product were calculated as percentages of total screw volume for the whole screw, the head region, and the shaft region. After 8 weeks, Mg represented a significantly smaller percentage of total volume within the head region when compared to the shaft and whole screw (B, * p<0.01). Concurrently, corrosion product represented a significantly greater percentage of total volume within the head region when compared to the shaft and whole screw (B, * p<0.01). Plate volume was reduced by 19.57±0.66 mm3 (* p<0.01).

6.5.3 Fracture healing

Bi-weekly x-rays showed progressive healing throughout the study (Figure 27). These observations were confirmed by microCT and histological staining after 8 and 16 weeks. After 8 weeks, fracture healing was observed as proximal and distal cortical bone union for most samples (Figure 28 A). After 16 weeks, more mature healing was observed, with full thickness cortical bone bridging at the fracture site (Figure 28 B). Histological staining showed normal bone morphology within these regions including osteocytes and osteoid (Figure 28 C-F).

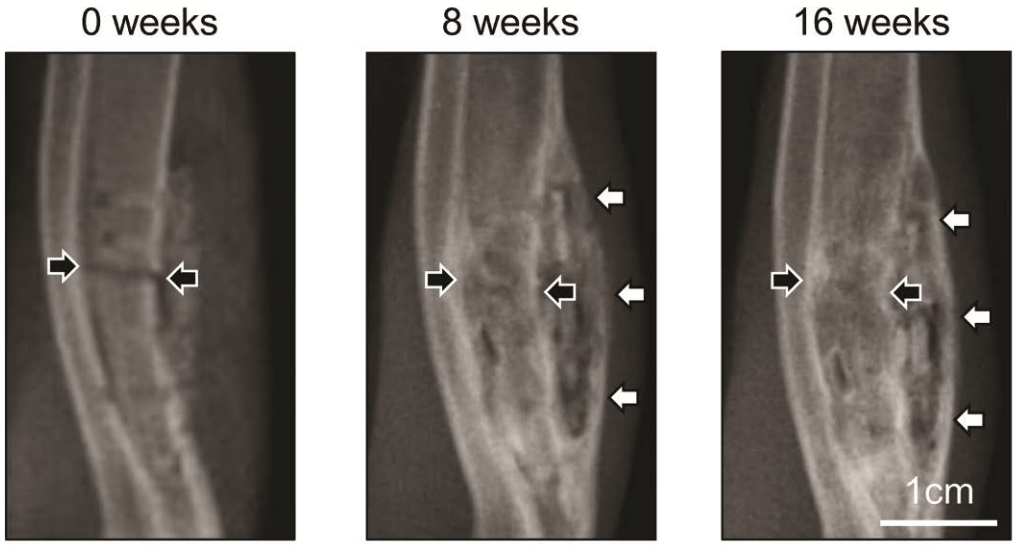

Figure 27. X-rays showing progression of fracture healing and bone overgrowth.

Fracture healing was observed by 8 weeks with further maturation by 16 weeks post-operative (black arrows). In addition, new bone was formed over the entire fixation device. Partial bone covering was observed by 8 weeks, with complete covering occurring by 16 weeks post-operative (white arrows).

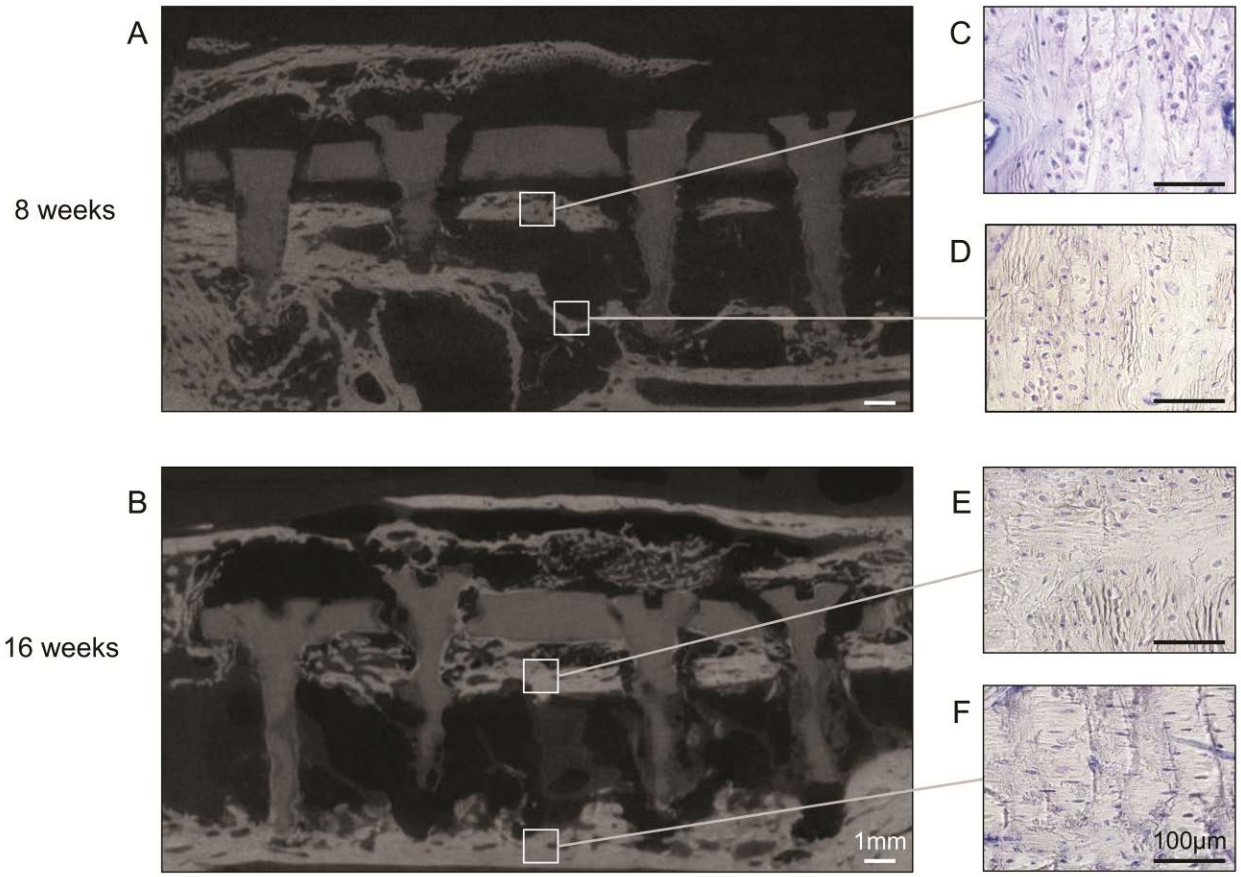

Figure 28. MicroCT and histological staining showing fracture healing.

MicroCT slices show cortical bone union after 8 weeks (A) with further maturation after 16 weeks (B). High magnification images of Toluidine stained sections show normal bone morphology within the healed cortical bones at the fracture site after 8 (C, D) and 16 weeks (E, F).

6.5.4 Bone-device contact

Bone-device contact was observed through microCT and histological staining. In the presence of ongoing corrosion, high levels of bone-device contact were observed after 8 and 16 weeks in vivo. Areas of bone-device contact were more prevalent in slower degrading regions, such as around the plate and screw heads. New bone growth was often observed around the screw head

and within the driver slot, with direct bone-device contact (Figure 29). Bone device contact along screw shafts were quantified after 8 weeks, revealing over 25% of the screw shaft surface area in contact with bone.

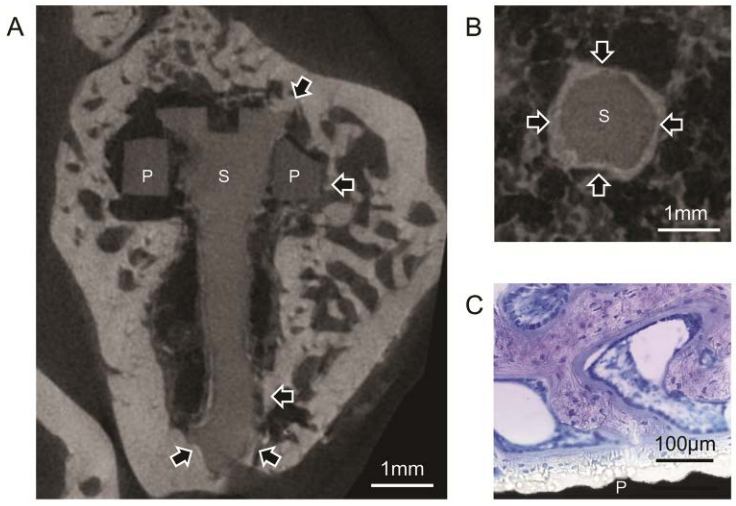

Figure 29. MicroCT and histological staining showing bone-device contact.

Interfaces of Mg devices (lower density, darker) and bone (higher density, brighter) were observed through microCT. A longitudinal slice of a Mg plate (P) and screw (S) show areas of bone contact around the screw head, shaft, and plate edge (A). A transverse slice of a Mg screw shaft (S) shows bone contact around screw perimeter after 16 weeks (B). Toluidine Blue shows bone at bone-plate (P) interface after 8 weeks (C).

6.5.5 New bone growth around Mg devices

New bone was formed over and around all Mg devices. This bone formation was observed throughout the study by x-ray, and was further assessed by microCT and histological staining after 8 and 16 weeks. After 8 weeks, new bone partially covered all Mg devices (Figure 30 A-C). After 16 weeks, this new bone completely covered all Mg devices (Figure 30 D-F). MicroCT was used to quantify the amount of new bone formed over the fixation devices. A significant

increase in overlying bone formation was observed from 8 to 16 weeks (p=0.001), with 100.20 ± 33.80 mm^3 of new bone formed within this period (Figure 30 G).

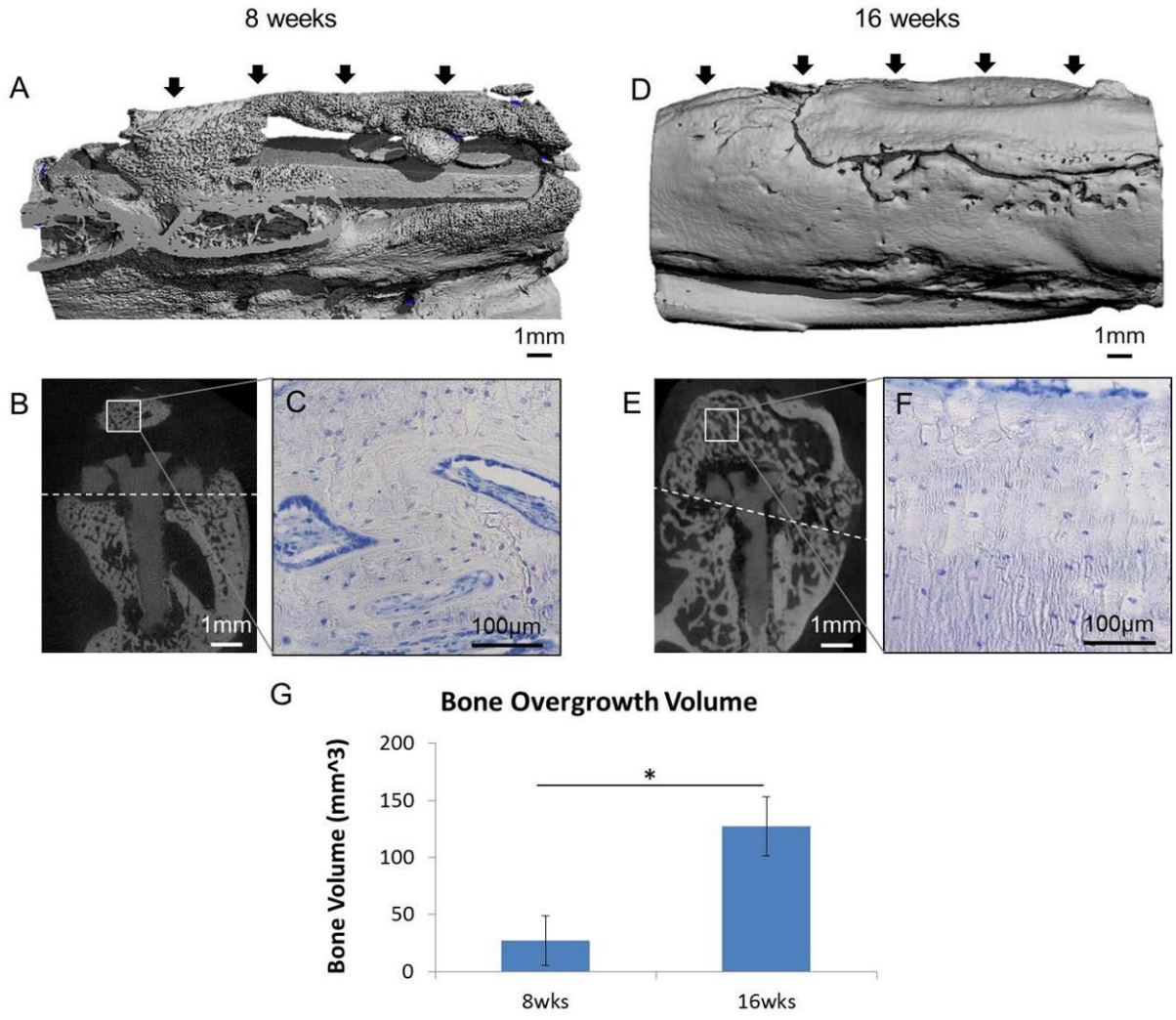

Figure 30. MicroCT and histological staining showing bone overgrowth around Mg devices.

Bone overgrowth (black arrows) was observed around degrading Mg devices. MicroCT 3D rendering after 8 weeks shows partial bone overgrowth around the degrading Mg device (A). By 16 weeks, bone overgrowth completely covered all devices (B). X-ray slices from microCT scanning highlight bone overgrowth over screws after 8 (B) and 16 weeks (E). Toluidine Blue stain shows normal bone morphology with osteocytes and osteoid within the newly formed bone (C & F). New bone overgrowth was quantified using microCT. Conservatively, bone above the plate baseline (marked with a white dotted line) was identified as new bone. A significant increase in bone was observed from 8 to 16 weeks (G, *p<0.01).

6.5.6 Bend testing

The relative structural properties of the healed ulnae were assessed by three point bend testing after 16 weeks. Bone overgrowth and degraded fixation devices were left in place for testing; therefore, results reflect the entire bone-device complex as it would be loaded in vivo. Bend test results revealed a slight, though not significant, increase in flexural load for healed ulnae fixed with Mg devices compared to intact ulnae controls (Figure 31).

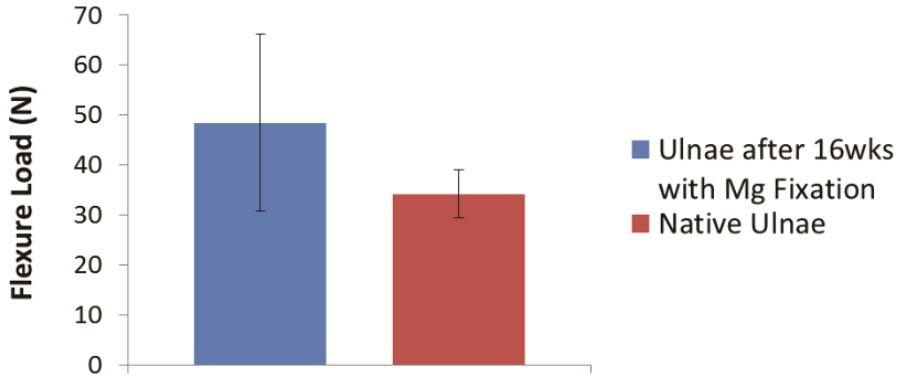

Figure 31. Three point bend test results.

Bend testing was performed on ulnae after 16 weeks and compared to healthy, un-fractured controls. Fixation devices and bone overgrowth were not removed for testing. No significant differences were observed between healed ulnae and healthy controls.

6.6 DISCUSSION

In the present study, we assessed the efficacy of degradable Mg fixation plates and screws in a loaded ulna fracture model. This model has been used to study bone repair and effects of implants and therapeutic agents on fracture healing [146-148]. Previously, our group performed a

pilot study evaluating the biological effect of Mg plates and screws. This study revealed abundant new bone formation around the degrading Mg devices, suggesting a connection between Mg degradation and bone formation. To further explore the effect of Mg on fracture healing and bone formation, we have conducted a thorough investigation of 99.9% Mg fixation plates and screws. We hypothesized that these degradable devices would facilitate fracture healing, while stimulating local bone formation.

As Mg degrades, hydrogen gas is produced. Depending on the implant's local environment and available blood flow, this gas may be cleared from the implant site without accumulation. However, rapid corrosion rate and/or insufficient gas removal may lead to accumulation. Several studies have documented gas cavity formation associated with Mg degradation [27, 42]. Kraus et al used microCT to study gas formation and Mg pin degradation in rat femora [28]. They showed gas formation closely followed Mg volume reduction. Furthermore, they showed that gas was largely resorbed by the surrounding tissue, and did not cause adverse effects on bone healing. In the present study, six gas pockets from two animals were observed over the course of the study, indicating that most gas released during device degradation was efficiently cleared from the implant site. Furthermore, the observed gas accumulation did not disrupt fracture healing, bone formation, or surrounding tissue health. It is important to note however, that reducing gas pocket formation is necessary for clinical translation. One way to achieve this could be through grain refinement, as has been previously demonstrated with Mg alloy LAE442 [149]. In the study by Ullmann et al, LAE442 rods with varying grain sizes were implanted into the medullary cavity of New Zealand white rabbits and assessed over 6 months. Their results demonstrated that grain size reduction provided slower corrosion and improved clinical tolerance. It is likely that grain refinement of the pure Mg used

in the present study (average grain size 36.9 μm) would provide similar corrosion improvements. For instance, through mechanisms such as improved passive film formation due to increased activity of reduced grain size area, and consequently, better adhesion due to increased grain boundary density [150]. As a result, gas pocket formation may be likely reduced.

In addition to hydrogen, degrading Mg produces corrosion product on its surface [27, 151]. The materials properties of the remaining Mg and corrosion product are expectedly not equal, and therefore do not provide equal contributions to device function. For these reasons, we assessed device degradation in terms of Mg volume loss and corrosion product volume gain. We observed a net volume loss for all devices, with considerable corrosion product formation. Interestingly, we observed a greater corrosion rate for the plates than the screws (0.55 ± 0.02 and 0.40 ± 0.04 mm/year, respectively). We hypothesize that this difference is attributed to the devices' local environment. Unlike the screws, which were largely contained within bone, the plates were initially covered by muscle. This tissue has a higher water content and blood flow than bone, and therefore likely accelerated plate corrosion [42].

Interestingly, we also observed differences in corrosion behavior between screw regions. Specifically, our data suggest that corrosion was enhanced for screw heads compared to shafts. Similar observations of varied degradation behavior for Mg screws have been previously reported [27, 38, 41, 152]. For instance, Willbold et al implanted Mg alloy AZ31 screws into the hip bone of sheep. After three and six months, they observed accelerated corrosion of screw heads (surrounded by soft tissue) when compared to screw shafts (surrounded by bone) [41]. Uniquely, our screws were tested as part of a fixation system, and therefore screw heads were in contact with the overlying soft tissue, as well as the fixation plate. Shearing of these components, as well as compression during loading, likely contributed to corrosion within the head region [27,

153, 154]. A similar effect of compression on corrosion was shown by Denkena et al using LAE442 rods in vitro. They observed increased corrosion rate with compressive stress and decreased corrosion rate with tensile stress [155]. Despite these observations of accelerated corrosion, all devices remained in place and provided sufficient stabilization throughout the study. Furthermore, high levels of bone-device contact were observed, revealing osteointegration of the devices.

In the presence of ongoing device corrosion, fracture healing remained uninhibited, and cortical bone union matured throughout the study. These observations are in accordance with our previous study which demonstrated healing of similar rabbit ulnae fractures after 4 weeks. In the present study, we observed more mature healing after 8 weeks, which is consistent with the reported healing time of rabbit fractures [147]. These results demonstrate the ability of Mg fixation devices to facilitate physiological healing and long-term remodeling in a loaded fracture environment. Importantly, this reflects a unique advantage of Mg alloys over resorbable polymer devices, which are often not suitable for load bearing applications.

Uniquely, Mg devices have the potential to not only facilitate fracture healing, but also enhance bone formation. Several studies have highlighted this potential by showing increased mineral apposition, bone mass, and bone mineral density around Mg implants in bone [26, 30, 117, 144]. For instance, in a notable study by Witte et al, degradable Mg and polymeric implants were placed in the intramedullary space of guinea pig femora [26]. After 6 and 18 weeks, they observed a significant increase in mineralization for all groups with Mg implants when compared to polymeric controls. Similar results were observed with fast corroding Mg implants in rabbit femur [72]. These results highlighted the potential of degrading Mg implants to illicit a positive bone growth response, establishing their potential as strong candidates for orthopedic implants.

To our knowledge, however, there have been no reported investigations of Mg's ability to encourage bone formation in a traumatic fracture environment. In the present study, we observed abundant bone formation over and around all degrading Mg devices. This bone formation occurred over the devices, where periosteal and muscle tissue layers are typically present, suggesting the ability of Mg ion release from device degradation to affect osteoblastic cell differentiation. This observation is in accordance with our previous study in which de novo bone formation was observed around Mg plates and screws after 4 weeks [145], as well as a previous report of LAE442 screws and plates implanted in intact rabbit tibia [155]. With the present study, we have confirmed our pilot study observations, and demonstrated that prolonged exposure to Mg degradation can cause progressive bone formation. This bone formation is not typically seen with resorbable polymer or permanent metal devices, and therefore highlights a unique advantage of Mg fixation devices. In this manner, the degrading fixation device is gradually replaced by bone, without compromising fracture healing.

The mechanism of this bone growth is not yet fully understood, though some in vitro studies have been conducted to elucidate mechanisms of Mg's effect on bone cells [76]. We hypothesized that as these devices degrade, Mg is released, and local cells are stimulated to form bone (Figure 32). This effect has been demonstrated in vitro by exposing cells to Mg ion and assessing their osteogenic response [76, 156]. In addition, various in vivo models have also shown a beneficial effect of Mg degradation on bone [26, 30, 117, 144]. Considering the location of the newly formed bone observed in the present study, it is likely that the periosteum served as a cell source for osteogenic differentiation (Figure 32). Cells within this tissue layer, including osteoblasts and pluripotent mesenchymal stem cells, are known to facilitate bone growth and repair [8, 157]. It is possible that Mg released from our degrading devices stimulated stem cells

within the periosteum to initiate bone formation over the devices. This hypothesis is consistent with previous work by Bondarenko et al which demonstrated that fast corroding Mg implants enhanced expression of osteocalcin and osteopontin in surrounding bone tissue [158]. It is likely that the bone formation observed in the present study then continued as device degradation, and subsequent Mg release, persisted over time.

We hypothesize that this new bone contributes to the structural properties of the ulna, helps provide stabilization, and further facilitates weight-bearing activity during healing. Through three point bend testing, we observed a similar flexure load response of the healed ulnae when compared to healthy, un-fractured controls. Importantly, these results reveal that the structural properties of healed bone are similar to native ulnae, and that functional regeneration has occurred.

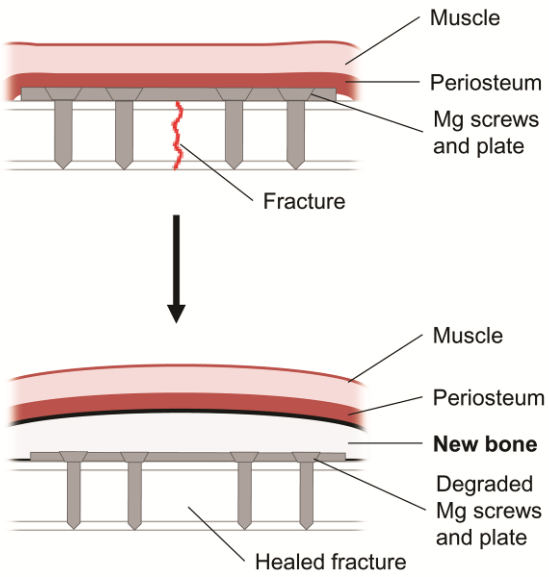

Figure 32. Schematic of proposed mechanism for Mg stimulated bone formation.

6.7 CONCLUSION

In the present study we assessed the efficacy of degradable Mg fixation plates and screws in a loaded rabbit ulna model. We have demonstrated that Mg device degradation does not inhibit fracture healing and enhances bone formation around the devices. Furthermore, we observed de novo bone formation above the devices, suggesting a role of Mg in cell differentiation and bone growth. To our knowledge, this is the first study to show the effect of Mg screws and plates on a loaded fracture model. These data support the potential use of pure Mg as fracture fixation devices.

7.0 IN VIVO ASSESSMENT OF MAGNESIUM ALLOY WXQK PLATE AND SCREW DEGRADATION AND BONE FRACTURE HEALING

7.1 ACKNOWLEDGEMENTS

The work presented in this chapter was supported by the NSF ERC RMB (grant 0812348), Commonwealth of Pennsylvania (SAP4100061184), University of Pittsburgh's Center for Craniofacial Regeneration, and the Edward R. Weidlein Chair Professorship funds of Prashant N. Kumta from the Swanson School of Engineering University of Pittsburgh, and is being prepared for publication. All work was done in collaboration with Da-Tren Chou, Daeho Hong, Dr. Sayuri Yoshizawa, Dr. Kostas Verdelis, Dr. Prashant N. Kumta, and Dr. Charles Sfeir. We would also like to thank Andrew Holmes (University of Pittsburgh) for device fabrication, Dr. Michael Epperly (University of Pittsburgh) for device sterilization, Dr. Alejandro Almarza (University of Pittsburgh) for assistance with mechanical testing, and the Pittsburgh Materials Technology, Inc. for assisting us in performing impact extrusion.

7.2 ABSTRACT

Previously, we reported positive results obtained with 99.9% Mg plates and screws as rabbit ulna fracture fixation devices ("In vivo study of Magnesium plate and screw degradation and bone

fracture healing"). Specifically, we observed gradual device degradation with no inhibition of fracture healing. In addition, we observed new bone formation around the degrading 99.9% Mg devices, with high levels of bone-device contact throughout. These results suggested a beneficial effect of Mg device degradation on local bone growth, which we postulated was an effect of the release of Mg ion into the surrounding tissue. For these reasons, we hypothesized that fixation devices made with a Mg alloy would perform similarly in vivo. To test this hypothesis, we developed and tested fixation plates and screws made with Mg alloy WXQK using the identical surgical procedure and assessment methods as previously used to test 99.9% Mg devices.

Interestingly, we observed several differences with the WXQK devices when compared to 99.9% Mg. For instance, we observed bone overgrowth around the WXQK devices with greater intracortical porosity than previously observed with 99.9% Mg. In addition, we observed cortical bone loss beneath WXQK devices, which had not been observed previously with pure Mg. These observations emphasize the biological sensitivity to Mg devices based on their corrosion rate and/or alloy composition, and underscore the importance of continued evaluations of these materials in vivo to better understand their corrosion behavior and subsequent biological response.

7.3 INTRODUCTION

Many recent studies have been conducted demonstrating the potential of Mg and its alloys as biomaterials for craniomaxillofacial and orthopedic applications. These studies have revealed biological responses to Mg, both in vitro and in vivo, which support bone regeneration and healing. For instance, several studies have demonstrated that degrading Mg implants elicit a local

increase in bone mineral density and mineral apposition [26, 27, 117, 144]. Furthermore, studies have shown an overgrowth of bone around Mg pins, plates, and screws in vivo [28, 109, 155]. Indeed, we have also observed new bone formation around 99.9% Mg plates and screws [86, 110]. In addition, we have conducted in vitro studies which begin to explore the mechanisms of Mg's effect on bone cells [76]. Taken together, we believe that degradable Mg alloys can serve as ideal fracture management devices by providing stabilization while actively supporting bone growth and healing. However, additional investigations are needed to fully understand the effects of degradation rate and alloy composition on the subsequent biological response. For these reasons, we are continuing to study Mg alloys as fixation plates and screws to better understand the alloy's effect on bone biology and healing.

In the present study, we evaluated Mg alloy Mg-1%Y-0.6%Ca-0.25%Ag-0.4%Zr (wt. %, denoted henceforth as WXQK with elemental abbreviations according to ASTM B275-05 [159]). This alloy was designed to exhibit good bulk workability for extrusion, and demonstrate higher stiffness compared to pure Mg. Herein, we describe our unique findings from evaluating WXQK as fixation plates and screws in a loaded rabbit ulna fracture model. Using this model, we have followed procedures previously described with 99.9% Mg devices [110], allowing us to contrast results obtained with the two Mg materials. We hypothesized that the WXQK alloy would perform similarly to 99.9% Mg in terms of bone healing and formation; however, we observed several differences in the biological response associated with the two materials. These findings provide important insight regarding Mg alloy performance in vivo, including possible caveats of the biological response dependent on alloy degradation rate and composition.

7.4 MATERIALS AND METHODS

7.4.1 WXQK alloy preparation

The WXQK alloy consisted of the nominal composition of Mg-1%Y-0.6%Ca-0.25%Ag-0.4%Zr in weight percent. Elemental ingots of Mg (US Magnesium Inc., Salt Lake City, UT, 99.97%), Y (Alfa-Aesar, Ward Hill, MA, 99.9%), Ca (Alfa-Aesar, 99.5%), and Ag (Alfa Aesar, 99.999%) were weighed according to the nominal composition, melted together in a graphite crucible using an induction furnace (MTI Corporation, Richmond, CA) purged with ultra-high purity (UHP) Ar, and vacuumed to avoid oxidation of the elements. The initial alloy produced by induction melting was cleaned thoroughly to remove residue and oxide scale, and was re-melted in a mild steel crucible using an electrical resistance furnace (Wenesco Inc., Chicago, IL) under the protection of Ar + 1.5% SF_6 cover gas. The melting and pouring temperature was 780 °C, and once the temperature was reached, Zr was added by adding Zirmax (Mg-33.3% Zr) master alloy (Magnesium Elektron Ltd., Manchester, UK). After Zr was added, the melt was stirred for 10 s at an interval of 1 min and 5 min to dissolve and disperse the Zr particles uniformly into the melt. The melt was held for 30 min and poured into a cylindrical mild steel mold preheated to 500 °C with dimensions of 44.5 mm diameter × 82.5 mm length. Appropriate holding and stirring times to release Zr particles from Zirmax master alloy is essential to achieve high solubility of Zr in the melt and optimal grain refinement [160]. The as-cast samples were solution treated (T4) at 525 °C for 6 h inside a tubular furnace covered under continuous UHP Ar flow and immediately quenched in water. The T4 treated alloy then underwent impact extrusion in which the alloy slug was cladded inside an aluminum can. The canned alloy was coated with a graphite-based lubricant (Neolube, Huron Industries, Port Huron, MI) and preheated for 1 h at 482°C. Following

pre-heating, the canned alloy was impact extruded through a die with an extrusion ratio of ~3. This WXQK extruded alloy was compared to as-drawn pure Mg (99.9%, Goodfellow Corp., Coraopolis, PA) in later reported tests.

7.4.2 WXQK phase characterization and microstructure analysis

In order to determine the phase formation, X-ray diffraction (XRD) was conducted using Philips X'Pert PRO diffractometer employing CuKα (λ=1.54056 Å) radiation with a Si-detector (X'celerator). The X-ray generator operated at 45 kV and 40 mA at a 2θ range of 10-80°. Peak identification was determined using the X'Pert High Score Plus software.

Microstructure of the WXQK alloy was analyzed by mounting the metal sample in epoxy which was then mechanically polished (Tegramin-20, Struers, Ballerup, Denmark) and chemically etched in a solution of 5 mL acetic acid, 6 g picric acid, 10 mL water, and 100 mL ethanol. The microstructure was observed using optical microscopy (Axiovert 40 MAT, Carl Zeiss, Jena, Germany and) and SEM (JEOL JSM-6610, JEOL Ltd., Tokyo, Japan) with EDX (EDAX Genesis, Mahwah, NJ) to conduct elemental analysis.

7.4.3 Mechanical testing

Tensile dogbone samples were machined along the long axis of the WXQK alloy as-cast ingot and WXQK and pure Mg extruded rods of with dimensions in accordance with ASTM-E8-04 with a gage area of 3 × 3 mm. Tensile tests were conducted at room temperature using an MTS testing system (MTS Systems Corporation, Eden Prairie, MN) with a crosshead speed of 1.3 mm/min. Tensile yield strength, ultimate tensile strength, Young's modulus (E), and percent

elongation were determined from the resultant stress-strain curves. The ultimate tensile strengths of the alloys were determined as the maximum tensile stress from the stress-strain curves. The tensile yield strengths were determined as the stress at the yield point during the tensile tests. Young's modulus was calculated as the slope of the linear elastic deformation region of the stress-strain curve. Percent elongation was determined from the strain at failure of the test samples. An average and standard deviation of at least 3 measurements was taken for each group.

7.4.4 Electrochemical corrosion testing

To assess the corrosion behavior of the WXQK alloy compared to pure Mg, the potentiodynamic polarization technique was used. Samples were connected to a copper wire using silver epoxy and mounted in epoxy resin. The mounted samples were mechanically polished, sonicated in isopropyl alcohol, and dried in air. The potentiodynamic corrosion study was carried out with an electrochemical workstation (CH-604A, CH Instruments, Inc., Austin, TX) at a scanning rate of 1 mV/s and potential window of 500 mV above and below the open circuit potential. A three electrode cell was employed with platinum as the counter electrode, Ag/AgCl as the reference electrode, and the sample as the working electrode. The test was performed in Dulbecco's Modified Eagle Medium (DMEM, with 4.5 g/l glucose, L-glutamine, and sodium pyruvate, Cellgro, Manassas, VA) supplemented with 10% fetal bovine serum (FBS), 100 U/ml penicillin, and 100 μg/ml streptomycin at pH 7.2 ± 0.2 and held at 37.4 °C. Before each measurement, the sample was immersed in the corrosion media to provide stability. The cathodic and anodic portions of the generated Tafel plots were fit linearly to allow calculation of corrosion potential (E_{corr}) and corrosion current density (i_{corr}).

7.4.5 Immersion corrosion testing

Corrosion of the WXQK extruded alloy and pure Mg were also measured using mass loss while immersed in a solution of 0.9% NaCl solution with volume to sample surface area ratio of 50 ml cm^{-2}. Immersion tests of samples polished to 1200 grit were carried at 37 °C. Samples were removed after 10 days of immersion and dried at room temperature. The sample masses were measured after samples were cleaned in a solution of 200 g/L of chromic acid and 10 g/L of $AgNO_3$ while sonicating for 1 minute to remove corrosion products. The corrosion rate was calculated according to ASTM G31-72 [34] with the following equation:

$$C = (K \times W)/(A \times T \times D) \quad (2)$$

Where C is the corrosion rate in mm $year^{-1}$ (mmpy), the constant K is 8.76×10^4, W is the mass loss in g, A is the sample area exposed to solution in cm^2, T is the time of exposure in h, and D is the density of the material in g cm^{-3}. An average and standard deviation of 3 measurements were taken for each group.

7.4.6 Device development

Device designs followed those previously used by our group (Figure 33, plates: 20x4.5x1-1.5 mm; screws: 7 mm long, 1.75 mm shaft outer diameter, 1 mm shaft inner diameter) [110]. Devices were cleaned with sonicated washes in acetone and ethanol, and sterilized with gamma radiation ($2x10^6$ cGy, 23.5 Gy/min, cesium 137 source, Mark I 68, JL Shepherd and Associates, San Fernando, CA).

Figure 33. MicroCT 3D reconstructions of WXQK devices before implantation.

7.4.7 Surgical procedure

All animal experiments were approved by the University of Pittsburgh's Institutional Animal Care and Use Committee following procedures, methods, and timelines previously described for 99.9% Mg [86]. A bilateral defect model was used with 12 New Zealand White rabbits (19 weeks old, 3.5±0.2 kg), providing 24 surgical sites (12 sites per time point). A 2 cm incision was made over the ulna, and overlying soft tissue was carefully retracted. An ulnar osteotomy (0.5-1 mm thick) was created using a hand held drill and then stabilized with one plate and four screws. Forearms were checked daily for signs of subcutaneous gas pocket formation. All observable gas pockets were documented and removed with a sterile syringe. Animals were then euthanized after 8 and 16 weeks.

7.4.8 MicroCT

To assess in vivo device degradation and new bone formation, devices were scanned before implantation and after euthanasia including the surrounding tissue. The devices as manufactured were scanned before implantation using a VivaCT40 (Scanco Medical AG, Bruttisellen, Switzerland) with a 10.5 μm voxel size, 55 kV tube potential, and 72 μA tube current. After 8

and 16 weeks of implantation, the device/local tissue complexes (n = 4 per time point) removed from the sacrificed animals were imaged using SkyScan1172 (Bruker-MicroCT, Kontich, Belgium) with a 10 μm voxel size, 79 kV tube potential, and 125 μA tube current. The CT images were digitally reoriented using SkyScan DataViewer. SkyScan CTAn software (version 1.13.5.1) was used to distinguish the remaining alloy and corrosion product from soft and hard tissue as previous described by segmenting based on absorption coefficient relative to mineral density [89, 146]. The alloy and corrosion product were discernable from each other due to a difference in their relative X-ray absorption coefficients. This was reflected by inflection points in the mineral density distribution histogram from which regions of interest could be captured by defining thresholds to delineate remaining alloy from corrosion products.

In addition to calculating the remaining volume of the plates and screws, corrosion rate was calculated from the volume of segmentations using the following equation:

$$CR = \Delta V/(At) \quad (3)$$

Where CR is corrosion rate in mm/yr, ΔV is change in Mg volume in mm^3, A is surface area in mm^2, and t is time in years [147]. The corrosion rates of the screws and plates were determined using the volume remaining in each respective regions of the device.

Local bone formation and resorption were also assessed by microCT. To quantify the amount of bone formed above the degrading devices, regions of interest were generated containing all bone located above the bottom of the plate. In addition, the intracortical porosity of this newly formed bone was quantified using CTAn software. Bone volume was also calculated within the cortical bone layer immediately beneath the plates (proximal layer). These cortical bone volumes were then compared to those found from our previous study assessing 99.9% Mg fixation devices [161].

7.4.9 Three point bend testing of in vivo implants

The relative strength of the ulnae after 16 weeks was assessed using three point bend testing as previously described (pre load: 1 N, loading speed: 5 mm/min, stop point: 0.5 mm flexural extension) [50, 86]. The flexural load at max extension was then recorded for each sample. Intact ulnae were used as controls.

7.4.10 Histological assessment

Samples were preserved with 10% formalin, embedded in Technovit 9100 New® (Heraeus Kulzer, Hanau, Germany), and sectioned at 5-10 μm thickness for histological assessments. Prior to staining, sections were deacrylated with xylene and 2-methoxyethyl acetate (MEA) for 20 min each, followed by gradual rehydration to deionized water. Masson-Goldner Trichrome stain was performed according to the manufacturer's protocol (Electron Microscopy Sciences, Hatfield, PA). In addition, sections were stained with Toluidine Blue working solution for 2 min, rinsed in water, gradually dehydrated, and mounted for bright field imaging. Osteoclasts were identified using tartrate-resistant acid phosphatase (TRAP) staining according to manufacturer's protocol (Sigma-Aldrich, St. Louis, MO). Sections were stained with the TRAP working solution for 1 hour at 37 ºC, rinsed in water, and mounted for bright field imaging.

7.4.11 Statistical analysis

Statistical analysis was performed using IBM SPSS Statistics 19 (IBM, Armonk, NY). To determine statistical differences between groups for mechanical tests, one-way ANOVA

followed by Tukey's test was used. For immersion corrosion and in vivo tests, groups were compared using a student's t-test. Device degradation was compared between 0 and 8 weeks (n=4 screws, n=2 plates per time point). Cortical bone loss and periosteal bone growth quantifications were compared across time points of 8 and 16 weeks (n=4 per group). Flexural load response to three point bending was also compared across time points of 8 and 16 weeks (n= 6 per time point). Graphical representations reflect mean ± standard deviation.

7.5 RESULTS

7.5.1 WXQK phase and microstructure characterization

The phases of the as-cast and extruded WXQK alloys were characterized by X-ray diffraction as shown in Figure 34. The XRD spectra show both conditions of the alloy were composed of hcp α-Mg, without detecting the presence of unalloyed Y, Ca, Ag, Zr, or intermetallic phases. The microstructure of the extruded alloy is shown in the optical micrographs of Figure 35, demonstrating significant grain size reduction after impact extrusion of the as-cast alloy.

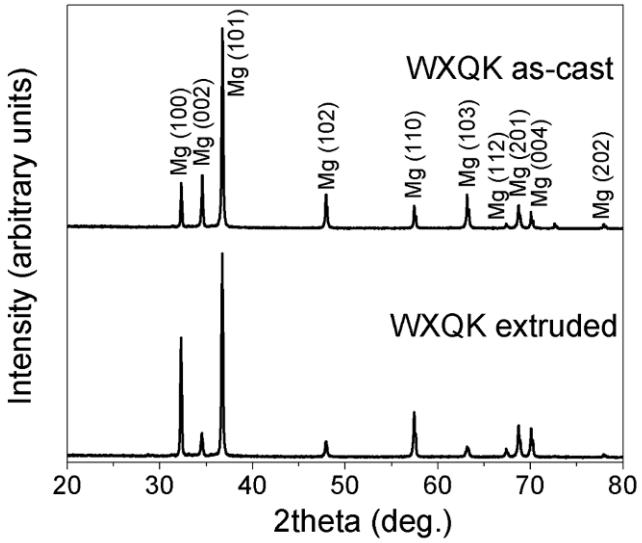

Figure 34. X-ray diffraction pattern of WXQK in as-cast and extruded forms.

Peaks of α-Mg are indicated throughout.

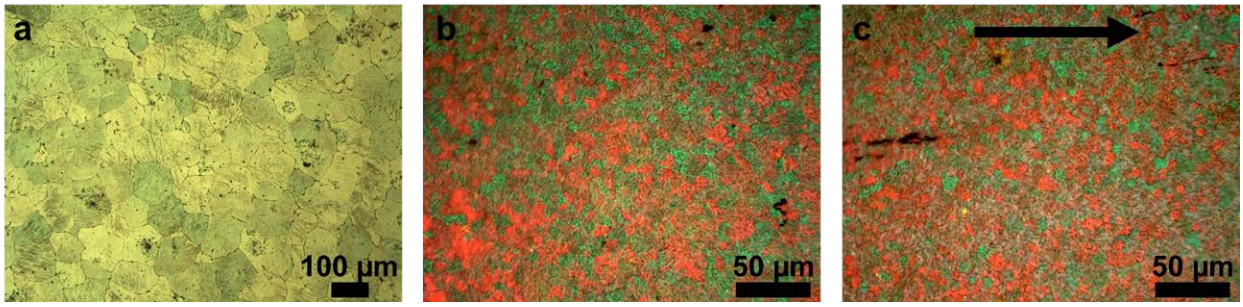

Figure 35. Optical micrographs showing WXQK microstructure.

Conditions shown include as-cast (a), and after impact extrusion with sections taken in the transverse (b) and longitudinal (c) planes to the direction of extrusion (arrow indicates direction of extrusion).

SEM and EDX (Figure 36) revealed that the WXQK as-cast and extruded alloys included clusters of secondary phase intermetallics which formed by segregation during solidification. These particles consisted of the alloying elements Ca, Ag, with elevated amounts of Y, as well as impurities of Al and Si (Figure 36 d-e). The bulk grains alloy matrix included Mg, O, and dissolved Ca (Figure 36 d region 1, e region 4). Regions at the grain boundaries (Figure 36 d

point 3, e point 6) also contained impurity elements of Si and Al, as well as small amounts of alloying elements Ca and Ag. After extrusion, while the bright segregations of secondary phase intermetallics became aligned in the direction of extrusion as seen in Figure 36 c and f, they remained at a relatively similar volume compared to the as-cast material, despite being subjected to a T4 solution treatment and extrusion.

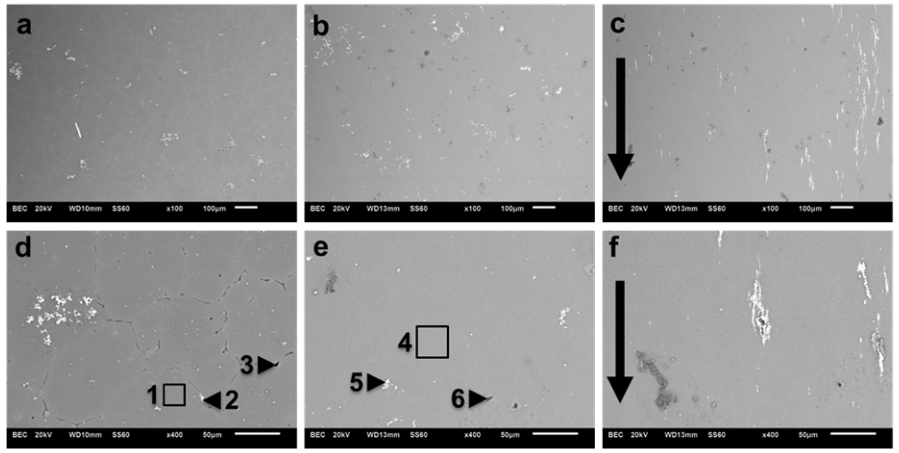

	Element	Wt. %
1	O	3.60
	Mg	96.17
	Ca	0.22
2	O	9.20
	Mg	52.54
	Ca	5.61
	Y	32.18
3	O	10.76
	Mg	73.02
	Si	14.91
	Ca	1.07
	Ag	0.25

	Element	Wt. %
4	O	6.73
	Mg	92.67
	Al	0.16
	Ca	0.43
5	O	14.95
	Mg	44.02
	Al	0.68
	Si	0.77
	Ca	1.98
	Y	37.61
6	O	5.49
	Mg	93.80
	Al	0.20
	Ca	0.51

Figure 36. SEM images showing WXQK microstructure.

Microstructure shown at 100x (a-c) and 400x (d-f) magnification: WXQK as-cast (a, d), WXQK extruded transverse section (b, e), and WXQK extruded longitudinal section (c, f). Elemental composition as determined by EDX in selected regions. In c and f, arrow indicates direction of extrusion.

7.5.2 WXQK mechanical properties

Mechanical properties were determined using tensile testing of dogbone shaped samples of the Mg alloys. The tensile mechanical properties of the WXQK alloys and pure Mg are presented in Table 2. After extrusion, both yield and ultimate tensile strength and strain at failure increased significantly for the WXQK alloy. Yield strength was also significantly higher compared to pure Mg; however the ultimate tensile strength was similar. Pure Mg possessed a higher elongation than the WXQK alloy.

Table 2. Tensile mechanical properties of WXQK and pure Mg.

Yield tensile strength between groups was significantly different (* p<0.001). Ultimate tensile strength between WXQK as-cast and other groups was significantly different († p<0.001). Strain at break between WXQK as-cast and Pure Mg was significantly different (§ p=0.007).

	Yield Tensile Strength (MPa)*	Ultimate Tensile Strength (MPa) †	Strain At Break (%) §	Modulus (GPa)
WXQK as-cast	65.6 ± 2.7	130.0 ± 28.0	4.4 ± 2.7	51.0 ± 8.0
WXQK extruded	185.5 ± 3.5	217.0 ± 11.3	6.1 ± 5.4	48.7 ± 1.3
Pure Mg	128.9 ± 14.1	221.6 ± 4.6	13.1 ± 3.1	45.2 ± 16.2

7.5.3 WXQK corrosion properties (in vitro)

The corrosion rates of the as-cast and extruded WXQK alloys were calculated based on mass loss after immersion in 0.9% NaCl solution and by electrochemical corrosion measurements. Representative potentiodynamic polarization curves (Figure 37) show the similarities between the WXQK alloy's Tafel plots, whereas pure Mg is clearly shifted to lower corrosion current densities. Thus, the corrosion rate of pure Mg was calculated to be lower than that of the alloys tested (Table 3). The lower corrosion rate of pure Mg compared to the WXQK alloy held true after conducting immersion corrosion in 0.9% NaCl solution (Figure 38).

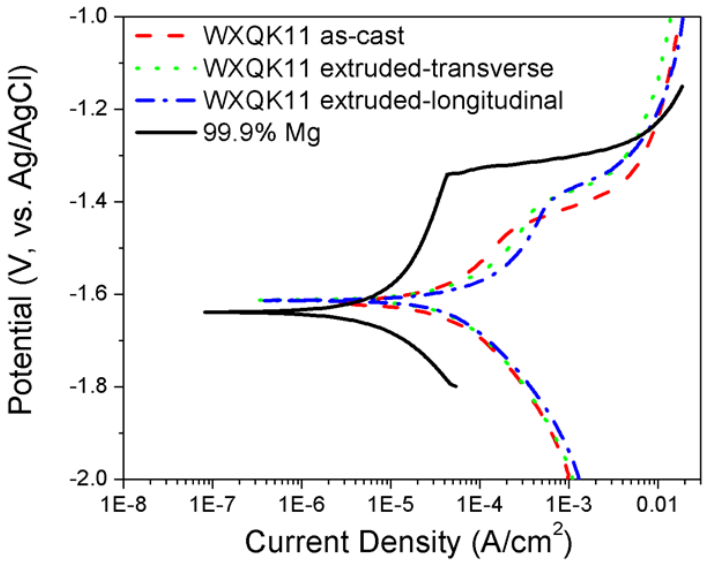

Figure 37. Representative potentiodynamic polarization curves of WXQK.

As-cast and extruded alloys with transverse and longitudinal sections exposed are shown compared to pure Mg conducted in DMEM at 37 °C.

Table 3. Electrochemical conducted in DMEM with 10% FBS at 37 °C of WXQK and pure Mg.

Material	Corrosion potential, E_{corr} (V)	Corrosion current density, i_{corr} (μA cm^{-2})	Corrosion rate, mm/year (mmpy)
WXQK as-cast	-1.62	84.22	1.93
WXQK extruded-transverse section	-1.61	64.26	1.48
WXQK extruded-longitudinal section	-1.61	61.71	1.42
Pure Mg	-1.64	7.65	0.17

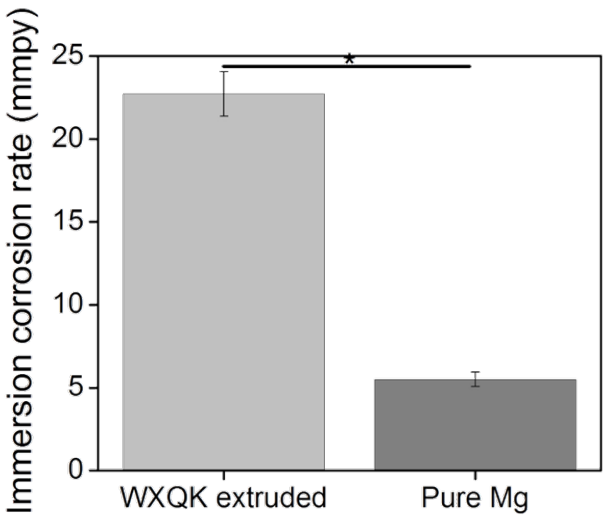

Figure 38. Immersion corrosion rates of WXQK extruded alloy and pure Mg.

Degradation rate between groups was significantly different (* p=0.001) in 0.9% NaCl solution at 37 °C.

7.5.4 In vivo device degradation

Evidence of in vivo device degradation was initially observed through subcutaneous gas pocket formation (Supplemental Figure 2). Gas pockets were observed through 6 weeks in 50% of all animals. Some animals developed multiple gas pockets, while others developed only one or no gas pockets. The largest number of total gas pockets observed in a single week was 6, and no gas pockets were observed after 6 weeks.

Screw degradation after 8 weeks was quantified by 3D microCT (Figure 39). After 8 weeks, we observed a significant reduction in underlying alloy volume (p=0.002) accompanied by the formation of corrosion product at the device periphery. Based on alloy volume change, the corrosion rates at 8 weeks were calculated to be 0.45 ± 0.04 mm/year for screws (n=4) and 0.71 ± 0.02 mm/year for plates (n=2). Device degradation after 16 weeks was also assessed with

microCT; however due to excessive corrosion and tissue infiltration, volume loss quantifications were not performed.

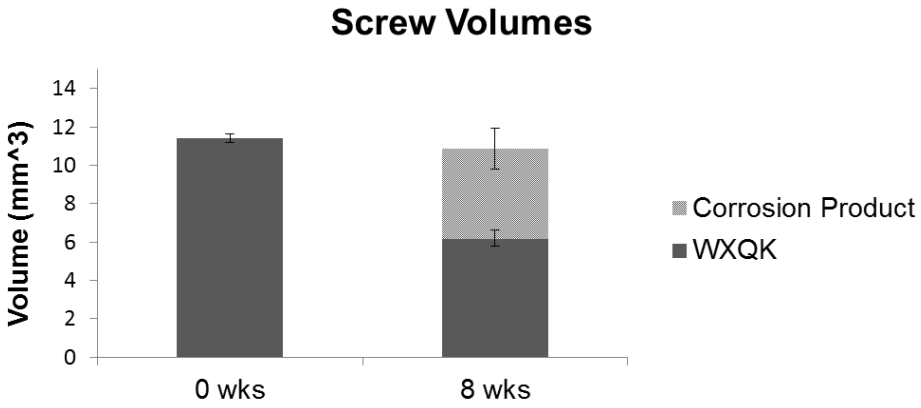

Figure 39. MicroCT quantification of screw degradation.

Volumes of remaining WXQK and corrosion product were quantified separately as shown. WXQK volume was significantly reduced from 0 to 8 weeks (* p=0.002), while corrosion product was formed. Using these alloy volumes, corrosion rates were determined to be 0.45 ± 0.04 mm/year for the screws (n=4) and 0.71 ± 0.02 mm/year for the plates (n=2, not shown) from 0 to 8 weeks.

7.5.5 Bone overgrowth

Bone overgrowth was studied using microCT and histology (Figure 40). Progressive periosteal bone formation was observed above the degrading devices throughout the course of the study. By 8 weeks, 36.61 ± 26.28 mm^3 of new bone was formed over the devices, providing partial coverage (Figure 40 A, Figure 41 A). By 16 weeks, this bone growth increased significantly ($p=0.014$) to 175.78 ± 62.02 mm^3, completely encasing the devices (Figure 40 B, Figure 41 B). Histological staining with Masson-Goldner Trichrome showed normal bone morphology within this region, including osteocytes and osteoid (Figure 40 C&D). Interestingly however, this newly formed bone appeared highly porous. When compared to bone overgrowth observed in a

previous study by our group using 99.9% Mg fixation devices [110], the average pore volume at 16 weeks was significantly larger (p=0.041) with WXQK devices (Figure 41 B). The difference in porosity can be observed by comparing Figure 40 with Supplemental Figure 3.

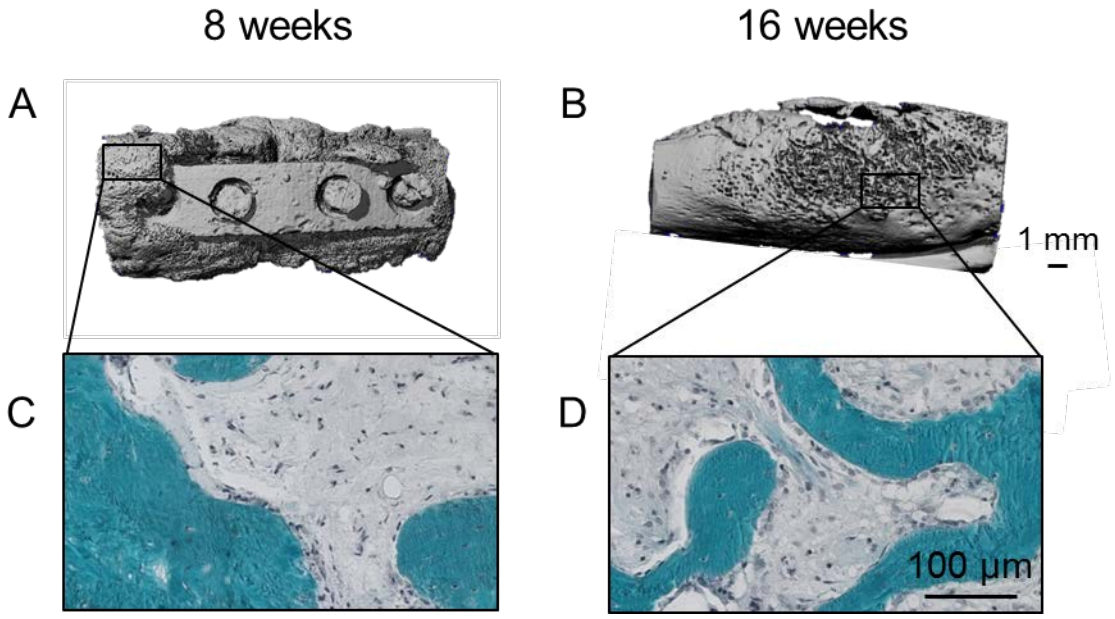

Figure 40. MicroCT and histological staining showing bone overgrowth around WXQK devices. 3D reconstructions show partial bone overgrowth after 8 weeks (A) and full overgrowth by 16 weeks (B). Newly formed bone appeared highly porous, unlike previous observations of smoother and more compact bone overgrowth around 99.9% Mg devices (Supplemental Figure 3, [110]). Masson-Goldner Trichrome staining showed osteocytes and osteoid within these regions at 8 and 16 weeks (C and D, respectively).

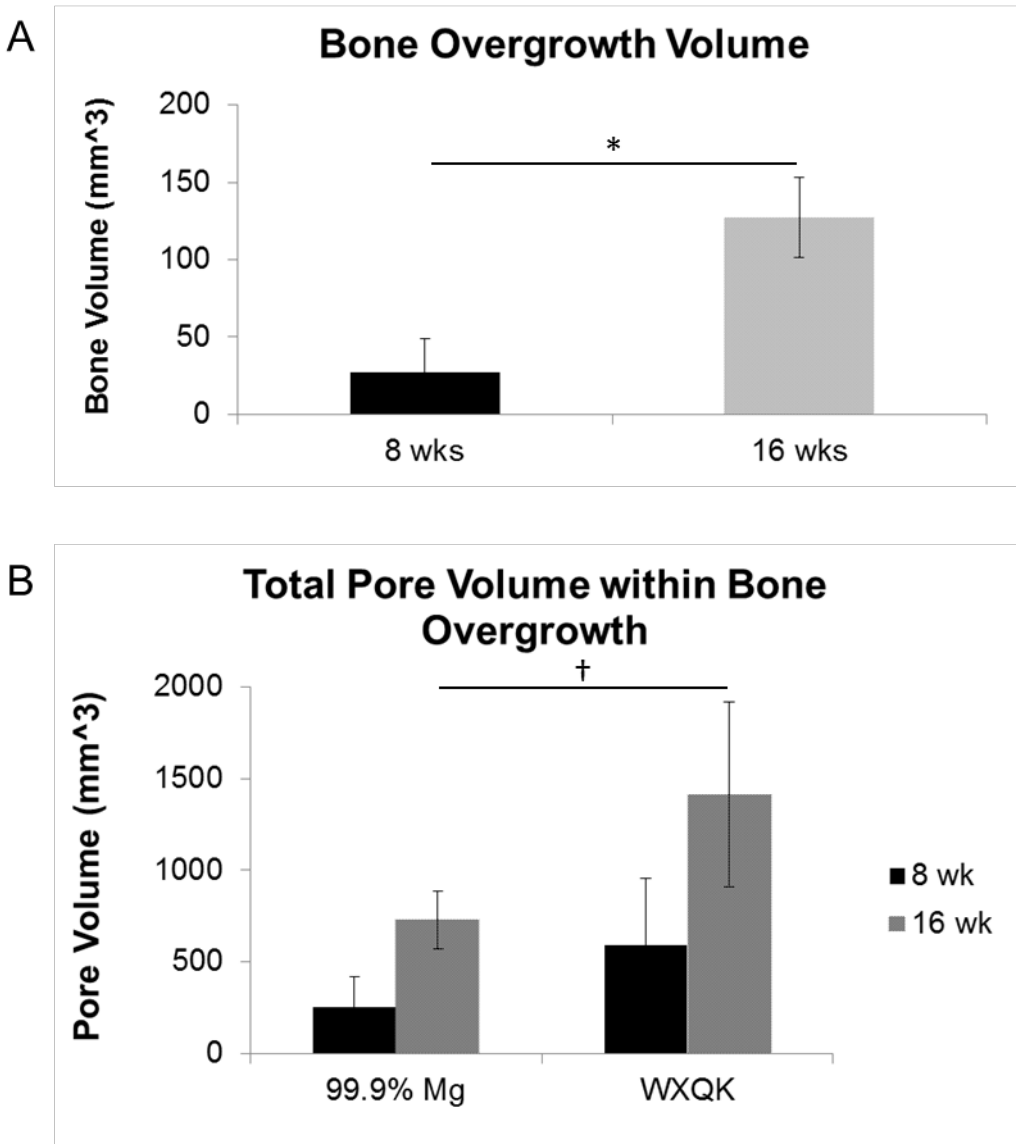

Figure 41. MicroCT quantification of bone overgrowth and intracortical porosity.

By 8 weeks, 36.61 ± 26.28 mm3 of new bone was formed over WXQK devices. This new bone growth increased to 175.78 ± 62.02 mm3 by 16 weeks (A, * p=0.014). Total pore volume within the bone overgrowth was also quantified using microCT and compared to previously studied 99.9% Mg ([110], n=4 per time point). Increased pore volume was found for WXQK compared to 99.9% Mg (B, † p=0.041) at 16 weeks.

7.5.6 Cortical bone resorption

Cortical bone loss was observed by microCT and histology (Figure 42). This bone loss affected the cortical bone layer immediately beneath the plates (referred to hereafter as the proximal layer) and did not affect the more distant cortical bone layer (referred to hereafter as the distal layer). When compared to cortical bone volumes observed previously in a separate study by our group using 99.9% Mg fixation devices [110], the average cortical bone volume beneath WXQK devices was significantly reduced at 8 ($p=0.003$) and 16 ($p=0.004$) weeks (Figure 42 G). TRAP staining revealed no differences in the presence of osteoclasts throughout the samples (Supplemental Figure 4). Osteoclasts were observed in newly formed bone above the devices, as well as within the proximal and distal layers of cortical bone.

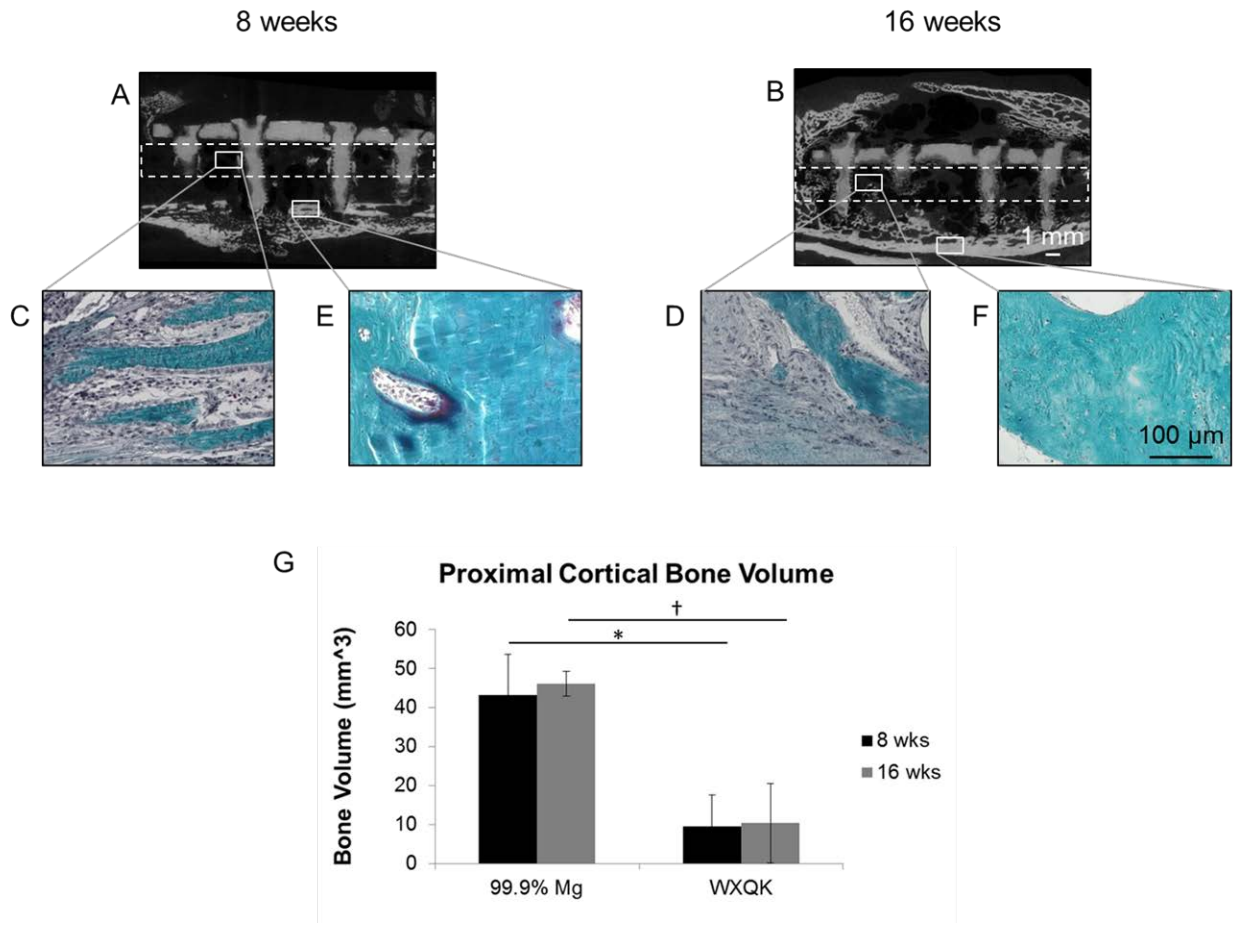

Figure 42. MicroCT and histological staining showing bone healing with WXQK devices. Cortical bone loss was observed beneath the plates after 8 (A) and 16 weeks (B). White dotted boxes outline areas originally containing the cortical bone layer. The volume of remaining proximal cortical bone was quantified and compared to previously studied 99.9% Mg [110]. Significantly less bone remained after 8 (* p=0.003) and 16 († p=0.004) weeks for animals with WXQK devices compared to 99.9% Mg devices (E). Despite this bone loss, distal cortical bone healing was observed in 77% of samples after 8 weeks (C) and 88% of samples after 16 weeks (D). Histological staining of this healed bone showed healthy bone morphology (C and D).

7.5.7 Fracture healing

Despite proximal cortical bone loss beneath the plates, distal cortical bone healing was observed in 77% of samples after 8 weeks and 88% of samples after 16 weeks through microCT and histology. Healed bone within these regions appeared histologically normal through Masson-Goldner Trichrome staining (Figure 42 E&F).

7.5.8 Bend testing

The relative flexural load response of healed ulnae was assessed using three point bend testing. After 16 weeks, we observed no difference in flexure load response for healed ulnae when compared to healthy, age-matched controls (Figure 43).

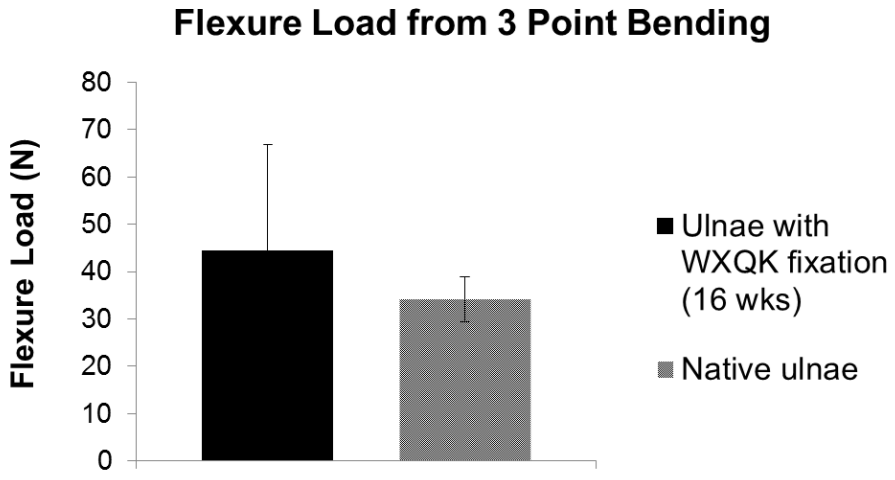

Figure 43. Three point bend testing results.

Three point bend testing was performed to evaluate the flexure load response of healed ulna after 16 weeks. No significant difference was found in the flexure load of healed ulnae and healthy un-fractured control ulna after 16 weeks.

7.6 DISCUSSION

To reduce the risk of long term complications and eliminate the need for implant retrieval surgeries, we are exploring degradable Mg alloys for bone fixation applications. In the current study, a high stiffness, as-extruded, biodegradable Mg alloy was tested using a rabbit ulna fracture model previously employed by our group [110]. Alloy extrusion is widely used to achieve grain refinement. This process has a profound effect on material strength through the Hall-Petch relation in which grain boundaries act as pinning points to impede the propagation of dislocations [162, 163]. In the present study, WXQK alloy extrusion resulted in a significant improvement in material strength compared to as-cast WXQK alloy due to the decreased grain size. These results are in accordance with previous work showing that as-cast Mg-Y-Ca-Zr retained more refined grains than after solution treatment, resulting in higher mechanical properties [70]. We observed that the as-extruded Mg-Y-Ag-Ca-Zr exhibited higher yield strength compared to extruded pure Mg, whereas ultimate tensile strength of both materials were similar (Table 2). The elemental composition of the WXQK alloy provided theoretical advantages over pure Mg. For instance, Y and Ca contribute to grain boundary strengthening of Mg alloys [164] and improve corrosion resistance [39, 165, 166]. Zr serves as an effective grain refining agent [167], imparting grain boundary strengthening [168] and corrosion resistance [169]. Finally, the addition of 0.6 wt. % Ag increases ductility and bulk workability of the alloy for extrusion. Furthermore, Mg-Ag alloys have demonstrated antibacterial properties, reducing the viability of Staphylococcus aureus and Staphylococcus epidermidis [170].

Although as-extruded Mg-Y-Ag-Ca-Zr was designed to exhibit corrosion resistance comparable to pure Mg, the corrosion rate of Mg-Y-Ag-Ca-Zr was significantly higher than that of pure Mg in immersion corrosion measurements conducted in 0.9% NaCl solution at 37 °C

(Figure 38). It is possible that the addition of Ag resulted in the observed accelerated corrosion. Similar observations have been made with as-cast Mg-Ag alloys in which increasing Ag content resulted in more rapid corrosion [170]. In addition, corrosion may have been accelerated due to the presence of segregations of alloying elements such as Y (Figure 36), making the beta phase more cathodic when the passive layer is not stable [171].

Despite these observations of accelerated corrosion in vitro, we identified the as-extruded WXQK alloy to be a good candidate material to test as fixation plates and screws in vivo due to its high yield strength. Previously, we reported encouraging results with 99.9% Mg plates and screws for rabbit ulna fracture fixation [86, 110]. In these previous studies, we observed healthy bone regeneration in the presence of device degradation, as well as new bone formation around the devices. Based on those results, we hypothesized that Mg ion release from degrading Mg devices has the ability to influence periosteal stem cells and ultimately enhance bone formation. In the present study, we aimed to further explore this phenomenon using the WXQK alloy.

Interestingly, our results obtained with WXQK devices varied from our prior work with 99.9% Mg. For instance, in the present study we observed cortical bone resorption beneath the plates after 8 and 16 weeks, which has not been observed with 99.9% Mg. Similar observations have been reported with other metallic and polymeric plating systems and are typically attributed to surgical trauma, stress shielding, and inhibited local blood supply [172-176]. In the present study however, we believe it is unlikely that these factors contributed to the observed bone loss. The surgical technique used in this study was previously performed by our laboratory without complications, making it unlikely that the induced trauma would cause bone resorption. Furthermore, the devices used in this study were degradable, gradually decreasing their load-bearing contribution over time. We anticipate that as these devices degrade, their load is

transferred onto the ulnae, thus limiting stress shielding [177, 178]. In addition, device degradation would likely reduce compression on surrounding bone, minimizing damage to the local vasculature.

For these reasons, we believe that our observations of bone resorption are a result of WXQK alloy degradation. This degradation could affect surrounding tissue through alloying element release and/or gas release. By weight percent, the most predominant component of the WXQK devices is Mg. Various in vitro and in vivo studies have demonstrated Mg's biocompatibility and positive effect on osteoblasts and mineralization [26, 28, 40, 86]. In addition, recent studies have begun to elucidate effects of Mg on osteoclasts [116, 179]. For instance, Wu et al used $MgCl_2$ and 99.95% Mg extracts to study effects of Mg on human osteoclastogenesis and osteoclast activity in vitro [116]. Using serial dilutions of the Mg extracts, they mimicked the theoretical Mg gradient surrounding degrading Mg alloys. Their data showed that when exposed to increasing Mg concentrations, cellular metabolic activity and differentiation were reduced, while resorption activity per osteoclast was increased. In the present study, we also assessed osteoclast presence using TRAP staining; however, we observed no differences in osteoclasts based on proximity to our degrading implants. Osteoclasts were observed sporadically throughout remodeling bone above the devices and within cortical bone beneath the devices. Although the bone loss observed in this study was likely caused by osteoclastic activity, it is possible that our time points for histological assessments (8 and 16 weeks post-op) were too late to observe differences in osteoclasts presence. If we consider gas release as a marker of alloy degradation, we would expect the most significant Mg release to occur within 2-6 weeks post-op. During this time, the concentration of Mg around the devices would increase, potentially affecting osteoclast behavior [116]. However, after 8 weeks,

corrosion product formation on the device surfaces may have slowed degradation and subsequent Mg release, thereby allowing local Mg concentrations to equilibrate.

In contrast to resorption of the underlying cortical bone, we observed new bone formation on top of the devices. Similar bone growth has previously been reported by our group [86, 110] as well as others [26, 28]. Interestingly however, in the present study we observed large intracortical pores throughout this bone. It is possible that these pores are the result of rapid gas release from accelerated device degradation. Based on our experience with this surgical model, bone overgrowth around degrading Mg devices begins before 4 weeks post-op [86, 110]. Concomitantly, the plates and screws release gas as they degrade. Similar gas release has been observed by other groups in soft tissue and bone marrow adjacent to degrading Mg devices. Over time however, this gas was shown to dissipate [26, 28, 39, 180-182]. In the current study, we speculate that the rapidly released gas became trapped within the overlying bone during mineralization, giving rise to the large pores we observed. Additional long term studies are needed to better understand how this morphology will change over time as the bone remodels [172].

The dichotomy in our observations of bone resorption beneath devices and bone growth above devices highlights site-specific biological responses to Mg alloy degradation. Indeed the environments above and below the devices are quite different and contain unique cell populations. It is possible that alloy degradation and subsequent ion release elicited unique responses from the undifferentiated MSCs within the periosteum (above devices) and the differentiated cells of the cortical bone (below devices). Recent work by Yoshizawa et al explored effects of $MgSO_4$ on undifferentiated hBMSCs and differentiated osteogenic cells in vitro [76]. They observed that 10 mM $MgSO_4$ enhanced COL10A1 and VEGF expression;

however, they saw an activation of HIF-2α for undifferentiated hBMSCs and PGC-1α for differentiated osteogenic cells. These data revealed that the effect of Mg ion on cell behavior can vary depending on cell differentiation; however additional investigations are needed to better understand these cellular responses.

In addition to cellular differences, the tissues surrounding the devices maintain different vascularity. For instance, the environment above the devices initially consisted of periosteum and muscle. Compared to the cortical bone beneath the devices, these tissues are more vascularized and capable of providing enhanced buffering of pH and alloying elements released through device degradation. It is possible that insufficient buffering capacity, coupled with the increased WXQK corrosion rate, caused a local pH increase and subsequent bone resorption beneath the devices. A difference in the Mg concentration in these two regions may also result in the varying bone response, indicating a threshold of local Mg beyond which may elicit mineralization defects [183] and inhibitory effects on osteoblast differentiation and mineralizing activity [184]. The addition of Ag may also have had an effect on bone growth surrounding the device, as higher concentrations of Ag treatment have been found to inhibit the osteoinductive capability of demineralized bone matrix [185]. Ag nanoparticles also exert dose-dependent cytotoxic effects on osteoblast and osteoclast differentiation and viability, and may have negative effects on the osseointegration of orthopedic implants [186]. Similarly, Y has been shown to have concentration-dependent effects on osteoblast proliferation, differentiation, and mineralization function [187]. These dose-dependent relationships between alloying elements and the resultant bone response generally indicate that higher concentrations of elements result in detrimental effects on bone growth, and suggest a controlled alloy degradation profile is preferred. Due to the rapid degradation of the WXQK alloy used in this study, bone resorption may have occurred

in areas where the concentration of the degradation products reached the threshold to cause detrimental effects.

Despite these concerns of the effects of the elements used in the WXQK alloy, several of the components (Mg, Y, Zr) are included in other commercial alloys such as WE43 (Y 4%, Nd 2.25%, 0.15% Zr) and have been studied in vitro and in vivo, demonstrating good biocompatibility [188, 189]. Y and Zr are also included in the MAGNEZIX® compression screw for small bone fractures which has obtained CE marking of medical devices for medical applications in Europe after a randomized, controlled clinical study was conducted using the Mg alloy screw in hallux valgus surgery, demonstrating the safety of the alloying elements in this embodiment [190]. Additional work is needed to fully assess the potential toxicity of the WXQK alloy used in the current study; however, we observed no signs of systemic toxicity via behavioral changes in the animals. Animals resumed normal behavior and weight-bearing movement following surgery. Furthermore, despite the observed cortical bone loss, mechanical testing demonstrated no significant difference in the flexure load response of ulnae fixed with WXQK devices when compared to healthy, intact controls after 16 weeks.

7.7 CONCLUSIONS

In this study, we assessed as-extruded WXQK plates and screws as degradable fixation devices. We observed in vitro improvements in mechanical strength, however in vitro and in vivo corrosion was accelerated when compared to previously studied pure Mg. Unlike observations from our previous work with pure Mg, we observed a contrast in the biological effect of WXQK degradation above and below the devices. In the present study, we observed highly porous bone

growth above the devices and cortical bone loss beneath the devices. These observations highlight the importance of controlled device degradation. We speculate that accelerated corrosion and insufficient buffering can result in gas and ion accumulation, ultimately leading to compromised bone formation or bone loss. Additional studies should be conducted to better understand the effects of alloying elements on bone cells. Through an improved understanding of these effects, we may better identify optimal degradation profiles and associated concentration ranges of alloying elements to promote bone healing and avoid detrimental bone loss.

8.0 CONCLUSIONS

In the present dissertation, degradable Mg alloys were studied for their potential as bone fixation devices. We hypothesized that their unique combination of in vivo degradation and mechanical strength would allow them to serve as ideal materials for orthopedic fixation devices by providing fracture stabilization to facilitate healing while undergoing gradual degradation.

To study these materials, we utilized multiple in vivo models which can provide more clinically relevant results than in vitro testing alone. First, we developed and assessed two unique models for material testing in rodents subcutaneously. Our original model consisted of a Mg alloy rod contained within a collagen scaffold seeded with hBMSCs (Figure 5). Using this model, we obtained qualitative and quantitative results describing alloy degradation and subsequent biological effect. Using microCT, we measured an increase in the degradation of 99.9% Mg compared to Mg alloy AZ31 after 8 weeks (Figure 6). Furthermore, histological staining, IHC, and in situ hybridization showed a normal inflammatory response with mouse and human cells around the degrading Mg implants (Figure 7). In addition, we observed expression of osteogenic proteins DMP1 (Figure 9) and OPN (Figure 10) in samples which contained hBMSCs. Alternatively, expression of these proteins was not observed in samples without hBMSCs, suggesting an active role of hBMSCs in the observed protein expression.

These results demonstrated the utility of our model to study effects of Mg degradation on a clinically relevant human cell population in vivo. However, we hypothesized that this model

could be further refined by replacing the collagen scaffolds with scaffoldless constructs. Scaffoldless constructs were formed directly from hBMSCs and wrapped around Mg alloys, providing a biomimetic cellular matrix environment (Figure 11). Using this model, we assessed the corrosion behavior of 99.9% Mg, as well as its effect on surrounding mouse and human cells. MicroCT showed gradual Mg degradation with corrosion product formation on the implant surface (Figure 12). Volume change quantifications revealed that the corrosion rate of the Mg implants decreased over time, likely a result of surface passivation (Figure 13). More detailed assessments of the corrosion layer using histological staining as well as SEM and EDX identified Mg, Ca, and P within this region (Figure 14, Figure 15, Figure 16). In the presence of ongoing Mg degradation, both mouse and human cells were observed within adjacent tissue. Interestingly, we observed expression of OC (Figure 18) and OPN (Figure 19) around the Mg implants in all samples, including those without hBMSCs. In contrast with our previous results obtained from the scaffold-based study, these observations suggest that the degrading Mg and/or corrosion product can trigger osteogenic differentiation of native mouse cells without hBMSCs. Taken together, these studies highlight the importance of the cellular microenvironment on cell behavior and shed light on the potential role of the corrosion layer in the biological response to degrading Mg implants.

In addition to studying Mg alloys as basic materials, we have developed and assessed them as functional fixation plates and screws in vivo. These devices were first tested through a pilot study in which we compared devices made with 99.9% Mg to clinically-used Ti (Figure 20). Through this study, we observed that the Mg devices performed similar to the Ti devices by providing fracture reduction and alignment to facilitate physiological bone healing (Figure 23). Interestingly however, we observed an abundance of newly formed bone around the degrading

Mg, but not Ti, devices after 4 weeks (Figure 24). This striking observation suggested that Mg device degradation could increase local bone formation; however, additional assessments were needed to verify these observations.

For these reasons, we conducted a follow-up studies in which we developed and tested fixation plates and screws made from 99.9% Mg (Figure 25) and Mg alloy WXQK (Figure 33). In these studies, we conducted detailed assessments of device degradation and bone regeneration after 8 and 16 weeks. The results obtained with 99.9% Mg devices were extremely positive. We observed gradual device degradation (Figure 26), physiologically normal fracture healing (Figure 28), and integration of the degrading devices with surrounding bone (Figure 29). Furthermore, we observed substantial new bone formation around all devices (Figure 30). These data verified our pilot study observations and demonstrated the preliminary efficacy of 99.9% Mg fixation devices in vivo.

We hypothesized that the beneficial effects of device degradation were related to Mg ion release, and therefore expected the WXQK alloy to perform similarly to 99.9% Mg in vivo. However, we observed several differences in the biological response to WXQK devices when compared to 99.9% Mg. For instance, we observed substantial bone overgrowth around WXQK devices (Figure 40); however, this bone was highly porous with an irregular morphology (Figure 41). Furthermore, we observed cortical bone loss beneath most WXQK plates after 8 and 16 weeks (Figure 42). These observations revealed an adverse reaction of local cells and tissue to WXQK degradation. We speculate that this adverse reaction was linked to the accelerated device degradation through excessive release of Mg ion, alloying elements, and/or gas. However, additional investigations, such as detailed mechanistic studies, are needed to clearly identify

which degradation effects are responsible for the observed bone loss and changes in newly formed bone morphology.

Despite our variable observations with WXQK, our overall work with degradable Mg alloys has demonstrated potential for these materials to be used for bone fixation and regeneration applications. By undergoing controlled in vivo degradation, pure Mg devices could reduce the risk of long term complications and eliminate the need for removal surgeries. Furthermore, when properly controlled, the degradation of pure Mg can enhance local bone formation to facilitate osteointegration, support fracture healing, and potentially improve clinical outcomes.

9.0 FUTURE DIRECTIONS

In order to exploit the advantageous traits of Mg degradation, such as enhanced local bone formation, additional work should be done to understand the mechanisms of these effects. For instance, the effect of Mg degradation on differentiated versus undifferentiated cells should be explored. These investigations have been initiated by Yoshizawa et al, who revealed a variable effect of Mg on hBMSCs depending on their stage of differentiation [76]. Their work showed enhanced mineralization, VEGF, and ColX expression when hBMSCs were exposed to 10 mM $MgSO_4$. Interestingly, they observed that for undifferentiated hBMSCs, this enhancement was linked to activation of the HIF signaling pathway. Alternatively, for differentiated hBMSCs, the PGC-1a pathway was activated. This work demonstrated that Mg's effect on cells may be specific to their stage of differentiation; however, additional work is needed to fully understand these mechanisms both in vitro and in vivo.

By understanding the mechanisms of Mg's biological effects, we may tailor device design to maximize bone regeneration, while avoiding bone resorption or other adverse reactions. For instance, Mg devices could be designed to meet specific degradation profiles, such as initial burst degradation (and Mg^{2+} release) followed by slower degradation (and sustained Mg^{2+} release). In addition, Mg devices could be designed for specific applications, such as craniofacial bone healing. In this anatomical region, bone growth occurs primarily via intramembranous ossification which does not require intermediate cartilage formation. It has yet

to be determined whether or not the beneficial effects of Mg degradation observed in long bones will also occur in craniofacial bones. For these reasons, studies should be conducted testing Mg devices in craniofacial defect models.

In addition to fracture fixation, Mg alloys should be considered for other medical applications in which bone growth is desired. For instance, Mg devices may be used to regenerate bone after tumor resection or bone loss caused by dental disease such as periodontitis. Alternatively, Mg alloys could be used for soft tissue applications, such as stents, sutures, and staples [191-193].

Regardless of the desired clinical application, rigorous long term studies will be required to fully demonstrate the safety and efficacy of Mg devices in vivo. These studies should encompass the entire life span of the devices, from implantation through total degradation. In addition, studies involving fracture fixation or bone regeneration should be conducted over long enough time periods to observe bone remodeling following healing. Throughout these studies, device degradation should be carefully monitored, including clearance of associated gas release and corrosion products.

APPENDIX A

SUPPLEMENTAL DATA

A.1 SUPPLEMENTAL FIGURES

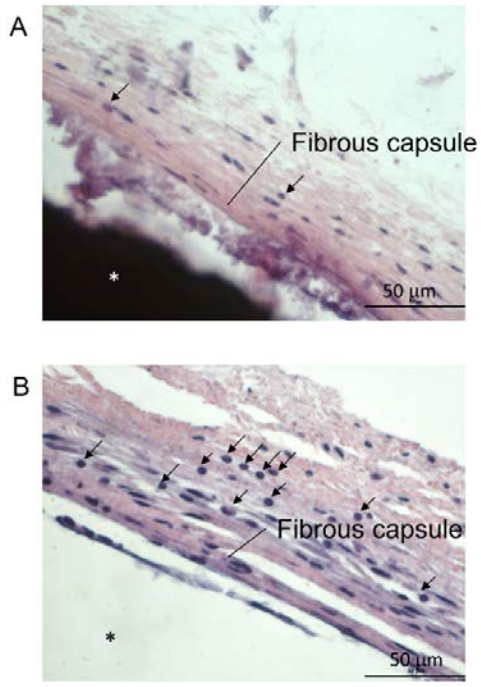

Supplemental Figure 1. H&E staining showing appropriate immune response around Mg alloys. H&E staining of tissue surrounding pure Mg (A) and AZ31(B). Mild chronic inflammation was observed around pure Mg, and mild to moderate chronic inflammation was observed around AZ31. Arrows indicate inflammatory cells. * indicates implant location. Scale bars are 50 µm.

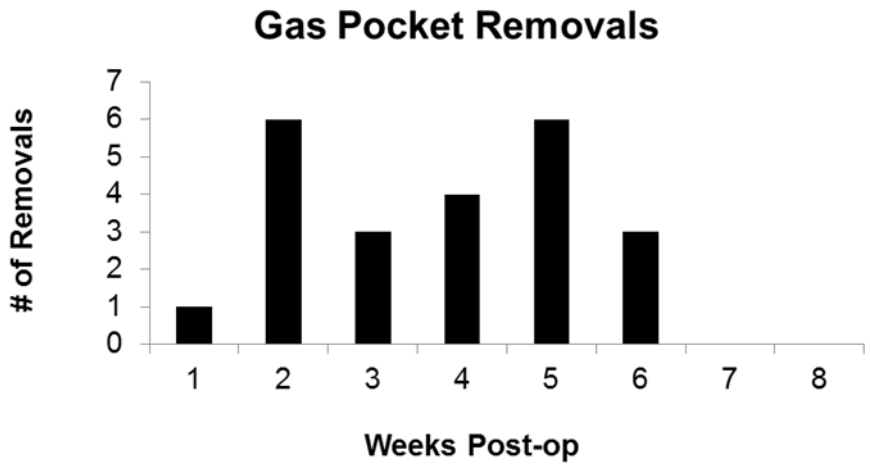

Supplemental Figure 2. Quantification of subcutaneous gas pockets.

Subcutaneous gas pockets were removed per animal care facility guidelines. Gas pockets were observed through 6 weeks post-op in 50% of all animals. Some animals required multiple removals per week, while others required no removals. No gas pockets were observed after 6 weeks.

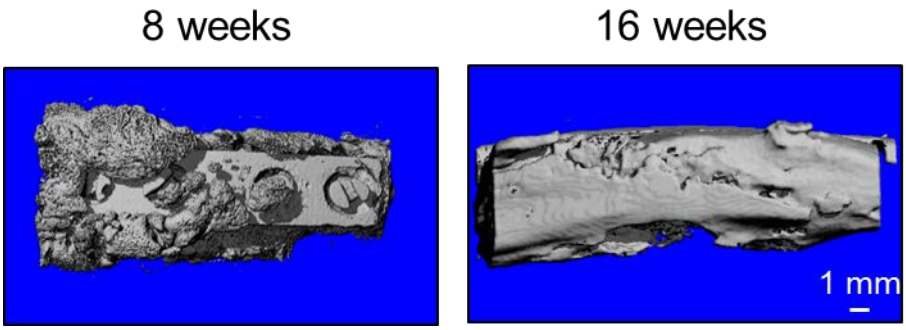

Supplemental Figure 3. MicroCT showing bone overgrowth around 99.9% Mg devices [110].

3D reconstructions show partial bone overgrowth after 8 weeks and full overgrowth by 16 weeks. In contrast to bone formed around WXQK devices, bone around 99.9% Mg devices appeared smooth and less porous.

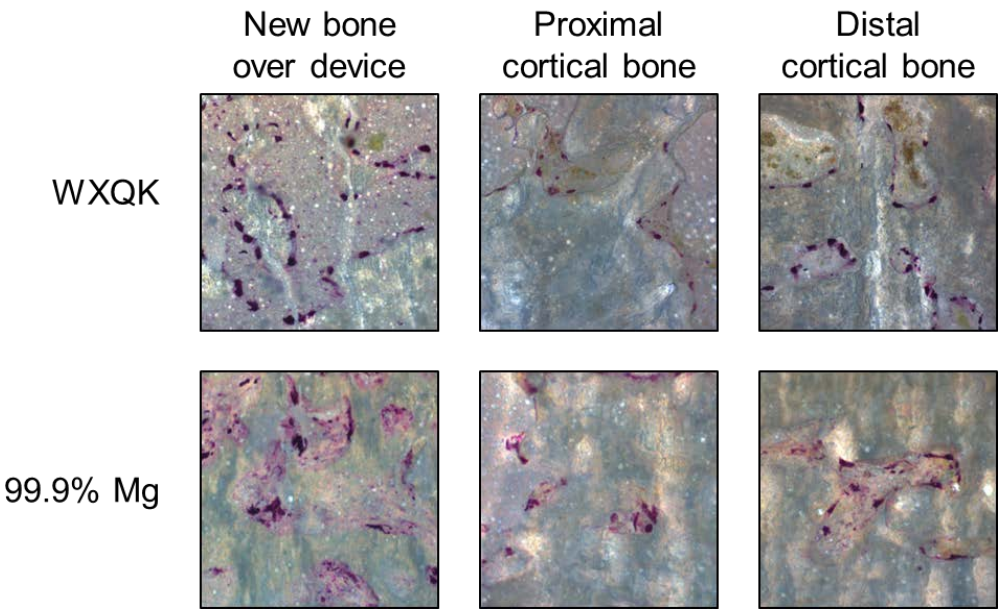

Supplemental Figure 4. TRAP staining identifying osteoclasts.

TRAP staining (red/purple) revealed osteoclasts present in all areas of remodeling bone, including newly formed bone over the devices, as well as the proximal and distal cortical bone layers at 8 weeks. TRAP staining was compared to previously studied 99.9% Mg [110], revealing similar osteoclast expression with both materials. Osteoclasts were not observed by 16 weeks post-op (not shown).

A.2 SUPPLEMENTAL TABLES

Table 4. 99.9% Mg composition including possible impurities (Goodfellow).

Mg Alloy	Primary Composition	Impurities (ppm)
99.9% Mg ("pure Mg")	99.9% Mg	Al 70, Cu 20, Fe 280, Mn 170, Ni <10, Si 50, Zn <20

BIBLIOGRAPHY

[1] Bruce Alberts AJ, Julian Lewis, Martin Raff, Keith Roberts, and Peter Walter. Molecular Biology of the Cell, 4th Edition. New York: Garland Science; 2002.

[2] Sandy C. Marks Jr. DCH. The Structure and Development of Bone. In: John P. Bilezikian LGR, Gideon A. Rodan editor. Principles of Bone Biology. San Diego: Academic Press; 1996.

[3] Yuan H, de Groot K. Calcium Phosphate Biomaterials: An Overview. In: Reis RL, Weiner S, editors. Learning from Nature How to Design New Implantable Biomaterialsis: From Biomineralization Fundamentals to Biomimetic Materials and Processing Routes: Springer Netherlands; 2005. p. 37-57.

[4] Edgar R, Domrachev M, Lash AE. Gene Expression Omnibus: NCBI gene expression and hybridization array data repository. Nucleic acids research 2002;30:207-10.

[5] Hauschka PV. Osteocalcin: the vitamin K-dependent Ca2+-binding protein of bone matrix. Haemostasis 1986;16:258-72.

[6] Imai Y, Youn M-Y, Inoue K, Takada I, Kouzmenko A, Kato S. Nuclear Receptors in Bone Physiology and Diseases2013.

[7] Young A. Janet Vaughan “The Physiology of Bone”. British Journal of Sports Medicine 1981;15:237-.

[8] Malizos KN, Papatheodorou LK. The healing potential of the periosteum: Molecular aspects. Injury 2005;36:S13-S9.

[9] Gilbert S. Osteogenesis: The Development of Bones. Developmental Biology, 6th edition. MA: Sinauer Associates; 2000.

[10] Rosset P, Deschaseaux F, Layrolle P. Cell therapy for bone repair. Orthopaedics & traumatology, surgery & research : OTSR 2014;100:S107-12.

[11] Dumont J, Cruess RL. Healing of Bone, Tendon and Ligament. Fractures 1975.

[12] Perren SM. Evolution of the internal fixation of long bone fractures. The scientific basis of biological internal fixation: choosing a new balance between stability and biology. J Bone Joint Surg Br 2002;84:1093-110.

[13] Carter DR, Beaupre GS, Giori NJ, Helms JA. Mechanobiology of skeletal regeneration. Clin Orthop Relat Res 1998:S41-55.

[14] Orthopedic Network News 2011 Trauma Update. 2011.

[15] Staiger MP, Pietak AM, Huadmai J, Dias G. Magnesium and its alloys as orthopedic biomaterials: A review. Biomaterials 2006;27:1728-34.

[16] Pietak A, Mahoney P, Dias GJ, Staiger MP. Bone-like matrix formation on magnesium and magnesium alloys. Journal of Materials Science: Materials in Medicine 2008;19:407-15.

[17] Puleo DA, Huh WW. Acute toxicity of metal ions in cultures of osteogenic cells derived from bone marrow stromal cells. J Appl Biomater 1995;6:109-16.

[18] Jacobs JJ, Gilbert JL, Urban RM. Corrosion of metal orthopaedic implants. The Journal of bone and joint surgery American volume 1998;80:268.

[19] Rokkanen PU, Böstman O, Hirvensalo E, Mäkelä EA, Partio EK, Pätiälä H, et al. Bioabsorbable fixation in orthopaedic surgery and traumatology. Biomaterials 2000;21:2607-13.

[20] Colton C, Krikler S, Schatzker J, Trafton P. AO Surgery Reference. 2007;2012.

[21] Suchenski M, McCarthy MB, Chowaniec D, Hansen D, McKinnon W, Apostolakos J, et al. Material properties and composition of soft-tissue fixation. Arthroscopy : the journal of arthroscopic & related surgery : official publication of the Arthroscopy Association of North America and the International Arthroscopy Association 2010;26:821-31.

[22] Böstman O, Hirvensalo E, Mäkinen J, Rokkanen P. Foreign-body reactions to fracture fixation implants of biodegradable synthetic polymers. J Bone Joint Surg Br 1990;72:592-6.

[23] Weiler A, Helling HJ, Kirch U, Zirbes TK, Rehm KE. Foreign-body reaction and the course of osteolysis after polyglycolide implants for fracture fixation: experimental study in sheep. J Bone joint Surg Br 1996;78:369-76.

[24] Claes LE. Mechanical characterization of biodegradable implants. Clin Mater 1992;10:41-6.

[25] Hofmann GO. Biodegradable implants in traumatology: a review on the state-of-the-art. Archives of orthopaedic and trauma surgery 1995;114:123-32.

[26] Witte F, Kaese V, Haferkamp H, Switzer E, Meyer-Lindenberg A, Wirth CJ, et al. In vivo corrosion of four magnesium alloys and the associated bone response. Biomaterials 2005;26:3557-63.

[27] Zheng YF, Gu XN, Witte F. Biodegradable metals. Materials Science and Engineering: R: Reports 2014;77:1-34.

[28] Kraus T, Fischerauer SF, Hänzi AC, Uggowitzer PJ, Löffler JF, Weinberg AM. Magnesium alloys for temporary implants in osteosynthesis: in vivo studies of their degradation and interaction with bone. Acta biomaterialia 2012;8:1230-8.

[29] Witte F, Fischer J, Nellesen J, Crostack H-A, Kaese V, Pisch A, et al. In vitro and in vivo corrosion measurements of magnesium alloys. Biomaterials 2006;27:1013-8.

[30] Witte F, Ulrich H, Palm C, Willbold E. Biodegradable magnesium scaffolds: Part II: peri-implant bone remodeling. Journal of biomedical materials research Part A 2007;81:757-65.

[31] Okuma T. Magnesium and bone strength. Nutrition (Burbank, Los Angeles County, Calif) 2001;17:679-80.

[32] Elin RJ. Assessment of magnesium status. Clinical Chemistry 1987;33:1965.

[33] Witkowski M, Hubert J, Mazur A. Methods of assessment of magnesium status in humans: a systematic review. Magnesium research : official organ of the International Society for the Development of Research on Magnesium 2011;24:163-80.

[34] DeGarmo P. Materials and Processes in Manufacturing, 5th Edition. New York: Collin Macmillan; 1979.

[35] Witte F. The history of biodegradable magnesium implants: A review. Acta Biomaterialia 2010;6:1680-92.

[36] Witte F, Feyerabend F, Maier P, Fischer J, Störmer M, Blawert C, et al. Biodegradable magnesium–hydroxyapatite metal matrix composites. Biomaterials 2007;28:2163-74.

[37] Xu L, Pan F, Yu G, Yang L, Zhang E, Yang K. In vitro and in vivo evaluation of the surface bioactivity of a calcium phosphate coated magnesium alloy. Biomaterials 2009;30:1512-23.

[38] Xu L, Yu G, Zhang E, Pan F, Yang K. In vivo corrosion behavior of Mg-Mn-Zn alloy for bone implant application. Journal of Biomedical Materials Research Part A 2007;83A:703-11.

[39] Li Z, Gu X, Lou S, Zheng Y. The development of binary Mg–Ca alloys for use as biodegradable materials within bone. Biomaterials 2008;29:1329-44.

[40] Witte F, Ulrich H, Rudert M, Willbold E. Biodegradable magnesium scaffolds: Part 1: appropriate inflammatory response. J Biomed Mater Res A 2007;81:748-56.

[41] Willbold E, Kaya AA, Kaya RA, Beckmann F, Witte F. Corrosion of magnesium alloy AZ31 screws is dependent on the implantation site. Materials Science and Engineering B 2011;176.

[42] Witte F, Hort N, Vogt C, Cohen S, Kainer KU, Willumeit R, et al. Degradable biomaterials based on magnesium corrosion. Current Opinion in Solid State and Materials Science 2008;12:63-72.

[43] Ankrum JA, Ong JF, Karp JM. Mesenchymal stem cells: immune evasive, not immune privileged. Nat Biotech 2014;32:252-60.

[44] Krebsbach PH, Kuznetsov SA, Bianco P, Robey PG. Bone marrow stromal cells: characterization and clinical application. Critical reviews in oral biology and medicine : an official publication of the American Association of Oral Biologists 1999;10:165-81.

[45] Bianco P, Robey PG. Skeletal stem cells. Development (Cambridge, England) 2015;142:1023-7.

[46] Bianco P, Riminucci M, Gronthos S, Robey PG. Bone marrow stromal stem cells: nature, biology, and potential applications. Stem cells (Dayton, Ohio) 2001;19:180-92.

[47] Grayson WL, Bunnell BA, Martin E, Frazier T, Hung BP, Gimble JM. Stromal cells and stem cells in clinical bone regeneration. Nature reviews Endocrinology 2015;11:140-50.

[48] Robey PG. Cell Sources for Bone Regeneration: The Good, the Bad, and the Ugly (But Promising). Tissue Engineering Part B, Reviews 2011;17:423-30.

[49] Chatterjea A, Meijer G, van Blitterswijk C, de Boer J. Clinical Application of Human Mesenchymal Stromal Cells for Bone Tissue Engineering. Stem Cells International 2010;2010:12.

[50] Zaky SH, Lee KW, Gao J, Jensen A, Close J, Wang Y, et al. Poly(Glycerol sebacate) elastomer: a novel material for mechanically loaded bone regeneration. Tissue engineering Part A 2014;20:45-53.

[51] Tevlin R, McArdle A, Atashroo D, Walmsley GG, Senarath-Yapa K, Zielins ER, et al. Biomaterials for craniofacial bone engineering. Journal of dental research 2014;93:1187-95.

[52] Syed-Picard FN, Larkin LM, Shaw CM, Arruda EM. Three-dimensional engineered bone from bone marrow stromal cells and their autogenous extracellular matrix. Tissue engineering Part A 2009;15:187-95.

[53] Syed-Picard FN, Ray HL, Jr., Kumta PN, Sfeir C. Scaffoldless tissue-engineered dental pulp cell constructs for endodontic therapy. Journal of dental research 2014;93:250-5.

[54] Akahane M, Nakamura A, Ohgushi H, Shigematsu H, Dohi Y, Takakura Y. Osteogenic matrix sheet-cell transplantation using osteoblastic cell sheet resulted in bone formation without scaffold at an ectopic site. Journal of tissue engineering and regenerative medicine 2008;2:196-201.

[55] Athanasiou KA, Eswaramoorthy R, Hadidi P, Hu JC. Self-organization and the self-assembling process in tissue engineering. Annual review of biomedical engineering 2013;15:115-36.

[56] Pearce AI, Richards RG, Milz S, Schneider E, Pearce SG. Animal models for implant biomaterial research in bone: a review. European cells & materials 2007;13:1-10.

[57] Yoshizawa S, Chaya A, Verdelis K, Bilodeau EA, Sfeir C. An in vivo model to assess magnesium alloys and their biological effect on human bone marrow stromal cells. Acta Biomater 2015.

[58] Bergen GS, National Center for Health Statistics (U.S.). Injury in the United States : 2007 chartbook. Hyattsville, MD: U.S. Department of Health and Human Services, Centers for Disease Control and Prevention, National Center for Health Statistics; 2008.

[59] Hanson B, van der Werken C, Stengel D. Surgeons' beliefs and perceptions about removal of orthopaedic implants. BMC musculoskeletal disorders 2008;9:73.

[60] Busam ML, Esther RJ, Obremskey WT. Hardware removal: indications and expectations. The Journal of the American Academy of Orthopaedic Surgeons 2006;14:113-20.

[61] Pietak A, Mahoney P, Dias GJ, Staiger MP. Bone-like matrix formation on magnesium and magnesium alloys. Journal of materials science Materials in medicine 2008;19:407-15.

[62] Jacobs JJ, Gilbert JL, Urban RM. Corrosion of metal orthopaedic implants. The Journal of bone and joint surgery American volume 1998;80:268-82.

[63] Mantripragada VP, Lecka-Czernik B, Ebraheim NA, Jayasuriya AC. An overview of recent advances in designing orthopedic and craniofacial implants. J Biomed Mater Res A 2013;101:3349-64.

[64] Claes L, Ignatius A. Development of new, biodegradable implants. Chirurg 2002;73:990-6.

[65] Abdullah MR, Goharian A, Abdul Kadir MR, Wahit MU. Biomechanical and bioactivity concepts of polyetheretherketone composites for use in orthopedic implants-a review. J Biomed Mater Res A 2015.

[66] Bostman O, Pihlajamaki H. Clinical biocompatibility of biodegradable orthopaedic implants for internal fixation: a review. Biomaterials 2000;21:2615-21.

[67] Bostman OM, Pihlajamaki HK. Adverse tissue reactions to bioabsorbable fixation devices. Clinical Orthopaedics and Related Research 2000:216-27.

[68] Fraser RK, Cole WG. Osteolysis after Biodegradable Pin Fixation of Fractures in Children. Journal of Bone and Joint Surgery-British Volume 1992;74:929-30.

[69] Gu XN, Zheng YF, Cheng Y, Zhong SP, Xi TF. In vitro corrosion and biocompatibility of binary magnesium alloys. Biomaterials 2009;30:484-98.

[70] Chou DT, Hong D, Saha P, Ferrero J, Lee B, Tan Z, et al. In vitro and in vivo corrosion, cytocompatibility and mechanical properties of biodegradable Mg-Y-Ca-Zr alloys as implant materials. Acta Biomater 2013;9:8518-33.

[71] Hong D, Saha P, Chou DT, Lee B, Collins BE, Tan Z, et al. In vitro degradation and cytotoxicity response of Mg-4% Zn-0.5% Zr (ZK40) alloy as a potential biodegradable material. Acta Biomater 2013;9:8534-47.

[72] Willbold E, Kalla K, Bartsch I, Bobe K, Brauneis M, Remennik S, et al. Biocompatibility of rapidly solidified magnesium alloy RS66 as a temporary biodegradable metal. Acta Biomater 2013;9:8509-17.

[73] Castellani C, Lindtner RA, Hausbrandt P, Tschegg E, Stanzl-Tschegg SE, Zanoni G, et al. Bone-implant interface strength and osseointegration: Biodegradable magnesium alloy versus standard titanium control. Acta Biomaterialia 2011;7:432-40.

[74] Witte F, Ulrich H, Palm C, Willbold E. Biodegradable magnesium scaffolds: Part II: peri-implant bone remodeling. J Biomed Mater Res A 2007;81:757-65.

[75] Janning C, Willbold E, Vogt C, Nellesen J, Meyer-Lindenberg A, Windhagen H, et al. Magnesium hydroxide temporarily enhancing osteoblast activity and decreasing the osteoclast number in peri-implant bone remodelling. Acta Biomaterialia 2010;6:1861-8.

[76] Yoshizawa S, Brown A, Barchowsky A, Sfeir C. Magnesium ion stimulation of bone marrow stromal cells enhances osteogenic activity, simulating the effect of magnesium alloy degradation. Acta Biomater 2014;10:2834-42.

[77] Habibovic P, Woodfield T, de Groot K, van Blitterswijk C. Predictive value of in vitro and in vivo assays in bone and cartilage repair - What do they really tell us about the clinical performance? Tissue Engineering 2006;585:327-60.

[78] Walker J, Shadanbaz S, Woodfield TB, Staiger MP, Dias GJ. Magnesium biomaterials for orthopedic application: a review from a biological perspective. Journal of biomedical materials research Part B, Applied biomaterials 2014;102:1316-31.

[79] Witte F, Fischer J, Nellesen J, Crostack HA, Kaese V, Pisch A, et al. In vitro and in vivo corrosion measurements of magnesium alloys. Biomaterials 2006;27:1013-8.

[80] Feyerabend F, Fischer J, Holtz J, Witte F, Willumeit R, Drucker H, et al. Evaluation of short-term effects of rare earth and other elements used in magnesium alloys on primary cells and cell lines. Acta Biomaterialia 2010;6:1834-42.

[81] Mankani MH, Kuznetsov SA, Fowler B, Kingman A, Robey PG. In vivo bone formation by human bone marrow stromal cells: Effect of carrier particle size and shape. Biotechnol Bioeng 2001;72:96-107.

[82] Meinel L, Fajardo R, Hofmann S, Langer R, Chen J, Snyder B, et al. Silk implants for the healing of critical size bone defects. Bone 2005;37:688-98.

[83] Mueller SM, Glowacki J. Age-related decline in the osteogenic potential of human bone marrow cells cultured in three-dimensional collagen sponges. J Cell Biochem 2001;82:583-90.

[84] Donnenberg AD, Gorantla VS, Schneeberger S, Moore LR, Brandacher G, Stanczak HM, et al. Clinical implementation of a procedure to prepare bone marrow cells from cadaveric vertebral bodies. Regenerative medicine 2011;6:701-6.

[85] Henderson SE, Verdelis K, Maiti S, Pal S, Chung WL, Chou DT, et al. Magnesium alloys as a biomaterial for degradable craniofacial screws. Acta Biomater 2014;10:2323-32.

[86] Chaya A, Yoshizawa S, Verdelis K, Noorani S, Costello BJ, Sfeir C. Fracture healing using degradable magnesium fixation plates and screws. Journal of oral and maxillofacial surgery : official journal of the American Association of Oral and Maxillofacial Surgeons 2015;73:295-305.

[87] Macdonald TL, Martin RB. Aluminum ion in biological systems. Trends Biochem Sci 1988;13:15-9.

[88] Willbold E, Kaya AA, Kaya RA, Beckmann F, Witte F. Corrosion of magnesium alloy AZ31 screws is dependent on the implantation site. Materials Science and Engineering B-Advanced Functional Solid-State Materials 2011;176:1835-40.

[89] Witte F, Fischer J, Nellesen J, Vogt C, Vogt J, Donath T, et al. In vivo corrosion and corrosion protection of magnesium alloy LAE442. Acta Biomaterialia 2010;6:1792-9.

[90] Walker J, Shadanbaz S, Kirkland NT, Stace E, Woodfield T, Staiger MP, et al. Magnesium alloys: Predicting in vivo corrosion with in vitro immersion testing. J Biomed Mater Res B 2012;100B:1134-41.

[91] Song GL, Atrens A. Understanding magnesium corrosion - A framework for improved alloy performance. Advanced Engineering Materials 2003;5:837-58.

[92] Choudhary L, Raman RKS. Magnesium alloys as body implants: Fracture mechanism under dynamic and static loadings in a physiological environment. Acta Biomaterialia 2012;8:916-23.

[93] Tu Q, Valverde P, Li S, Zhang J, Yang P, Chen J. Osterix overexpression in mesenchymal stem cells stimulates healing of critical-sized defects in murine calvarial bone. Tissue Eng 2007;13:2431-40.

[94] Xing J, Jin H, Hou T, Chang Z, Luo F, Wang P, et al. Establishment of a bilateral femoral large segmental bone defect mouse model potentially applicable to basic research in bone tissue engineering. J Surg Res 2014;192:454-63.

[95] Geiger M, Li RH, Friess W. Collagen sponges for bone regeneration with rhBMP-2. Advanced Drug Delivery Reviews 2003;55:1613-29.

[96] Friess W. Collagen - biomaterial for drug delivery. European Journal of Pharmaceutics and Biopharmaceutics 1998;45:113-36.

[97] Chvapil M. Collagen Sponge - Theory and Practice of Medical Applications. J Biomed Mater Res 1977;11:721-41.

[98] Bowen PK, Drelich J, Goldman J. Magnesium in the murine artery: probing the products of corrosion. Acta Biomater 2014;10:1475-83.

[99] Walker J, Shadanbaz S, Woodfield TB, Staiger MP, Dias GJ. Magnesium biomaterials for orthopedic application: A review from a biological perspective. Journal of biomedical materials research Part B, Applied biomaterials 2014.

[100] Chicatun F, Pedraza CE, Muja N, Ghezzi CE, McKee MD, Nazhat SN. Effect of chitosan incorporation and scaffold geometry on chondrocyte function in dense collagen type I hydrogels. Tissue engineering Part A 2013;19:2553-64.

[101] Yang Z, Wu Y, Li C, Zhang T, Zou Y, Hui JH, et al. Improved mesenchymal stem cells attachment and in vitro cartilage tissue formation on chitosan-modified poly(L-lactide-co-epsilon-caprolactone) scaffold. Tissue engineering Part A 2012;18:242-51.

[102] Peyton SR, Kalcioglu ZI, Cohen JC, Runkle AP, Van Vliet KJ, Lauffenburger DA, et al. Marrow-derived stem cell motility in 3D synthetic scaffold is governed by geometry along with adhesivity and stiffness. Biotechnology and bioengineering 2011;108:1181-93.

[103] Discher DE, Janmey P, Wang YL. Tissue cells feel and respond to the stiffness of their substrate. Science (New York, NY) 2005;310:1139-43.

[104] Hong MH, Kim SM, Om JY, Kwon N, Lee YK. Seeding cells on calcium phosphate scaffolds using hydrogel enhanced osteoblast proliferation and differentiation. Annals of biomedical engineering 2014;42:1424-35.

[105] Papadimitropoulos A, Riboldi SA, Tonnarelli B, Piccinini E, Woodruff MA, Hutmacher DW, et al. A collagen network phase improves cell seeding of open-pore structure scaffolds under perfusion. Journal of tissue engineering and regenerative medicine 2013;7:183-91.

[106] Haykal S, Salna M, Zhou Y, Marcus P, Fatehi M, Frost G, et al. Double-chamber rotating bioreactor for dynamic perfusion cell seeding of large-segment tracheal allografts: comparison to conventional static methods. Tissue engineering Part C, Methods 2014;20:681-92.

[107] Buizer AT, Veldhuizen AG, Bulstra SK, Kuijer R. Static versus vacuum cell seeding on high and low porosity ceramic scaffolds. Journal of biomaterials applications 2013;29:3-13.

[108] Griffon DJ, Abulencia JP, Ragetly GR, Fredericks LP, Chaieb S. A comparative study of seeding techniques and three-dimensional matrices for mesenchymal cell attachment. Journal of tissue engineering and regenerative medicine 2011;5:169-79.

[109] Henderson SE, Verdelis K, Maiti S, Pal S, Chung WL, Chou DT, et al. Magnesium alloys as a biomaterial for degradable craniofacial screws. Acta Biomater 2013.

[110] Chaya A, Yoshizawa S, Verdelis K, Myers N, Costello BJ, Chou DT, et al. In vivo study of magnesium plate and screw degradation and bone fracture healing. Acta Biomater 2015.

[111] VanDusen KW, Syverud BC, Williams ML, Lee JD, Larkin LM. Engineered skeletal muscle units for repair of volumetric muscle loss in the tibialis anterior muscle of a rat. Tissue engineering Part A 2014;20:2920-30.

[112] Narita T, Shintani Y, Ikebe C, Kaneko M, Campbell NG, Coppen SR, et al. The use of scaffold-free cell sheet technique to refine mesenchymal stromal cell-based therapy for heart failure. Molecular therapy : the journal of the American Society of Gene Therapy 2013;21:860-7.

[113] Syed-Picard FN, Jayaraman T, Lam RSK, Beniash E, Sfeir C. Osteoinductivity of calcium phosphate mediated by connexin 43. Biomaterials 2013;34:3763-74.

[114] Song G, Atrens A. Understanding Magnesium Corrosion—A Framework for Improved Alloy Performance. Advanced Engineering Materials 2003;5:837-58.

[115] Yang C, Yuan G, Zhang J, Tang Z, Zhang X, Dai K. Effects of magnesium alloys extracts on adult human bone marrow-derived stromal cell viability and osteogenic differentiation. Biomedical materials (Bristol, England) 2010;5:045005.

[116] Wu L, Luthringer BJ, Feyerabend F, Schilling AF, Willumeit R. Effects of extracellular magnesium on the differentiation and function of human osteoclasts. Acta Biomater 2014;10:2843-54.

[117] Janning C, Willbold E, Vogt C, Nellesen J, Meyer-Lindenberg A, Windhagen H, et al. Magnesium hydroxide temporarily enhancing osteoblast activity and decreasing the osteoclast number in peri-implant bone remodelling. Acta Biomater 2010;6:1861-8.

[118] Barradas AM, Yuan H, van Blitterswijk CA, Habibovic P. Osteoinductive biomaterials: current knowledge of properties, experimental models and biological mechanisms. European cells & materials 2011;21:407-29; discussion 29.

[119] Jang Y, Collins B, Sankar J, Yun Y. Effect of biologically relevant ions on the corrosion products formed on alloy AZ31B: an improved understanding of magnesium corrosion. Acta Biomater 2013;9:8761-70.

[120] Jang Y, Tan Z, Jurey C, Xu Z, Dong Z, Collins B, et al. Understanding corrosion behavior of Mg–Zn–Ca alloys from subcutaneous mouse model: Effect of Zn element concentration and plasma electrolytic oxidation. Materials Science and Engineering: C 2015;48:28-40.

[121] Fujibayashi S, Neo M, Kim HM, Kokubo T, Nakamura T. Osteoinduction of porous bioactive titanium metal. Biomaterials 2004;25:443-50.

[122] Winter GD, Simpson BJ. Heterotopic bone formed in a synthetic sponge in the skin of young pigs. Nature 1969;223:88-90.

[123] Urist MR. Bone: formation by autoinduction. Science (New York, NY) 1965;150:893-9.

[124] Barrere F, van der Valk CM, Dalmeijer RA, Meijer G, van Blitterswijk CA, de Groot K, et al. Osteogenecity of octacalcium phosphate coatings applied on porous metal implants. J Biomed Mater Res A 2003;66:779-88.

[125] Santander S, Alcaine C, Lyahyai J, Perez MA, Rodellar C, Doblare M, et al. In vitro osteoinduction of human mesenchymal stem cells in biomimetic surface modified titanium alloy implants. Dental materials journal 2014;33:305-12.

[126] Zhang Q, Leng Y, Xin R. A comparative study of electrochemical deposition and biomimetic deposition of calcium phosphate on porous titanium. Biomaterials 2005;26:2857-65.

[127] Stevens B, Yang Y, Mohandras A, Stucker B, Nguyen K. A Review of Materials, Fabrication Methods, and Strategies Used to Enhance Bone Regeneration in Engineered Bone Tissues. Journal of Biomedical Materials Research Part B: Applied Biomaterials 2008;85B:573-82.

[128] The 2004 Surgeon General's Report on Bone Health and Osteoporosis: What It Means To You. In: Services UDoHaH, editor.2004.

[129] Staiger M, Pietak A, Huadmai J, Dias G. Magnesium and its alloys as orthopedic biomaterials: A review. Biomaterials 2006:1728-34.

[130] Jacobs J, Gilbert J, Urban R. Corrosion of Metal Orthopaedic Implants. J Bone and Joint Surg 1998;80.

[131] Rokkanen PU, Bostman O, Hirvensalo E, Makela EA, Partio EK, Patiala H, et al. Bioabsorbable fixation in orthopaedic surgery and traumatology. Biomaterials 2000;21:2607-13.

[132] Hofmann G. Biodegradable implants in traumatology: a review on the state-of-the-art. Arch Orthop Trauma Surg 1992;114:123-32.

[133] Suchenski M, McCarthy M, Chowaniec D, Hansen D, McKinnon W, Apostolakos J, et al. Material Properties and Composition of Soft-Tissue Fixation. Arthroscopy 2010;26:821-31.

[134] Weiler A, Helling H, Kirch U, Zirbes T, Rehm K. Foreign-body reaction and the course of osteolysis after polyglycolide implants for fracture fixation: experimental study in sheep. J Bone joint Surg Br 1996;78:369-76.

[135] Kraus T, Fischerauer S, Hanzi A, Uggowitzer P, Loffler J. Magnesium alloys for temporary implants in osteosynthesis: In vivo studies of their degradation and interaction with bone. Acta Biomaterialia 2012;8:1230-8.

[136] Okuma T. Magnesium and bone strength. Nutrition 2001;17:679-80.

[137] Yoshizawa S, Brown A, Barchowsky A, Sfeir C. Magnesium ion stimulation of bone marrow stromal cells enhances osteogenic activity, simulating the effect of magnesium alloy degradation. Acta Biomater 2014.

[138] Gu X, Zheng Y, Cheng Y, Zhong S, Xi T. In vitro corrosion and biocompatibility of binary magnesium alloys. Biomaterials 2009;30:484-98.

[139] Luppen CA, Blake CA, Ammirati KM, Stevens ML, Seeherman HJ, Wozney JM, et al. Recombinant Human Bone Morphogenetic Protein-2 Enhances Osteotomy Healing in Glucocorticoid-Treated Rabbits. J Bone and Mineral Research 2002;17:301-10.

[140] Mills LA, Simpson AHRW. In vivo models of bone repair. J Bone and Joint Surg 2012;94-B:865-74.

[141] Schatzker J, Chapman M, Ha'Eri GB, Fornasier VL, Sumner-Smith G, Williams C. The effect of calcitonin on fracture healing. Clin Orthop Relat Res 1979:303-6.

[142] Stevens B, Yang Y, Mohandas A, Stucker B, Nguyen KT. A review of materials, fabrication methods, and strategies used to enhance bone regeneration in engineered bone tissues. Journal of Biomedical Materials Research Part B: Applied Biomaterials 2008;85B:573-82.

[143] Böstman O, Hirvensalo E, Mäkinen J, Rokkanen P. Foreign-body reactions to fracture fixation implants of biodegradable synthetic polymers. The Journal of bone and joint surgery British volume 1990;72:592.

[144] Yang JX, Cui FZ, Lee IS, Zhang Y, Yin QS, Xia H, et al. In vivo biocompatibility and degradation behavior of Mg alloy coated by calcium phosphate in a rabbit model. Journal of biomaterials applications 2012;27:153-64.

[145] Chaya A, Yoshizawa S, Verdelis K, Noorani S, Costello BJ, Sfeir C. Fracture healing using degradable magnesium fixation plates and screws. Journal of Oral and Maxillofacial Surgery.

[146] Luppen CA, Blake CA, Ammirati KM, Stevens ML, Seeherman HJ, Wozney JM, et al. Recombinant Human Bone Morphogenetic Protein-2 Enhances Osteotomy Healing in Glucocorticoid-Treated Rabbits. Journal of Bone and Mineral Research 2002;17:301-10.

[147] Mills LA, Simpson AH. In vivo models of bone repair. J Bone Joint Surg Br 2012;94:865-74.

[148] Schatzker J, Chapman M, Ha'Eri GB, Fornasier VL, Sumner-Smith G, Williams C. The effect of calcitonin on fracture healing. Clinical orthopaedics and related research 1979:303-6.

[149] Ullmann B, Reifenrath J, Seitz JM, Bormann D, Meyer-Lindenberg A. Influence of the grain size on the in vivo degradation behaviour of the magnesium alloy LAE442.

Proceedings of the Institution of Mechanical Engineers Part H, Journal of engineering in medicine 2013;227:317-26.

[150] Ralston KD, Birbilis N. Effect of Grain Size on Corrosion: A Review. Corrosion 2010;66:075005--13.

[151] Bowen PK, Drelich J, Goldman J. Magnesium in the murine artery: Probing the products of corrosion. Acta Biomaterialia 2014;10:1475-83.

[152] Erdmann N, Angrisani N, Reifenrath J, Lucas A, Thorey F, Bormann D, et al. Biomechanical testing and degradation analysis of MgCa0.8 alloy screws: A comparative in vivo study in rabbits. Acta Biomaterialia 2011;7:1421-8.

[153] Zhang S, Zhang X, Zhao C, Li J, Song Y, Xie C, et al. Research on an Mg-Zn alloy as a degradable biomaterial. Acta Biomaterialia 2010;6:626-40.

[154] Wang Q, Tan L, Xu W, Zhang B, Yang K. Dynamic behaviors of a Ca–P coated AZ31B magnesium alloy during in vitro and in vivo degradations. Materials Science and Engineering: B 2011;176:1718-26.

[155] Denkena B, Köhler J, Stieghorst J, Turger A, Seitz J, Fau DR, et al. Influence of stress on the degradation behavior of Mg LAE442 implant systems. Procedia CIRP2013. p. 189-95.

[156] Yun Y, Dong Z, Yang D, Schulz MJ, Shanov VN, Yarmolenko S, et al. Biodegradable Mg corrosion and osteoblast cell culture studies. Materials Science and Engineering: C 2009;29:1814-21.

[157] Colnot C, Zhang X, Knothe Tate ML. Current insights on the regenerative potential of the periosteum: molecular, cellular, and endogenous engineering approaches. J Orthop Res 2012;30:1869-78.

[158] Bondarenko A, Angrisani N, Meyer-Lindenberg A, Seitz JM, Waizy H, Reifenrath J. Magnesium-based bone implants: Immunohistochemical analysis of peri-implant osteogenesis by evaluation of osteopontin and osteocalcin expression. Journal of Biomedical Materials Research - Part A 2014;102:1449-57.

[159] Material ASfTa. ASTM B275-05 Standard Practice for Codification of Certain Nonferrous Metals and Alloys, Cast and Wrought. Annual book of ASTM standards. Philadelphia, PA: ASTM; 2005.

[160] Qian M, StJohn DH, Frost MT. Zirconium alloying and grain refinement of magnesium alloys. Magnesium Technology 2003 2003;2003:209-14.

[161] Chaya A, Yoshizawa S, Verdelis K, Myers N, Costello BJ, Chou DT, et al. In vivo study of magnesium plate and screw degradation and bone fracture healing. Acta Biomater 2015;18:262-9.

[162] Hall EO. The Deformation and Ageing of Mild Steel: III Discussion of Results. Proceedings of the Physical Society Section B 1951;64:747.

[163] Petch NJ. The cleavage strength of polycrystals. The Journal of the Iron and Steel Institute 1953;174.

[164] Wu A-r, Xia C-q. Study of the microstructure and mechanical properties of Mg-rare earth alloys. Materials & Design 2007;28:1963-7.

[165] Liu M, Schmutz P, Uggowitzer PJ, Song G, Atrens A. The influence of yttrium (Y) on the corrosion of Mg–Y binary alloys. Corrosion Science 2010;52:3687-701.

[166] Drynda A, Hassel T, Hoehn R, Perz A, Bach F-W, Peuster M. Development and biocompatibility of a novel corrodible fluoride-coated magnesium-calcium alloy with improved degradation kinetics and adequate mechanical properties for cardiovascular applications. Journal of Biomedical Materials Research Part A 2010;93A:763-75.

[167] Saha P, Lolies K, Viswanathan S, Gokhale A, Batson R. A Systematic Study of the Grain Refinement of Magnesium by Zirconium: Minerals, Metals and Materials Society/AIME, 420 Commonwealth Dr., P. O. Box 430 Warrendale PA 15086 USA; 2010.

[168] Witte F, Hort N, Vogt C, Cohen S, Kainer KU, Willumeit R, et al. Degradable biomaterials based on magnesium corrosion. Current Opinion in Solid State & Materials Science 2008;12:63-72.

[169] Song G, StJohn D. The effect of zirconium grain refinement on the corrosion behaviour of magnesium-rare earth alloy MEZ. Journal of Light Metals 2002;2:1-16.

[170] Tie D, Feyerabend F, Muller WD, Schade R, Liefeith K, Kainer KU, et al. Antibacterial biodegradable Mg-Ag alloys. Eur Cell Mater 2013;25:284-98; discussion 98.

[171] Hänzi AC, Gunde P, Schinhammer M, Uggowitzer PJ. On the biodegradation performance of an Mg–Y–RE alloy with various surface conditions in simulated body fluid. Acta Biomaterialia 2009;5:162-71.

[172] Carter DR, Shimaoka EE, Harris WH, Gates EI, Caler WE, McCarthy JC. Changes in long-bone structural properties during the first 8 weeks of plate implantation. J Orthop Res 1984;2:80-9.

[173] Uhthoff HK, Foux A, Yeadon A, McAuley J, Black RC. Two processes of bone remodeling in plated intact femora: an experimental study in dogs. J Orthop Res 1993;11:78-91.

[174] Marks Jr SC, Odgren PR. Chapter 1 - Structure and Development of the Skeleton. In: Rodan JPBGRA, editor. Principles of Bone Biology (Second Edition). San Diego: Academic Press; 2002. p. 3-15.

[175] Cullinane DM, Einhorn TA. Chapter 2 - Biomechanics of Bone. In: Rodan JPBGRA, editor. Principles of Bone Biology (Second Edition). San Diego: Academic Press; 2002. p. 17-32.

[176] Rha EY, Paik H, Byeon JH. Bioabsorbable Plates and Screws Fixation in Mandible Fractures: Clinical Retrospective Research During a 10-Year Period. Annals of plastic surgery 2014.

[177] Singh G, Mohammad S, Chak RK, Lepcha N, Singh N, Malkunje LR. Bio-resorbable plates as effective implant in paediatric mandibular fracture. Journal of maxillofacial and oral surgery 2012;11:400-6.

[178] Perrone GS, Leisk GG, Lo TJ, Moreau JE, Haas DS, Papenburg BJ, et al. The use of silk-based devices for fracture fixation. Nature communications 2014;5:3385.

[179] Belluci MM, Schoenmaker T, Rossa-Junior C, Orrico SR, de Vries TJ, Everts V. Magnesium deficiency results in an increased formation of osteoclasts. The Journal of nutritional biochemistry 2013;24:1488-98.

[180] Kuhlmann J, Bartsch I, Willbold E, Schuchardt S, Holz O, Hort N, et al. Fast escape of hydrogen from gas cavities around corroding magnesium implants. Acta Biomater 2013;9:8714-21.

[181] Hanzi AC, Gerber I, Schinhammer M, Loffler JF, Uggowitzer PJ. On the in vitro and in vivo degradation performance and biological response of new biodegradable Mg-Y-Zn alloys. Acta Biomater 2010;6:1824-33.

[182] Razavi M, Fathi M, Savabi O, Vashaee D, Tayebi L. In vivo assessments of bioabsorbable AZ91 magnesium implants coated with nanostructured fluoridated hydroxyapatite by MAO/EPD technique for biomedical applications. Materials Science and Engineering: C 2015;48:21-7.

[183] Castiglioni S, Cazzaniga A, Albisetti W, Maier JA. Magnesium and osteoporosis: current state of knowledge and future research directions. Nutrients 2013;5:3022-33.

[184] Leidi M, Dellera F, Mariotti M, Maier JA. High magnesium inhibits human osteoblast differentiation in vitro. Magnesium research : official organ of the International Society for the Development of Research on Magnesium 2011;24:1-6.

[185] Kramer SJ, Spadaro JA, Webster DA. Antibacterial and osteoinductive properties of demineralized bone matrix treated with silver. Clinical orthopaedics and related research 1981:154-62.

[186] Albers C, Hofstetter W, Siebenrock K, Landmann R, Klenke F. CYTOTOXIC EFFECTS OF IONIC SILVER AND SILVER NANO-PARTICLES ON OSTEOBLASTS AND OSTEOCLASTS IN VITRO. Journal of Bone & Joint Surgery, British Volume 2012;94-B:163.

[187] Zhang J, Liu C, Li Y, Sun J, Wang P, Di K, et al. Effect of yttrium ion on the proliferation, differentiation and mineralization function of primary mouse osteoblasts in vitro. Journal of Rare Earths 2010;28:466-70.

[188] Waizy H, Diekmann J, Weizbauer A, Reifenrath J, Bartsch I, Neubert V, et al. In vivo study of a biodegradable orthopedic screw (MgYREZr-alloy) in a rabbit model for up to 12 months. Journal of biomaterials applications 2014;28:667-75.

[189] Castellani C, Lindtner RA, Hausbrandt P, Tschegg E, Stanzl-Tschegg SE, Zanoni G, et al. Bone-implant interface strength and osseointegration: Biodegradable magnesium alloy versus standard titanium control. Acta biomaterialia 2011;7:432-40.

[190] Windhagen H, Radtke K, Weizbauer A, Diekmann J, Noll Y, Kreimeyer U, et al. Biodegradable magnesium-based screw clinically equivalent to titanium screw in hallux valgus surgery: short term results of the first prospective, randomized, controlled clinical pilot study. Biomedical engineering online 2013;12:62.

[191] Seitz JM, Durisin M, Goldman J, Drelich JW. Recent Advances in Biodegradable Metals for Medical Sutures: A Critical Review. Advanced healthcare materials 2015;4:1915-36.

[192] Lafont A, Yang Y. Magnesium stent scaffolds: DREAMS become reality. Lancet (London, England) 2015.

[193] Wu T, Chen X, Fan D, Pang X. Development and application of metal materials in terms of vascular stents. Bio-medical materials and engineering 2015;25:435-41.